Title: A single-cell atlas of ABCA7 loss-of-function reveals lipid disruptions, mitochondrial dysfunction and DNA damage in neurons

Authors: Djuna von Maydell[1,2,†], Shannon Wright[1,2,†], Julia Maeve Bonner[1,2,†], Ping-Chieh Pao[1,2], Gloria Suella Menchaca[1,2], Gwyneth Welch[1,2], Carles A. Boix[3,4], Hansruedi Mathys[1,2,‡], Guillaume Leclerc[3], Noelle Leary[1,2], George Samaan[1,2], Manolis Kellis[3,4], Li-Huei Tsai[1,2,*]

Affiliations:

[1]Picower Institute for Learning and Memory, Massachusetts Institute of Technology; Cambridge, MA 02139, USA.

[2]Department of Brain and Cognitive Sciences, Massachusetts Institute of Technology; Cambridge, MA 02139, USA.

[3]MIT Computer Science and Artificial Intelligence Laboratory; Cambridge, MA 02139, USA.

[4]Broad Institute of MIT and Harvard; Cambridge, MA 02139, USA.

†These authors contributed equally to this work.

‡Present address: Department of Neurobiology, University of Pittsburgh; Pittsburgh, PA 15261

*Corresponding author. Email: lhtsai@mit.edu

Abstract: ABCA7 loss-of-function (LoF) variants dramatically increase the risk of Alzheimer's disease (AD), yet the pathogenic mechanisms and the cell types affected by this loss remain largely unknown. Here, we performed single-nuclear RNA sequencing of 36 human *post-mortem* samples from the prefrontal cortex (PFC) of ABCA7 LoF carriers and matched control individuals. ABCA7 LoF variants were associated with perturbed gene clusters in all major cell types. Excitatory neurons, which expressed the highest levels of ABCA7, showed profound perturbations in gene clusters related to lipid metabolism, mitochondrial function, DNA damage, and NF-kB signaling. Given the known role of ABCA7 as a lipid transporter, we reasoned that ABCA7 LoF may mediate neuronal dysfunction by altering the lipidome, and evaluated lipid changes by untargeted mass-spectrometry. Indeed, ABCA7 LoF in *post-mortem* human PFC and iPSC-derived neurons showed widespread changes to the lipidome, including increased triacylglycerides and altered abundance of multiple phospholipid species. Consistent with these observations, assays on *post-mortem* human PFC and iPSC-derived ABCA7 LoF neurons (iNs) showed increased levels of mitochondrial dysfunction, DNA damage, and NF-kB activation, suggesting that ABCA7 LoF is a causal mediator of these disruptions in neurons. This study provides a detailed atlas of ABCA7 LoF in the human brain and suggests that lipid dysregulation in neurons may be an underlying insult by which ABCA7 LoF increases AD risk.

One-Sentence Summary: ABCA7 loss-of-function, associated with increased risk for Alzheimer's, causes mitochondrial dysfunction, DNA damage, and lipid disruptions in neurons.

Introduction

Late-onset Alzheimer's Disease (LOAD), or sporadic AD (sAD), affects individuals over the age of 65 and accounts for more than 95% of all AD cases (*1*) yet the etiology of sAD remains largely unknown. Large scale genomics studies have identified genetic variants that correlate with increased risk for sAD and poor cognitive aging (*2–8*). ATP-binding cassette transporter A7 (ABCA7) was recently added to the growing list of AD risk genes (*8–13*). ABCA7 expression correlates with onset of AD neuropathology, with low expression associated with younger age of onset (*13*). While a number of rare loss of function (LoF) mutations in ABCA7 are among the strongest genetic risk variants for AD, several common single nucleotide polymorphisms (SNPs) in ABCA7 have been associated with moderate effects on AD risk (*8–11*, *14*), suggesting that ABCA7 dysfunction may play a role in a significant proportion of AD cases.

ABCA7 is a member of the A subfamily of ABC transmembrane proteins (*15*) with high sequence homology to ABCA1, the primary lipid transporter responsible for cholesterol homeostasis and high-density lipoprotein genesis in the brain. ABCA7 effluxes both cholesterol and phospholipids to APOA-I and APOE in *in vitro* studies (*16*, *17*) and is a critical regulator of lipid metabolism and immune cell functions (*18*, *19*). However, the extent of the role of ABCA7 in AD pathogenesis and the effect of ABCA7 dysfunction in different brain cell types remains unclear.

Single-nuclear RNA sequencing (snRNA-seq) permits the interrogation of cell-type specific changes and intrapopulation heterogeneity that cannot be observed with bulk RNA sequencing (*20–22*). Here, we harness the power of snRNA-seq to better understand how ABCA7 LoF variants in AD patients impact biological functions across brain cell types. We observed dysfunction across all major brain cell types, with largely distinct processes altered in each cell type. In *post-mortem* tissue analysis, excitatory neurons were particularly disrupted by ABCA7 LoF, showing perturbed gene clusters associated with lipid biosynthesis, mitochondrial dysfunction, and DNA damage. Using isogenic iPSC-derived neurons with ABCA7 knockout (KO) mutations, we show significant increases in triglyceride levels and altered phospholipid species in ABCA7 KO iPSC-derived neurons and similar patterns in bulk patient tissue from *post-mortem* brain. Furthermore, we confirmed the direct relationship between ABCA7 dysfunction and mitochondrial defects, DNA damage, and NF-kB inflammatory signaling. Together, these data provide an atlas for ABCA7 dysfunction across brain cell types, and suggest that ABCA7 loss-of-function induced lipid dysregulation may substantially impact excitatory neuronal health.

Results

Selecting ABCA7 LoF variant carriers

To investigate the cell-type-specific impact of ABCA7 in the human brain, we selected a cohort of 36 subjects from the Religious Order Study (ROS) or the Rush Memory and Aging Project (MAP) (collectively known as ROSMAP), with and without ABCA7 LoF variants (**Fig. 1A**). ABCA7 LoF variant carriers were identified by searching whole genome sequences of >1000 ROSMAP subjects for rare damaging variants in ABCA7. We identified 12 heterozygous carriers of ABCA7 LoF variants, including splice region variants (c.4416+2T>G and c.5570+5G>C), frameshift variants (p.Leu1403fs and p.Glu709fs), and nonsense 'stop gained' variants (p.Trp1245* and p.Trp1085*) (**Fig. 1A,B; Table S1**). Most of these variants have previously been associated with increased AD risk in genetic association tables (**Table S1**) (*9*, *12*). We verified ABCA7 genotypes in a subset of ABCA7 LoF carriers and controls in the cohort by

Sanger sequencing (**Fig. S1A**) and verified that all single-cell libraries matched their whole genome sequencing counterparts to ensure all samples were appropriately assigned to their respective genotypes (**Fig. S2**). Finally, we verified that none of the ABCA7 LoF individuals carried damaging variants in other AD risk genes, whose LoF has previously been associated with increased AD risk (including *TREM2, SORL1, ATP8B4, ABCA1,* and *ADAM10*) (**Data S1**) (*12*).

Each of the variants included in our ABCA7 LoF cohort (**Table S1**) is presumed to cause haploinsufficiency due to nonsense mediated decay (NMD) of transcripts containing premature termination codons. To validate this assumption, we turned to proteomic data from the *post-mortem* PFC, which are available for a subset of ROSMAP subjects (**Table S2**). We observed a significant (p=0.018) decrease in ABCA7 protein levels in the PFC in subjects carrying ABCA7 LoF variants compared to control subjects (N = 180 Con, 5 ABCA7 LoF, including one carrier of c.2126_2132delAGCAGGG, one carrier of c.3255G>A, and three carriers of c.5570+5G>C) (**Fig. S1B-D**), while there was no evidence for a difference in NeuN protein expression levels (*RBFOX3*, p=0.73, **Fig. S1E,F**), as a proxy for neuronal loss. This trend remained when considering only a subset of the samples overlapping with our single cell cohort (N = 6 Con, 4 ABCA7 LoF, p=0.17) (**Fig. S1G,H**) and when accounting for NeuN protein levels (**Fig. S1I**).

We matched the ABCA7 LoF cohort to control samples (N=24) that did not carry any damaging ABCA7 variants or damaging variants in the aforementioned AD risk genes (**Data S1**) and matched the distributions of potential confounding variables, including AD pathology, age at death, *post-mortem* intervals, sex, APOE genotype, and cognition (**Figure S1J-R; Data S2; Supplementary Text**). We also attempted to match for these variables as closely as possible across snRNA-seq batches (**Fig. S3A-I**).

Single-nucleus transcriptomic atlas of cortical tissue from ABCA7 LoF variant-carriers

For each individual, we obtained fresh frozen tissue from the BA10 region of the prefrontal cortex (PFC). We performed snRNA-seq using 10x Genomics Chromium platform, resulting in a total of 150,456 cells (102,710 cells after multiple rounds of quality control) (**Fig. 1C**). We performed initial quality control based on predefined cutoffs, followed by dimensionality reduction, batch correct, and multiple rounds of clustering to identify low quality cells (**see Methods**). We observed a uniform distribution of batch-of-origin and subject-of-origin after batch correction using the Harmony algorithm (*23*) (**Fig. S3J-L**) and as a result cell type composition by batch was similar (**Fig. S3M)**. Using graph-based clustering to identify transcriptionally-distinct groups of cells (**Fig. S4A**), we then annotated clusters by enrichment with major cell type markers (**Fig. S4B,C; Table S2; see Methods**). Annotated cell types were well-represented across individuals (**Fig. S4D)** and annotations were supported by curated marker genes (**Fig. S4E; Table S2**). We identified a heterogeneous populations of inhibitory neurons (In, *SYT1 & GAD1+*), excitatory neurons (Ex, *SYT1 & NRGN+*), astrocytes (Ast, *AQP4+*), microglia (Mic, *CSF1R+*), oligodendrocytes (Oli, *MBP & PLP1+),* and oligodendrocyte precursor cells (OPCs, *VCAN+*) (**Fig. 1C, Fig. S4,F**). Given that the putative vascular cell cluster was small and did not meet quality control (qc) cutoffs, we did not consider these cells for downstream analysis (**see Methods**).

After qc, individual-level gene expression profiles correlated well within cell types (mean correlation *circa* 0.95) (**Fig. S4G,H**). The most frequently represented cell type was excitatory

neurons (median N = 928) and oligodendrocytes (median N = 620), followed by inhibitory neurons (median N = 365), and lower numbers of OPCs, astrocytes, and microglia (N<200, **Fig. S4,J**). We found that post-qc cell type proportions were well represented across individuals (**Fig. S4,I**). For downstream analyses, we focused only on major cell types that were well-represented in this dataset, including excitatory and inhibitory neurons, astrocytes, microglia, oligodendrocytes, and OPCs.

ABCA7 LoF perturbs gene clusters and biological processes across all major cell types

To investigate cell type-specific transcriptional effects associated with ABCA7 LoF variants, we first computed differentially expressed genes (DEGs) between control and LoF individuals for each cell type, while controlling for known and unknown covariates in the model and considering only genes with a detection rate >10% (**see Methods**). We captured a total of 356 differentially expressed genes (p-value<5e-3), including 111 and 63 DEGs in excitatory and inhibitory neurons, respectively, and 15, 47, 25, and 95 DEGs in astrocytes, microglia, oligodendrocytes, and OPCs, respectively (**Data S3**). Differential gene expression scores correlated well when comparing DEGs computed on the full dataset *versus* DEGs computed on a subsets of samples (i.e. excluding APOE4 carriers and all samples from batch #2) (**Fig. S5A-F**), suggesting that there was no major confounding by batch and APOE genotype.

To globally explore gene changes across all major cell types, we first filtered genes based on perturbation by ABCA7 LoF (evidence; p<0.05, linear model, total N genes passing this cutoff = 2,389) in at least one cell type (Ex, In, Ast, Mic, Oli, or OPC). We computed a per cell type perturbation score (*S=sign(log(FC))*-log10(p-value)*), quantifying the direction and significance of the ABCA7 LoF-associated change for each gene, placing each gene into a six-dimensional (Ex, In, Ast, Mic, Oli, OPC) "perturbation space" (**Fig. 1D; see Methods**). We projected genes from this higher dimensional space into two dimensions using the nonlinear uniform manifold approximation and projection (UMAP) algorithm(*24*) for ease of visualization. This lower dimensional visual representation captured the transcriptional landscape of ABCA7 LoF gene changes across all major cell types, indicating that the majority of gene changes were cell-type-specific (i.e. up and down-regulated genes occupied distinct areas on the map for different cell types) (**Fig. S6A** and **Fig. S6B**, respectively). However, excitatory and inhibitory cells seemed to share a number of gene perturbations, while the ABCA7 LoF response by glial cells was much more distinct (**Fig. S6A-B)**.

When highlighting the top perturbed genes by cell type (ranked by $|S|$), we observed a number of DEGs that were up-regulated in ABCA7 LoF neurons compared to control that were related to DNA damage and repair (*RECQL, FANCC*), inflammatory processes (*LRBA, IGSF11*), and lipid and carbon metabolism (*PTDSS1, MTHFS*) (**Fig. 1E**). We also observed a group of up- and down-regulated genes related to chromatin maintenance and cell cycle (*HMGN5*, *MEIKIN, HELB, CEP83, TIPIN*) in neurons. Excitatory neurons showed decreased expression of genes involved in excitatory synaptic signaling (*GRM2, UNC13B*), as well as regulators of apoptosis (*CASP9, MXD1*) (**Fig. 1E**). When performing the same visualization on glial cell types, we observed decreased expression of multiple heat shock proteins and increased expression of the immune gene *CLEC7A* in microglia. Finally, we observed altered expression of a number of vesicular and ion transporter genes, such as *SLC35E4* in oligodendrocytes, *KCNK1* in OPCs, and *COPB1* in astrocytes (**Fig. 1E**).

To quantitatively summarize the ABCA7 LoF-associated transcriptional landscape across all major cell types, we next assigned genes to clusters based on their projections in 2D space (gaussian mixture model; **Fig. 1D; see Methods**). We identified 15 gene clusters, representing groups of genes that share ABCA7 LoF-associated perturbation patterns to varying degrees across the different cell types (**Fig. 1F; Figure S6C**). To interpret these gene clusters based on the biological processes they represent, we quantified to what extent each cluster was enriched for specific biological pathways (Gene Ontology Biological Process database; **see Methods; Data S4**). Enriched (hypergeometric enrichment, $p<0.01$) biological themes spanned mitochondrial processes, DNA damage and cell stress, inflammation, and metabolic and synaptic changes (**Fig. 1G**).

When testing to what extent each cell type was enriched for a given gene cluster (FDR-adjusted p-value<0.01 & |score|>0.25; permutation test; **see Methods**), we first noted several cell stress and inflammatory clusters, including a heat shock response cluster 4 (*e.g. HSP90AA1, HSPA5, ITPR1*), which was most significantly down-regulated in microglia, followed by neurons and OPCs (**Fig. 1H; Fig. S6C)**. We also observed up-regulation of inflammatory clusters in microglia and astrocytes, including clusters 5 (*e.g. HIF1A, PICALM, NFKBIA*) and 10 (*e.g. TIAL1, ATF7, DNAJA3, NFKB1*), respectively (**Fig. 1H; Fig. S6C)**. We also noted several cell motility and vesicular-associated clusters perturbed in OPCs, including up-regulation of cluster 1, which was characterized by endocytic and lysosomal degradation genes (*e.g. EEA1, PPT1, LRP12*), and cluster 0, which was down-regulated in OPCs and enriched for pathways related to cilium assembly (e.g. *CEP162, DISC1*), cytoskeleton, and cell motility (**Fig. 1H; Fig. S6C; Data S4)**.

Clusters 6 and 14, which similarly to cluster 0 were characterized by cilium, cell adhesion, and synaptic genes (*e.g. SYT11, SHANK3, IFT56*, *GABRA3, NLGN1*), showed evidence for down-regulation in excitatory and inhibitory neurons (**Fig. 1H; Fig. S6C)**. In addition, both excitatory and inhibitory neurons up-regulated the DNA repair-associated gene cluster 9 (*e.g. NUP205, POLD3, VCP*). Finally, we noted two clusters that were specifically perturbed in excitatory neurons, including cluster 8, which was characterized by a number of mitochondrial complex genes (*e.g. COX7A2*), antioxidant response (*PARK7*), and was up-regulated specifically in excitatory neurons and cluster 2, which included lipid synthesis and transport genes (*e.g. LDLR, APOL2, NR1H3, ACLY, FITM2*), and was down-regulated specifically in excitatory neurons (**Fig. 1H; Fig. S6C; Data S4)**.

ABCA7 is expressed most highly in excitatory neurons

Our snRNA-seq data suggests that neurons, particularly excitatory neurons, expressed the highest levels of ABCA7, compared to other major cell types in the brain (**Fig. 2A**). While ABCA7 transcripts were detected (count>0) in *circa* 30% of excitatory neurons and *circa* 15% of inhibitory neurons, the detection rate was considerably lower (<10%) for microglia and astrocytes and barely detectable (<5%) for oligodendrocytes and OPCs (**Fig. 2B**). We validated this expression pattern in an independent publicly available dataset from (*25*) (**Table S2**), where six human *post-mortem* temporal cortex samples were FAC-sorted into NeuN- (glial) and NeuN+ (neuronal) cell populations, followed by bulk RNA sequencing. Again, we observed significantly higher *ABCA7* levels in the neuronal population *versus* the glial cell population ($p=0.021$, paired T-test; **Fig. S7A**), which matched the snRNA-seq data ($p<2.2e-16$, paired T-test; **Fig. S7B**). We also tested several control genes, whose expression patterns in glial *versus* neuronal cells are

well established, including *ABCA1*, *APOE*, and *NEUROD1*, all of which showed expected expression patterns and matched those in the snRNA-seq data (**Fig. S7C-H**).

Major ABCA7 LoF perturbations in excitatory neurons by graph partitioning

The aforementioned data showing increased ABCA7 expression in excitatory neurons and multiple transcriptional perturbations in ABCA7 LoF suggested that excitatory neurons may be particularly vulnerable to ABCA7 LoF. Therefore, we focused our next analysis specifically on excitatory neurons.

As an alternative approach to the unsupervised clustering of gene perturbation scores described above, we next used prior knowledge of biological pathway structure to perform an in-depth characterization of perturbed biological processes in ABCA7 LoF excitatory neurons. To this end, we first estimated statistical overrepresentation of biological gene sets among up and down-regulated genes using gene set enrichment analysis (GSEA; **see Methods**). For this analysis, we focused on a smaller set of pathways (N=472) from the WikiPathways database to reduce the total number of possible false positives. We observed a total of 34 pathways with evidence for perturbation at $p<0.05$ in excitatory neurons (**Data S3**). Excitatory neurons showed evidence for up-regulation of pathways related to electron transport, cell cycle, proteasome and down-regulation of pathways related to neuronal signaling and lipid metabolism (**Fig. 2C; Data S3**).

However, many biological pathway databases carry redundant gene information, inflating the perceived biological effect and complicating downstream interpretations(*26*, *27*). To gain a better understanding of the main biological themes represented among the 268 genes ("leading edge genes"; the core genes driving the enrichment signal (*28*)) for the 34 pathways with evidence for perturbation (GSEA; $p<0.05$) specifically in excitatory neurons, we assigned the set of leading edge genes (*LE*) to non-redundant gene clusters (**Fig. 2D**). To this end, we applied the Kernighan-Lin (KL) algorithm (*29*) to the bipartite gene-pathway graph derived by drawing edges between all elements of *LE* and their associated pathways as annotated in the WikiPathways database (**Fig. 2D; see Methods**). This resulted in non-overlapping gene clusters of approximately equal size.

By applying the KL heuristic, we were able to group *LE* into a small number of gene clusters (**Data S7**) that reflected a limited number of biological processes; we identified eight gene-pathway clusters in excitatory neurons showing various degrees of evidence for perturbation in ABCA7 LoF (**Fig. 2E-G**). The majority of gene clusters (6/8) showed a tendency towards up-regulation in ABCA7 LoF. These included multiple clusters related to DNA damage and cell cycle (clusters 1, 3, and 5), two clusters (4 and 6) related to inflammatory signaling, including genes such as *IKBKB*, *PIK3CD*, *TOLLIP*, *C2*, and *CLU*, and carbon metabolism (*SUCLA2, ADSS*), and a mitochondrial function cluster (cluster 7) (**Fig. 2F,G**). The clusters which tended towards down-regulation included cluster 0, a cluster characterized by a number of synaptic and cytoskeletal genes, including several GABA receptors, and cluster 2, which was characterized by multiple transcriptional regulators of lipid and energy homeostasis (*e.g. SREBP, PPARD)* (**Fig. 2F,G; Data S7**).

ABCA7 LoF perturbs lipid homeostasis in neurons

The aforementioned analysis suggested that pathways with evidence for perturbation in excitatory neurons with ABCA7 LoF could be grouped into a number of major themes; three of which stood out to us in particular (**Fig. 2G**): (1) lipid perturbations, (2) mitochondrial function, (3) DNA damage and inflammation. Given that ABCA7 has previously been identified as a lipid transporter, with a specific preference for phospholipids (*30*, *31*), we wondered whether impaired lipid homeostasis could lie upstream of mitochondrial dysfunction, oxidative stress, and DNA damage in neurons.

Therefore, we further interrogated lipid phenotypes in ABCA7 LoF excitatory neurons. KL cluster 2 (**Fig 3A**) was characterized by a number of lipid-related pathways, including "adipogenesis", "SREBP signaling" (**Fig. 3B**) and known master-regulators of lipid-biosynthesis, such as *NR1H3, RARA,* and *PPARD* (**Fig. 3C**)**.** The majority of genes in the cluster were down-regulated in ABCA7 LoF (**Fig. 2F**), suggesting that decreased lipid biosynthesis is a feature of ABCA7 LoF excitatory neurons and that ABCA7 LoF may cause lipid disruptions in neurons.

To evaluate whether ABCA7 LoF neurons indeed show evidence for lipid dysfunction and to test whether the relationship between ABCA7 LoF and lipid disruptions is causal, we used CRISPR-Cas9 genome editing to engineer an induced pluripotent stem cell (iPSC) lines with a ABCA7 knockout mutation from an isogenic parental line, lacking ABCA7 LoF variants. Specifically, our "ABCA7KO#1" line was generated by a single base pair insertion in ABCA7 exon 3, resulting in a premature termination codon early in the *ABCA7* gene (**Fig. 3D; Fig. S8A**). We derived the line into neurons through lentiviral delivery of a doxycycline-inducible NGN2 expression cassette as previously described (*32*), maintained for 4 weeks (until D28) (**Fig. 3E**), and harvested for untargeted LC-MS lipidomics on ABCA7 KO#1 neurons compared to isogenic control neurons (**Data S8**).

We performed bulk lipidomics on two independent differentiation batches (N=3 KO#1 and N=3 WT for each batch). Individual samples across batches correlated well and clustered by ABCA7 genotype (**Fig. S9A**). When computing differentially perturbed lipid species between control and ABCA7 KO samples independently for each batch (see **Methods**), we saw good consistency (pcc=0.69) between batches (**Fig. S9B**) and decided to pool samples from each batch for further analysis to increase power and reduce noise.

Overall, these data revealed that the lipidomes of ABCA7 KO neurons differed substantially from their WT counterparts; Lipidomes clustered by genotype (**Fig. S9A**) and were linearly separable from their control counterparts when projected onto the first two principal components, jointly explaining 95% of the variance in the data (**Fig. 3F**). In total, we observed evidence for perturbation of 66 lipid species out of 410 species detected in total in ABCA7 KO vs WT cells (unpaired, two-sided T-test; $p<5e-3$), including 33 neutral lipid species, 27 phospholipid, and 6 sphingolipid species (**Fig. 3G; Data S8**). These data suggest that ABCA7 LoF may substantially impact the lipidome in neurons.

ABCA7 LoF leads to the accumulation of TAGs and disruption of phospholipids

Given that the most frequently perturbed lipid species in ABCA7 KO neurons were neutral lipids (**Fig. 3G**), we evaluated the subclass composition of these species. Of the neutral lipids, we found that the entirety of up-regulated neutral lipids were triglycerides (TAGs) (N=31; 56% of all detected TAG species) (**Data S8; Fig. 3G-I**). The down-regulated neutral lipids included two monoglycerides (MGs) (**Fig. 3G,H**). Together, these data suggest accumulation of neutral lipids in the form of TAGs.

The next most frequently perturbed lipid class were phospholipids (PLs) (**Fig. 3G,H**), including 18 up-regulated species and 9 down-regulated species in ABCA7 KO ($p<5e-3$), making up *circa* 10% of all detected PL species (**Data S8**). The PL changes were comprised primarily of phosphatidylcholine species (PC), of which 13 showed evidence for up-regulation and 8 showed evidence for down-regulation (**Fig. 3G,H,J**). Other PL-related changes included a small number of changes to cardiolipins (CL, MGCL), phosphatidylserine (PS) and phosphatidylglycerol (PG) (**Fig. 3H**). We also noted some evidence for a few sphingolipid (ceramide) changes (**Fig. 3H**). However, neutral lipid and phospholipid changes were both the most frequent (**Fig. 3H**), consistent, and robust in terms of effect sizes (**Fig. S9C**).

To ask whether ABCA7 LoF-associated lipid changes were also evident in the *post-mortem* human brain, we performed unbiased mass spectrometry-based lipidomics on a subset of the *post-mortem* human brain with and without LoF variants (N=8 for each group) used in transcriptomic analysis (**Data S9**). Given that PCs and TAGs were the most prominently perturbed species in ABCA7 LoF neurons, we visualized the distribution of these species in our human *post-mortem* samples (**Fig. 3K,L**). We found similar patterns of TAG and PC fold changes in *post-mortem* human brain, with a number of TAG species trending towards up-regulation in ABCA7 LoF (**Fig. 3K**) and a number of phosphatidylcholine species with some evidence of perturbation in *post-mortem* brain ($p<0.1$; **Fig. 3L**). When considering the full complement of lipid species, we also observed some evidence of change to a number of other phospholipid species, including cardiolipins (**Data S9**).

To further evaluate lipid-related changes in excitatory ABCA7 LoF neurons, we turned back to the single-cell data to perform a targeted analysis of lipid-associated gene changes (**see Methods; Table S2**). We found evidence ($p<0.025$) for a number of pathway changes that aligned with the lipidomic data observations, including increased expression of genes related to lipid storage and transport (e.g. *SCP, OSBPL8*) (**Fig. 3M**). Pathways reflecting decreased lipid synthesis (e.g. *NR1H3, ELOVL6*) and increased fatty acid catabolism through beta oxidation (e.g. *CRAT, ACOX3;* **Fig. 3M; Data S10**), further supporting that ABCA7 LoF neurons may be responding to an increased intracellular lipid burden.

ABCA7 LoF induces mitochondrial dysfunction in excitatory neurons

To test for a link between the observed lipid disruptions in ABCA7 LoF neurons and potential downstream phenotypes, we analyzed a publicly available dataset (*33*) (**Table S2**), which evaluated transcriptomic changes resulting from CRISPRi knockdown of 184 genes in iPSC-derived NGN2 neurons. We tested a subset of these CRISPRi target genes ($|S|>0.5$ and det.rate>0.25 in *post-mortem* Ex, N=59) for perturbation of the eight ABCA7 LoF-associated gene clusters (**Fig. 2E-G**). Cluster 7 was frequently perturbed by CRISPRi target genes (**Fig.**

4A). Expected CRISPRi targets, such as the mitochondrial subunit members *COX15* and *NDUFS8,* led to up-regulation of this cluster, which was characterized by oxidative phosphorylation pathways and genes (*e.g. COX7A2* and *NDUFV2)* (**Fig. 4B,C**). Less expectedly, we found that knock-down of two lipid regulators (the fatty acid elongase *ELOVL5* and the intracellular lipid transporter oxysterol binding protein *OSBPL6*) also caused a significant disruption to cluster 7 (**Fig. 4A**). Our previous analysis suggested disruptions to lipid synthesis, storage, and transport, including the disruption of fatty acid elongases and oxysterol binding proteins in ABCA7 LoF neurons (**Fig. 3M**), which are regulators of TAG burden (*34*, *35*) and lipid transport (*36*), respectively. These data suggest that ABCA7 LoF neurons might experience mitochondrial dysfunction as a direct consequence of observed lipid disruptions.

To examine whether ABCA7 LoF neurons indeed showed evidence for the predicted mitochondrial dysfunction as a direct result of ABCA7 LoF, we derived isogenic neurons from our ABCA7KO#1 line and a second isogenic line ("ABCA7KO#2") which harbors a different ABCA7 LoF variant modeled after a patient SNP (Tyr622*) introducing a premature termination codon in ABCA7 exon 15 (**Fig S8B**). We incubated four week old neurons with HCS Mitochondrial Health dye (ThermoFisher), as a general measure of mitochondrial health and function. The "Mitohealth" dye detects changes in mitochondrial membrane potential, accumulating in active mitochondria. We observed that ABCA7 KO neurons have reduced Mitohealth dye accumulation compared to control neurons within Tuj1 surfaces (**Fig. 4D,E**), indicating reduced mitochondrial function.

Mitochondrial dysfunction often leads to the production and accumulation of reactive oxygen species (*37–39*). To evaluate ROS burden in ABCA7 KO neurons, we treated live neurons with CellROX (ThermoFisher), a live-cell permeant dye that has low fluorescence when in a reduced state and fluoresces brightly upon oxidation. ABCA7 KO neurons had elevated CellROX fluorescence compared to control neurons within Tuj1 surfaces (**Fig. 4F,G**), indicating greater ROS burden and oxidative stress.

ABCA7 LoF induces DNA damage in excitatory neurons

A well-established consequence of mitochondrial dysfunction and ROS production is the accumulation of DNA damage (*38*, *40*, *41*). Studies from our lab and others have shown that neurons are particularly vulnerable to the accumulation of DNA damage (*25*, *42*), a hallmark of AD which can cause neuronal dysfunction and death (*43*, *44*). Therefore, we were particularly intrigued to find multiple DNA damage-related gene clusters perturbed in ABCA7 LoF excitatory neurons (**Fig. 2E-G**). Clusters 1 and 3 included key DNA damage genes, including *TLK2, MSH6, RECQL,* and multiple proteasomal genes, which show evidence for up-regulation in ABCA7 LoF and were characterized by pathways, including "DNA damage response via ATR" and "Homologous recombination" (**Fig. 4H**). Cluster 5 evidenced a number of cell cycle-related gene changes, including *CDC7* and *ORC6* and was characterized by cell cycle-related pathways (**Fig. 4H**). Together, the transcriptional data suggest that ABCA7 LoF neurons may have increased levels of DNA damage.

To test whether ABCA7 LoF carriers suffered greater DNA damage compared to matched controls, we performed the COMET assay under neutral conditions (*45–47*) on fresh frozen PFC from ABCA7 LoF carriers (N=5, 4 female, 1 male) and pathology- and sex-matched control PFC tissue (N=5, 4 female, 1 male). This assay measures the burden of DNA double-stranded breaks

as a function of tail moment, reflecting the migration of damaged DNA under electrophoresis. We isolated and analyzed > 1000 nuclei per genotype, and found ABCA7 LoF carriers indeed show greater tail moment compared to controls, indicating increased DNA damage (**Fig. 4I**).

To test whether increased DNA damage could be a cell-autonomous phenotype, specifically downstream of ABCA7 LoF in neurons, we next performed neutral COMET assays on iPSC-derived neurons. As observed in postmortem tissue, ABCA7 KO#1 neurons had significantly larger tail moments by comet assay (**Fig. 4J**), indicative of greater levels of DNA damage than control neurons.

A recent study from our lab showed that neurons burdened by double-stranded breaks initiate innate anti-viral immune signaling, characterized by NF-kB and interferon activation (*25*, *42*). Interestingly, we observed a number of gene clusters related to immune signaling in ABCA7 LoF neurons (clusters 4 and 6), which were characterized by pro-inflammatory gene changes, including *IKBKB,* an activator of NF-kB, in gene cluster 6 (**Fig. 2E-G; Data S7)**. Directly querying a large database of pathways for NF-kB-related processes, showed several NF-kB pathways with evidence for up-regulation in ABCA7 LoF excitatory neurons (**Fig. S10A; Data S12**). Since NF-kB is a transcriptional master regulator of innate immune signaling (*48*, *49*), we next validated changes of the NF-kB subunit p65, whose localization to the nucleus is indicative of NF-kB activation. We stained PFC brain tissue for p65 and examined whether we could detect differences in intensity within NeuN surfaces. We observed a significant increase in sum intensity of p65 per NeuN volume in our LoF brains compared to controls (**Fig. S10B**), confirming that these neurons are indeed upregulating this key innate immune regulator, as we have recently reported can occur downstream of DNA damage (*25*). ABCA7 KO iPSC-derived neurons also had increased levels of p65 immunofluorescence within Tuj1-positive DAPI surfaces (**Fig. S10C**) compared to control neurons, suggestive of increases in NF-kB inflammatory signaling. Altogether, these data show that ABCA7 LoF causes DNA damage and associated increases in inflammatory signaling.

Discussion

ABCA7 loss-of-function variants have among the highest odds ratios of any known Alzheimer's disease genetic risk factors. Here, we generated an atlas of ABCA7 dysfunction across all major brain cell types, and cataloged a number of perturbations related to lipid disruptions, mitochondrial function, DNA damage, and inflammation.

Previous studies have shown that ABCA7 is highly expressed in microglia and neurons (*15*, *50*, *51*). In our dataset, excitatory neurons showed the highest ABCA7 expression and strong evidence for perturbation by ABCA7 dysfunction, with dysregulated lipid biosynthesis, mitochondrial respiration, DNA repair pathways, and inflammatory signaling. Perturbation of ELOVL5, a fatty acid elongase, in NGN2 neurons and ABCA7 LoF in *post-mortem* excitatory neurons converge onto a shared transcriptomic signature, suggesting that lipid dysregulation may be a primary insult resulting from ABCA7 dysfunction in neurons, upstream of other disruptions in mitochondrial function and DNA repair.

ABCA7 LoF indeed triggers lipidomic changes in both ABCA7 KO neuron monocultures and bulk PFC tissues. Consistent with prior findings that highlight ABCA7's role as a lipid transporter favoring phospholipids (*16*, *17*), we detected shifts in phospholipid levels, particularly in phosphatidylcholine, accompanied by a pronounced increase in triglycerides due to ABCA7 LoF. Our *post-mortem* snRNAseq data suggested that neurons with ABCA7 LoF have

reduced expression of lipid synthesis pathways, including SREBF and ELOVL genes. Prior research indicates that intracellular phosphatidylcholine levels influence the SREBP1-mediated expression of genes tied to fatty acid and phospholipid synthesis, including ELOVLs (*52*). Furthermore, altering phosphatidylcholine synthesis impacts the intracellular accumulation of triglycerides (*52*, *53*). Given that phospholipid synthesis relies on triglyceride lipolysis and the metabolism of shared precursors (*54*, *55*), imbalances in phospholipid sensing and synthesis could result in triglyceride accumulation in ABCA7 LoF neurons (**Fig. S11**).

Accumulation of triglycerides is unusual in neurons, as they are typically rapidly turned over in the production of phospholipids for membrane production and maintenance (*56*, *57*). In other cell types, excess triglycerides can be stored in lipid droplets for later use in energy production (*58*). Neurons likely have a limited capacity for lipid droplet formation (*56*, *58*, *59*), and for fatty acid catabolism due to their sensitivity to byproduct ROS production (*60*, *61*). In the case of ABCA7 LoF neurons, mitochondrial stress may result from catabolism of accumulated triglycerides through increased fatty acid oxidation and result in the detected elevation in ROS (*62*). These ROS may then cascade down, producing DNA damage and inflammation (*63–66*) observed in ABCA7 LoF (**Fig. S11**).

As phospholipids are major components of biological membranes with generalizable functions, the effects of phospholipid changes in ABCA7 LoF may be more difficult to mechanistically associate with other phenotypes. For example, numerous changes in phosphatidylcholines were observed in the ABCA7 LoF lipidome. Phosphatidylcholine is a major component of biological membranes, particularly the plasma membrane (*67*), and is critical during neuronal differentiation (*68*, *69*), axon and neurite growth (*70*, *71*), and adult neuronal health and plasticity (*72*). Additionally, cardiolipin, a metabolite of phosphatidylglycerol, is a major component of the inner mitochondrial membrane. Cardiolipin species were altered in both the ABCA7 KO#1 NGN2 line and *post-mortem* human brain and phosphatidylglycerol showed some evidence of change, however to a lesser extent. Cardiolipin plays a critical role in mitochondrial health. It regulates membrane packing (*73*), plays a role in the electron transport chain (*74–80*), and its externalization to the outer mitochondrial membrane facilitates elimination by mitophagy upon mitochondrial damage (*81*). Furthermore, some phospholipids are capable of binding to nuclear receptors to affect downstream signaling cascades and transcriptional programs (*82*).

Lipid disruptions have long been evident in Alzheimer's disease, with lipid accumulation in AD postmortem brains first described by Alois Alzheimer in 1907, and by others more recently (*83*, *84*). Alzheimer's disease has also been associated with altered phospholipid (*85–89*) and fatty acid (*90*) metabolism. Genes that perturb lipid metabolism make up a significant subset of known AD risk genes, including genes involved in lipid synthesis, such as SREBF2 (*91*), lipid sensing and lipid-mediated inflammatory transition such as TREM2 (*92–94*), and lipid trafficking such as APOE, CLU, ABCA1 and ABCA7 (*95*). Moreover, AD risk genes whose canonical functions include vesicular trafficking, such as PICALM, or inflammation, such as SPI1, also heavily influence and are influenced by lipid metabolism (*96*, *97*). The strongest known AD genetic risk factor, the ε4 allele of APOE, has received significant attention since its discovery almost 3 decades ago (*98*), and is associated with lipid disruptions in multiple glial cell types (*53*, *99–101*).

Lipid metabolism and dysregulation is therefore critical in AD pathogenesis. Improved understanding of the genetic contributions to these individual lipid-associated risk factors and their interactions will improve our understanding of disease pathogenesis and potential interventions. While the ABCA7 LoF mutations studied here are relatively rare, low impact but

common missense variants (i.e. rs3752245: MAF=circa 0.18, OR=1.15 (1.11-1.18) (*5*, *12*); rs72973581: MAF=circa 0.6, OR=0.57 (0.41-0.80) (*12*, *102*)) in ABCA7 have also been associated with increased risk for AD, and likely cause perturbations reflective of those described in this study. Perhaps heightened through genetic interactions with other risk factors, including APOE, ABCA7 dysfunction could play a pathogenic role in a significant subset of AD cases.

Acknowledgments: We thank the individuals who donated *post-mortem* brain samples, and their families, for enabling this research; Y. Zhou, E. McNamara and T. Garvey for administrative support and animal care; the MIT SuperCloud and Lincoln Laboratory Supercomputing Center for providing HPC and consultation resources that have contributed to the research results reported within this paper; the Harvard Center for Mass Spectrometry (HCMS) for lipidomic sample runs and Charles Vidoudez (HCMS) for consultation on the lipidomic data analysis. ROSMAP resources can be requested at https://www.radc.rush.edu. Graphic illustrations were generated using BioRender under agreement # X25SQ61W7.

Funding:

This work was supported in part by the Cure Alzheimer's Fund, the JBP Foundation and NIH grants RF1AG062377, RF1 AG054321, RO1 AG054012, RO1 AG075901 (L.-H.T.)

Author contributions:

Conceptualization: DVM, JMB, L-HT, SEW

Data curation: DVM, JMB, SEW

Formal analysis: DVM

Methodology: DVM, JMB, SEW, HM, GL

Investigation: DVM, JMB, SEW, HM, AN, XJ, SM, GW, NL

Visualization: DVM, JMB, SEW

Funding acquisition: L-HT, MK

Writing – original draft: DVM, SEW

Writing – review & editing: DVM, SEW, JMB

Competing interests: Authors declare that they have no competing interests.

Data and materials availability: Analysis code to repeat any computational and analysis steps on the WGS, single-cell, or lipidomic datasets will be available on Github: https://github.com/djunamay/ABCA7lof2. Code to access the WGS data is available on Github: https://github.com/djunamay/ROSMAPwgs. Code to perform the gene-pathway clustering is available on Github: https://github.com/djunamay/geneclusters. Raw and processed single cell data, human *post-mortem* lipidomic data, and patient metadata will be deposited on Synapse. All other data are available through the open science framework: https://osf.io/vn7w2/ and in the supplementary materials of this manuscript.

Supplementary Materials

Materials and Methods

Supplementary Text

Figs. S1 to S11

Tables S1 to S3

References (*1-21*)

Data S1 to S12

Fig. 1. Single-nuclear RNA-sequencing of human postmortem prefrontal cortex reveals cell type-specific gene changes in ABCA7 LoF variant carriers. (A) Overview of human cohort for snRNAseq and distribution of ABCA7 LoF variants (c.3641G>A, stop gained, pink; c.3255G>A, stop gained, dark green; c.4208delT, frameshift, yellow; c.2126_2132del, frameshift, orange; c.5570+5G>C, splice region, purple; c.4416+2T>G, splice region, green) (Created with BioRender.com). (B) ABCA7 gene structure with color-coded arrows indicating location of variants from (A). Exons are indicated as black rectangles, and introns as black lines. (C) Two-dimensional UMAP projection of per-cell gene expression values from snRNA-sequencing of *post-mortem* prefrontal cortex samples from cohort in (A), and their transcriptionally-defined cell type. (D) Cartoon overview of DEG analysis strategy (also **see Methods**)(Created with BioRender.com). Genes from cell-type-specific ABCA7 LoF perturbation score space were projected onto the first two UMAP dimensions, followed by clustering and pathway enrichment to provide a unified visual overview of gene expression changes associated with ABCA7 LoF across all major cell types. (E) 2D UMAP projection of indicated cell type-specific per-gene ABCA7 LoF perturbation scores (*S*) (*S* = -log10(p-value)*sign(log2FC); Red = score>1.3, Blue = score<-1.3; Point size indicates |S|). Up to top 20 genes by |S| are labeled. (F) Genes in 2D UMAP space colored by cluster assignment (Gaussian mixture model, **see Methods**). (G) Per-cluster pathway enrichments for clusters in (F) (GO BP, hypergeometric enrichment, p<0.01). (H) Cell type-specific gene cluster scores ($S_C=mean(S_i)$, for genes i in cluster c). * indicates permutation FDR-adjusted p-value < 0.01 & $|S_C|>0.25$.

Fig. 2. Excitatory neuronal gene cluster analysis reveals ABCA7 LoF perturbations. (A) 2D projection of individual cells colored by log(Exp=log-normalized ABCA7 expression values). (B) Per cell type ABCA7 detection rate of the *post-mortem* PFC as quantified by snRNAseq. (C) Top perturbed pathways (WikiPathways, GSEA, p<0.025) in ABCA7 LoF Excitatory neurons. (D) Cartoon overview of graph partitioning strategy using Kernighan-Lin algorithm (Created with BioRender.com). (E) Kernighan-Lin (KL) clustering on leading edge genes from pathways in (C), where p<0.05. Colors indicate distinct KL clusters. (F) Distributions of gene scores *S* for genes belonging to a given gene cluster. Solid lines indicate distribution means. (G) Representative pathways that annotate the largest number of genes within a cluster (i.e. with the highest intra-cluster connectivity) shown per-cluster.

Fig. 3. ABCA7 LoF perturbs neutral- and phospho-lipid homeostasis in neurons. (A) Members of KL cluster 2 are highlighted in orange. (B) Representative pathways of cluster 2 inferred from graph. Average *S* for all cluster 2 member genes connected to that pathway are shown. (C) Top gene changes in network cluster 2 by |*S*|. (D) ABCA7 gene map depicts exons (black rectangles) and introns (black lines). CRISPR-Cas9 was used to generate an ABCA7 loss-of-function isogenic iPSC line by introducing a premature termination codon into exon 3 (ABCA7 KO#1, blue). (E) iPSCs were plated at low density for NGN2 viral transduction. Expression of NGN2 was driven by doxycycline (DOX) induction with puromycin (PURO) selection, then re-plated to match neuronal densities. Neurons were maintained for 4 weeks (DIV 28) before experimentation (Created with BioRender.com). (F) Projection of control and ABCA7KO#1 lipidomes (N=6 per genotype) onto the first two principal components from lipid space. Fraction of explained variance is shown along each axis. (G) Percentage of lipid species by major lipid class that show up- (p<5e-3 & fold-change>0, T-test) or down-regulation (p<5e-3 & fold-change<0, T-test) in KO#1 vs WT, where fold-change>0 indicates up-regulation in KO#1 compared to WT. Major class: NL=neutral lipids; PL=phospholipids; SL=sphingolipids;

GL=Glycoglycerolipids; FA=fatty acyl and other lipids. Subclass lipid names (TG, MG, e.t.c.) are shown in table H. (H) Overview of perturbed lipid species by lipid subclass. U=# of lipids in that subclass where p<5e-3 & fold-change>0. D=# of lipids in that subclass where p<5e-3 & fold-change<0. T=U+D. %=(T/N)*100, where N=total # of lipids in given subclass. "Hex1Cer" and "Cer" are sphingolipids (not shown in G). (I,J). Volcano plot showing distribution of triglyceride (TAG) species (I) and phosphatidylcholine (PC) species (J) by log-fold-change and log-p-value, where log-fold-change > 0 indicates up-regulation in KO#1(N=6) vs WT (N=6). A subset of lipid species are labeled (p<0.05 & logFC>2 (red) or logFC<-2 (blue). (K,L) Volcano plot showing distribution of triglyceride (TAG) species (K) and phosphatidylcholine species (L) by log-fold-change and log-p-value, where log-fold-change > 0 indicates up-regulation in ABCA7 LoF *post-mortem* PFC (N=8) vs Control (N=8). A subset of lipid species are labeled (p<0.1 & logFC>0.5 (red) or logFC<-0.5 (blue) (T-test). (M) Top lipid-specific pathway changes in excitatory neurons (when considering a large database of pathways, **see Methods**; p<0.025). *Score=sign(enrichment score)*-log10(p-value);* GSEA*; Score>0* indicates up in ABCA7 LoF excitatory neurons *vs* control.

Fig. 4. ABCA7 LoF in excitatory neurons induces mitochondrial dysfunction, oxidative stress, and DNA damage. (A) CRISPRi target genes (from (*33*)) that show perturbation of cluster 7 (GSEA, p<1e-3) and that have a det.rate > 0.25 in excitatory neurons (by *post-mortem* snRNAseq) and an ABCA7 LoF perturbation score |S|>0.5. (B) Members of KL clusters 1, 3, 5, and 7 are highlighted in blue, orange, green, and pink, respectively. (C) Representative pathways of cluster 7 inferred from graph (see **Methods**). Top gene changes in network cluster 7 by *S* are shown on the right. (D) Representative confocal images of Mitohealth (greyscale) signal in control, ABCA7 KO#1 and KO#2 iPSC-derived neurons co-stained for Tuj1 (green) and DAPI (blue). 20X images, Scale bars, 50 µm. (E) Quantification of Mitohealth fluorescence intensity (control: n=267; ABCA7 KO#1: n=227; ABCA7 KO#2: n=270) (KO#1: P<0.0001; KO#2: P<0.0001). (F) Representative confocal images of CellROX (greyscale) signal in control, ABCA7 KO#1 and KO#2 iPSC-derived neurons co-stained for Tuj1 (green) and DAPI (blue). 20X images, Scale bars, 50 µm. (G) Quantification of CellROX fluorescence intensity (control: n=220; ABCA7 KO#1: n=231; ABCA7 KO#2: n=252) (KO#1: P=0.0003; KO#2: P<0.0001). n=number of neurons, ***P<0.001, ****P<0.0001. (H) Representative pathways of clusters 1, 3, and 5 inferred from graph (see **Methods**). Top gene changes by *S* are shown on the right. (I) Left: representative confocal images of comet assay tail moments from control and ABCA7 loss-of-function (LoF) prefrontal cortex nuclei. 20X images. Right: Quantification of tail moment at left (control: n=1187; ABCA7 LoF: n=1352; n=number of cells) (P<0.0001). (J) Left: representative confocal images of comet assay tail moments from control and ABCA7 KO#1 iPSC-derived neurons. 20X images. Right: Quantification of tail moment at left (control: n=97; ABCA7 KO#1: n=49) (P<0.0001).

1. Alzheimer's Association, 2016 Alzheimer's disease facts and figures. *Wiley Online Library* (2016), , doi:10.1016/j.jalz.2016.03.001.

2. J. C. Lambert, C. A. Ibrahim-Verbaas, D. Harold, A. C. Naj, R. Sims, C. Bellenguez, A. L. DeStafano, J. C. Bis, G. W. Beecham, B. Grenier-Boley, G. Russo, T. A. Thorton-Wells, N. Jones, A. V. Smith, V. Chouraki, C. Thomas, M. A. Ikram, D. Zelenika, B. N. Vardarajan, Y. Kamatani, C. F. Lin, A. Gerrish, H. Schmidt, B. Kunkle, M. L. Dunstan, A. Ruiz, M. T. Bihoreau, S. H. Choi, C. Reitz, F. Pasquier, C. Cruchaga, D. Craig, N. Amin, C. Berr, O. L. Lopez, P. L. De Jager, V. Deramecourt, J. A. Johnston, D. Evans, S. Lovestone, L. Letenneur, F. J. Morón, D. C. Rubinsztein, G. Eiriksdottir, K. Sleegers, A. M. Goate, N. Fiévet, M. W. Huentelman, M. Gill, K. Brown, M. I. Kamboh, L. Keller, P. Barberger-Gateau, B. McGuiness, E. B. Larson, R. Green, A. J. Myers, C. Dufouil, S. Todd, D. Wallon, S. Love, E. Rogaeva, J. Gallacher, P. St George-Hyslop, J. Clarimon, A. Lleo, A. Bayer, D. W. Tsuang, L. Yu, M. Tsolaki, P. Bossù, G. Spalletta, P. Proitsi, J. Collinge, S. Sorbi, F. Sanchez-Garcia, N. C. Fox, J. Hardy, M. C. Deniz Naranjo, P. Bosco, R. Clarke, C. Brayne, D. Galimberti, M. Mancuso, F. Matthews, European Alzheimer's Disease Initiative (EADI), Genetic and Environmental Risk in Alzheimer's Disease, Alzheimer's Disease Genetic Consortium, Cohorts for Heart and Aging Research in Genomic Epidemiology, S. Moebus, P. Mecocci, M. Del Zompo, W. Maier, H. Hampel, A. Pilotto, M. Bullido, F. Panza, P. Caffarra, B. Nacmias, J. R. Gilbert, M. Mayhaus, L. Lannefelt, H. Hakonarson, S. Pichler, M. M. Carrasquillo, M. Ingelsson, D. Beekly, V. Alvarez, F. Zou, O. Valladares, S. G. Younkin, E. Coto, K. L. Hamilton-Nelson, W. Gu, C. Razquin, P. Pastor, I. Mateo, M. J. Owen, K. M. Faber, P. V. Jonsson, O. Combarros, M. C. O'Donovan, L. B. Cantwell, H. Soininen, D. Blacker, S. Mead, T. H. Mosley Jr, D. A. Bennett, T. B. Harris, L. Fratiglioni, C. Holmes, R. F. de Bruijn, P. Passmore, T. J. Montine, K. Bettens, J. I. Rotter, A. Brice, K. Morgan, T. M. Foroud, W. A. Kukull, D. Hannequin, J. F. Powell, M. A. Nalls, K. Ritchie, K. L. Lunetta, J. S. Kauwe, E. Boerwinkle, M. Riemenschneider, M. Boada, M. Hiltuenen, E. R. Martin, R. Schmidt, D. Rujescu, L. S. Wang, J. F. Dartigues, R. Mayeux, C. Tzourio, A. Hofman, M. M. Nöthen, C. Graff, B. M. Psaty, L. Jones, J. L. Haines, P. A. Holmans, M. Lathrop, M. A. Pericak-Vance, L. J. Launer, L. A. Farrer, C. M. van Duijn, C. Van Broeckhoven, V. Moskvina, S. Seshadri, J. Williams, G. D. Schellenberg, P. Amouyel, Meta-analysis of 74,046 individuals identifies 11 new susceptibility loci for Alzheimer's disease. *Nat. Genet.* **45**, 1452–1458 (2013).

3. R. E. Marioni, S. E. Harris, Q. Zhang, A. F. McRae, S. P. Hagenaars, W. D. Hill, G. Davies, C. W. Ritchie, C. R. Gale, J. M. Starr, A. M. Goate, D. J. Porteous, J. Yang, K. L. Evans, I. J. Deary, N. R. Wray, P. M. Visscher, Correction: GWAS on family history of Alzheimer's disease. *Transl. Psychiatry*. **9**, 161 (2019).

4. I. E. Jansen, J. E. Savage, K. Watanabe, J. Bryois, D. M. Williams, S. Steinberg, J. Sealock, I. K. Karlsson, S. Hägg, L. Athanasiu, N. Voyle, P. Proitsi, A. Witoelar, S. Stringer, D. Aarsland, I. S. Almdahl, F. Andersen, S. Bergh, F. Bettella, S. Bjornsson, A. Brækhus, G. Bråthen, C. de Leeuw, R. S. Desikan, S. Djurovic, L. Dumitrescu, T. Fladby, T. J. Hohman, P. V. Jonsson, S. J. Kiddle, A. Rongve, I. Saltvedt, S. B. Sando, G. Selbæk, M. Shoai, N. G. Skene, J. Snaedal, E. Stordal, I. D. Ulstein, Y. Wang, L. R. White, J. Hardy, J. Hjerling-Leffler, P. F. Sullivan, W. M. van der Flier, R. Dobson, L. K. Davis, H. Stefansson, K. Stefansson, N. L. Pedersen, S. Ripke, O. A. Andreassen, D. Posthuma, Genome-wide meta-analysis identifies new loci and functional pathways influencing Alzheimer's disease

risk. *Nat. Genet.* **51**, 404–413 (2019).

5. B. W. Kunkle, B. Grenier-Boley, R. Sims, J. C. Bis, V. Damotte, A. C. Naj, A. Boland, M. Vronskaya, S. J. van der Lee, A. Amlie-Wolf, C. Bellenguez, A. Frizatti, V. Chouraki, E. R. Martin, K. Sleegers, N. Badarinarayan, J. Jakobsdottir, K. L. Hamilton-Nelson, S. Moreno-Grau, R. Olaso, R. Raybould, Y. Chen, A. B. Kuzma, M. Hiltunen, T. Morgan, S. Ahmad, B. N. Vardarajan, J. Epelbaum, P. Hoffmann, M. Boada, G. W. Beecham, J.-G. Garnier, D. Harold, A. L. Fitzpatrick, O. Valladares, M.-L. Moutet, A. Gerrish, A. V. Smith, L. Qu, D. Bacq, N. Denning, X. Jian, Y. Zhao, M. Del Zompo, N. C. Fox, S.-H. Choi, I. Mateo, J. T. Hughes, H. H. Adams, J. Malamon, F. Sanchez-Garcia, Y. Patel, J. A. Brody, B. A. Dombroski, M. C. D. Naranjo, M. Daniilidou, G. Eiriksdottir, S. Mukherjee, D. Wallon, J. Uphill, T. Aspelund, L. B. Cantwell, F. Garzia, D. Galimberti, E. Hofer, M. Butkiewicz, B. Fin, E. Scarpini, C. Sarnowski, W. S. Bush, S. Meslage, J. Kornhuber, C. C. White, Y. Song, R. C. Barber, S. Engelborghs, S. Sordon, D. Voijnovic, P. M. Adams, R. Vandenberghe, M. Mayhaus, L. A. Cupples, M. S. Albert, P. P. De Deyn, W. Gu, J. J. Himali, D. Beekly, A. Squassina, A. M. Hartmann, A. Orellana, D. Blacker, E. Rodriguez-Rodriguez, S. Lovestone, M. E. Garcia, R. S. Doody, C. Munoz-Fernadez, R. Sussams, H. Lin, T. J. Fairchild, Y. A. Benito, C. Holmes, H. Karamujić-Čomić, M. P. Frosch, H. Thonberg, W. Maier, G. Roshchupkin, B. Ghetti, V. Giedraitis, A. Kawalia, S. Li, R. M. Huebinger, L. Kilander, S. Moebus, I. Hernández, M. I. Kamboh, R. Brundin, J. Turton, Q. Yang, M. J. Katz, L. Concari, J. Lord, A. S. Beiser, C. D. Keene, S. Helisalmi, I. Kloszewska, W. A. Kukull, A. M. Koivisto, A. Lynch, L. Tarraga, E. B. Larson, A. Haapasalo, B. Lawlor, T. H. Mosley, R. B. Lipton, V. Solfrizzi, M. Gill, W. T. Longstreth Jr, T. J. Montine, V. Frisardi, M. Diez-Fairen, F. Rivadeneira, R. C. Petersen, V. Deramecourt, I. Alvarez, F. Salani, A. Ciaramella, E. Boerwinkle, E. M. Reiman, N. Fievet, J. I. Rotter, J. S. Reisch, O. Hanon, C. Cupidi, A. G. Andre Uitterlinden, D. R. Royall, C. Dufouil, R. G. Maletta, I. de Rojas, M. Sano, A. Brice, R. Cecchetti, P. S. George-Hyslop, K. Ritchie, M. Tsolaki, D. W. Tsuang, B. Dubois, D. Craig, C.-K. Wu, H. Soininen, D. Avramidou, R. L. Albin, L. Fratiglioni, A. Germanou, L. G. Apostolova, L. Keller, M. Koutroumani, S. E. Arnold, F. Panza, O. Gkatzima, S. Asthana, D. Hannequin, P. Whitehead, C. S. Atwood, P. Caffarra, H. Hampel, I. Quintela, Á. Carracedo, L. Lannfelt, D. C. Rubinsztein, L. L. Barnes, F. Pasquier, L. Frölich, S. Barral, B. McGuinness, T. G. Beach, J. A. Johnston, J. T. Becker, P. Passmore, E. H. Bigio, J. M. Schott, T. D. Bird, J. D. Warren, B. F. Boeve, M. K. Lupton, J. D. Bowen, P. Proitsi, A. Boxer, J. F. Powell, J. R. Burke, J. S. K. Kauwe, J. M. Burns, M. Mancuso, J. D. Buxbaum, U. Bonuccelli, N. J. Cairns, A. McQuillin, C. Cao, G. Livingston, C. S. Carlson, N. J. Bass, C. M. Carlsson, J. Hardy, R. M. Carney, J. Bras, M. M. Carrasquillo, R. Guerreiro, M. Allen, H. C. Chui, E. Fisher, C. Masullo, E. A. Crocco, C. DeCarli, G. Bisceglio, M. Dick, L. Ma, R. Duara, N. R. Graff-Radford, D. A. Evans, A. Hodges, K. M. Faber, M. Scherer, K. B. Fallon, M. Riemenschneider, D. W. Fardo, R. Heun, M. R. Farlow, H. Kölsch, S. Ferris, M. Leber, T. M. Foroud, I. Heuser, D. R. Galasko, I. Giegling, M. Gearing, M. Hüll, D. H. Geschwind, J. R. Gilbert, J. Morris, R. C. Green, K. Mayo, J. H. Growdon, T. Feulner, R. L. Hamilton, L. E. Harrell, D. Drichel, L. S. Honig, T. D. Cushion, M. J. Huentelman, P. Hollingworth, C. M. Hulette, B. T. Hyman, R. Marshall, G. P. Jarvik, A. Meggy, E. Abner, G. E. Menzies, L.-W. Jin, G. Leonenko, L. M. Real, G. R. Jun, C. T. Baldwin, D. Grozeva, A. Karydas, G. Russo, J. A. Kaye, R. Kim, F. Jessen, N. W. Kowall, B. Vellas, J. H. Kramer, E. Vardy, F. M. LaFerla, K.-H. Jöckel, J. J. Lah, M. Dichgans, J. B. Leverenz, D. Mann, A. I. Levey, S. Pickering-Brown, A. P. Lieberman, N. Klopp, K. L. Lunetta, H.-E. Wichmann, C. G. Lyketsos, K. Morgan, D. C. Marson, K.

Brown, F. Martiniuk, C. Medway, D. C. Mash, M. M. Nöthen, E. Masliah, N. M. Hooper, W. C. McCormick, A. Daniele, S. M. McCurry, A. Bayer, A. N. McDavid, J. Gallacher, A. C. McKee, H. van den Bussche, M. Mesulam, C. Brayne, B. L. Miller, S. Riedel-Heller, C. A. Miller, J. W. Miller, A. Al-Chalabi, J. C. Morris, C. E. Shaw, A. J. Myers, J. Wiltfang, S. O'Bryant, J. M. Olichney, V. Alvarez, J. E. Parisi, A. B. Singleton, H. L. Paulson, J. Collinge, W. R. Perry, S. Mead, E. Peskind, D. H. Cribbs, M. Rossor, A. Pierce, N. S. Ryan, W. W. Poon, B. Nacmias, H. Potter, S. Sorbi, J. F. Quinn, E. Sacchinelli, A. Raj, G. Spalletta, M. Raskind, C. Caltagirone, P. Bossù, M. D. Orfei, B. Reisberg, R. Clarke, C. Reitz, A. D. Smith, J. M. Ringman, D. Warden, E. D. Roberson, G. Wilcock, E. Rogaeva, A. C. Bruni, H. J. Rosen, M. Gallo, R. N. Rosenberg, Y. Ben-Shlomo, M. A. Sager, P. Mecocci, A. J. Saykin, P. Pastor, M. L. Cuccaro, J. M. Vance, J. A. Schneider, L. S. Schneider, S. Slifer, W. W. Seeley, A. G. Smith, J. A. Sonnen, S. Spina, R. A. Stern, R. H. Swerdlow, M. Tang, R. E. Tanzi, J. Q. Trojanowski, J. C. Troncoso, V. M. Van Deerlin, L. J. Van Eldik, H. V. Vinters, J. P. Vonsattel, S. Weintraub, K. A. Welsh-Bohmer, K. C. Wilhelmsen, J. Williamson, T. S. Wingo, R. L. Woltjer, C. B. Wright, C.-E. Yu, L. Yu, Y. Saba, A. Pilotto, M. J. Bullido, O. Peters, P. K. Crane, D. Bennett, P. Bosco, E. Coto, V. Boccardi, P. L. De Jager, A. Lleo, N. Warner, O. L. Lopez, M. Ingelsson, P. Deloukas, C. Cruchaga, C. Graff, R. Gwilliam, M. Fornage, A. M. Goate, P. Sanchez-Juan, P. G. Kehoe, N. Amin, N. Ertekin-Taner, C. Berr, S. Debette, S. Love, L. J. Launer, S. G. Younkin, J.-F. Dartigues, C. Corcoran, M. A. Ikram, D. W. Dickson, G. Nicolas, D. Campion, J. Tschanz, H. Schmidt, H. Hakonarson, J. Clarimon, R. Munger, R. Schmidt, L. A. Farrer, C. Van Broeckhoven, M. C O'Donovan, A. L. DeStefano, L. Jones, J. L. Haines, J.-F. Deleuze, M. J. Owen, V. Gudnason, R. Mayeux, V. Escott-Price, B. M. Psaty, A. Ramirez, L.-S. Wang, A. Ruiz, C. M. van Duijn, P. A. Holmans, S. Seshadri, J. Williams, P. Amouyel, G. D. Schellenberg, J.-C. Lambert, M. A. Pericak-Vance, Alzheimer Disease Genetics Consortium (ADGC), European Alzheimer's Disease Initiative (EADI), Cohorts for Heart and Aging Research in Genomic Epidemiology Consortium (CHARGE),, Genetic and Environmental Risk in AD/Defining Genetic, Polygenic and Environmental Risk for Alzheimer's Disease Consortium (GERAD/PERADES), Genetic meta-analysis of diagnosed Alzheimer's disease identifies new risk loci and implicates Aβ, tau, immunity and lipid processing. *Nat. Genet.* **51**, 414–430 (2019).

6. I. de Rojas, S. Moreno-Grau, N. Tesi, B. Grenier-Boley, V. Andrade, I. E. Jansen, N. L. Pedersen, N. Stringa, A. Zettergren, I. Hernández, L. Montrreal, C. Antúnez, A. Antonell, R. M. Tankard, J. C. Bis, R. Sims, C. Bellenguez, I. Quintela, A. González-Perez, M. Calero, E. Franco-Macías, J. Macías, R. Blesa, L. Cervera-Carles, M. Menéndez-González, A. Frank-García, J. L. Royo, F. Moreno, R. Huerto Vilas, M. Baquero, M. Diez-Fairen, C. Lage, S. García-Madrona, P. García-González, E. Alarcón-Martín, S. Valero, O. Sotolongo-Grau, A. Ullgren, A. C. Naj, A. W. Lemstra, A. Benaque, A. Pérez-Cordón, A. Benussi, A. Rábano, A. Padovani, A. Squassina, A. de Mendonça, A. Arias Pastor, A. A. L. Kok, A. Meggy, A. B. Pastor, A. Espinosa, A. Corma-Gómez, A. Martín Montes, Á. Sanabria, A. L. DeStefano, A. Schneider, A. Haapasalo, A. Kinhult Ståhlbom, A. Tybjærg-Hansen, A. M. Hartmann, A. Spottke, A. Corbatón-Anchuelo, A. Rongve, B. Borroni, B. Arosio, B. Nacmias, B. G. Nordestgaard, B. W. Kunkle, C. Charbonnier, C. Abdelnour, C. Masullo, C. Martínez Rodríguez, C. Muñoz-Fernandez, C. Dufouil, C. Graff, C. B. Ferreira, C. Chillotti, C. A. Reynolds, C. Fenoglio, C. Van Broeckhoven, C. Clark, C. Pisanu, C. L. Satizabal, C. Holmes, D. Buiza-Rueda, D. Aarsland, D. Rujescu, D. Alcolea, D. Galimberti, D. Wallon, D. Seripa, E. Grünblatt, E. Dardiotis, E. Düzel, E. Scarpini, E.

Conti, E. Rubino, E. Gelpi, E. Rodriguez-Rodriguez, E. Duron, E. Boerwinkle, E. Ferri, F. Tagliavini, F. Küçükali, F. Pasquier, F. Sanchez-Garcia, F. Mangialasche, F. Jessen, G. Nicolas, G. Selbæk, G. Ortega, G. Chêne, G. Hadjigeorgiou, G. Rossi, G. Spalletta, G. Giaccone, G. Grande, G. Binetti, G. Papenberg, H. Hampel, H. Bailly, H. Zetterberg, H. Soininen, I. K. Karlsson, I. Alvarez, I. Appollonio, I. Giegling, I. Skoog, I. Saltvedt, I. Rainero, I. Rosas Allende, J. Hort, J. Diehl-Schmid, J. Van Dongen, J.-S. Vidal, J. Lehtisalo, J. Wiltfang, J. Q. Thomassen, J. Kornhuber, J. L. Haines, J. Vogelgsang, J. A. Pineda, J. Fortea, J. Popp, J. Deckert, K. Buerger, K. Morgan, K. Fließbach, K. Sleegers, L. Molina-Porcel, L. Kilander, L. Weinhold, L. A. Farrer, L.-S. Wang, L. Kleineidam, L. Farotti, L. Parnetti, L. Tremolizzo, L. Hausner, L. Benussi, L. Froelich, M. A. Ikram, M. C. Deniz-Naranjo, M. Tsolaki, M. Rosende-Roca, M. Löwenmark, M. Hulsman, M. Spallazzi, M. A. Pericak-Vance, M. Esiri, M. Bernal Sánchez-Arjona, M. C. Dalmasso, M. T. Martínez-Larrad, M. Arcaro, M. M. Nöthen, M. Fernández-Fuertes, M. Dichgans, M. Ingelsson, M. J. Herrmann, M. Scherer, M. Vyhnalek, M. H. Kosmidis, M. Yannakoulia, M. Schmid, M. Ewers, M. T. Heneka, M. Wagner, M. Scamosci, M. Kivipelto, M. Hiltunen, M. Zulaica, M. Alegret, M. Fornage, N. Roberto, N. M. van Schoor, N. M. Seidu, N. Banaj, N. J. Armstrong, N. Scarmeas, N. Scherbaum, O. Goldhardt, O. Hanon, O. Peters, O. A. Skrobot, O. Quenez, O. Lerch, P. Bossù, P. Caffarra, P. Dionigi Rossi, P. Sakka, P. Mecocci, P. Hoffmann, P. A. Holmans, P. Fischer, P. Riederer, Q. Yang, R. Marshall, R. N. Kalaria, R. Mayeux, R. Vandenberghe, R. Cecchetti, R. Ghidoni, R. Frikke-Schmidt, S. Sorbi, S. Hägg, S. Engelborghs, S. Helisalmi, S. Botne Sando, S. Kern, S. Archetti, S. Boschi, S. Fostinelli, S. Gil, S. Mendoza, S. Mead, S. Ciccone, S. Djurovic, S. Heilmann-Heimbach, S. Riedel-Heller, T. Kuulasmaa, T. Del Ser, T. Lebouvier, T. Polak, T. Ngandu, T. Grimmer, V. Bessi, V. Escott-Price, V. Giedraitis, V. Deramecourt, W. Maier, X. Jian, Y. A. L. Pijnenburg, EADB contributors, GR@ACE study group, DEGESCO consortium, IGAP (ADGC, CHARGE, EADI, GERAD), PGC-ALZ consortia, P. G. Kehoe, G. Garcia-Ribas, P. Sánchez-Juan, P. Pastor, J. Pérez-Tur, G. Piñol-Ripoll, A. Lopez de Munain, J. M. García-Alberca, M. J. Bullido, V. Álvarez, A. Lleó, L. M. Real, P. Mir, M. Medina, P. Scheltens, H. Holstege, M. Marquié, M. E. Sáez, Á. Carracedo, P. Amouyel, G. D. Schellenberg, J. Williams, S. Seshadri, C. M. van Duijn, K. A. Mather, R. Sánchez-Valle, M. Serrano-Ríos, A. Orellana, L. Tárraga, K. Blennow, M. Huisman, O. A. Andreassen, D. Posthuma, J. Clarimón, M. Boada, W. M. van der Flier, A. Ramirez, J.-C. Lambert, S. J. van der Lee, A. Ruiz, Common variants in Alzheimer's disease and risk stratification by polygenic risk scores. *Nat. Commun.* **12**, 3417 (2021).

7. D. P. Wightman, I. E. Jansen, J. E. Savage, A. A. Shadrin, S. Bahrami, D. Holland, A. Rongve, S. Børte, B. S. Winsvold, O. K. Drange, A. E. Martinsen, A. H. Skogholt, C. Willer, G. Bråthen, I. Bosnes, J. B. Nielsen, L. G. Fritsche, L. F. Thomas, L. M. Pedersen, M. E. Gabrielsen, M. B. Johnsen, T. W. Meisingset, W. Zhou, P. Proitsi, A. Hodges, R. Dobson, L. Velayudhan, K. Heilbron, A. Auton, 23andMe Research Team, J. M. Sealock, L. K. Davis, N. L. Pedersen, C. A. Reynolds, I. K. Karlsson, S. Magnusson, H. Stefansson, S. Thordardottir, P. V. Jonsson, J. Snaedal, A. Zettergren, I. Skoog, S. Kern, M. Waern, H. Zetterberg, K. Blennow, E. Stordal, K. Hveem, J.-A. Zwart, L. Athanasiu, P. Selnes, I. Saltvedt, S. B. Sando, I. Ulstein, S. Djurovic, T. Fladby, D. Aarsland, G. Selbæk, S. Ripke, K. Stefansson, O. A. Andreassen, D. Posthuma, A genome-wide association study with 1,126,563 individuals identifies new risk loci for Alzheimer's disease. *Nat. Genet.* **53**, 1276–1282 (2021).

8. C. Bellenguez, F. Küçükali, I. E. Jansen, L. Kleineidam, S. Moreno-Grau, N. Amin, A. C. Naj, R. Campos-Martin, B. Grenier-Boley, V. Andrade, P. A. Holmans, A. Boland, V. Damotte, S. J. van der Lee, M. R. Costa, T. Kuulasmaa, Q. Yang, I. de Rojas, J. C. Bis, A. Yaqub, I. Prokic, J. Chapuis, S. Ahmad, V. Giedraitis, D. Aarsland, P. Garcia-Gonzalez, C. Abdelnour, E. Alarcón-Martín, D. Alcolea, M. Alegret, I. Alvarez, V. Álvarez, N. J. Armstrong, A. Tsolaki, C. Antúnez, I. Appollonio, M. Arcaro, S. Archetti, A. A. Pastor, B. Arosio, L. Athanasiu, H. Bailly, N. Banaj, M. Baquero, S. Barral, A. Beiser, A. B. Pastor, J. E. Below, P. Benchek, L. Benussi, C. Berr, C. Besse, V. Bessi, G. Binetti, A. Bizarro, R. Blesa, M. Boada, E. Boerwinkle, B. Borroni, S. Boschi, P. Bossù, G. Bråthen, J. Bressler, C. Bresner, H. Brodaty, K. J. Brookes, L. I. Brusco, D. Buiza-Rueda, K. Bûrger, V. Burholt, W. S. Bush, M. Calero, L. B. Cantwell, G. Chene, J. Chung, M. L. Cuccaro, Á. Carracedo, R. Cecchetti, L. Cervera-Carles, C. Charbonnier, H.-H. Chen, C. Chillotti, S. Ciccone, J. A. H. R. Claassen, C. Clark, E. Conti, A. Corma-Gómez, E. Costantini, C. Custodero, D. Daian, M. C. Dalmasso, A. Daniele, E. Dardiotis, J.-F. Dartigues, P. P. de Deyn, K. de Paiva Lopes, L. D. de Witte, S. Debette, J. Deckert, T. Del Ser, N. Denning, A. DeStefano, M. Dichgans, J. Diehl-Schmid, M. Diez-Fairen, P. D. Rossi, S. Djurovic, E. Duron, E. Düzel, C. Dufouil, G. Eiriksdottir, S. Engelborghs, V. Escott-Price, A. Espinosa, M. Ewers, K. M. Faber, T. Fabrizio, S. F. Nielsen, D. W. Fardo, L. Farotti, C. Fenoglio, M. Fernández-Fuertes, R. Ferrari, C. B. Ferreira, E. Ferri, B. Fin, P. Fischer, T. Fladby, K. Fließbach, B. Fongang, M. Fornage, J. Fortea, T. M. Foroud, S. Fostinelli, N. C. Fox, E. Franco-Macías, M. J. Bullido, A. Frank-García, L. Froelich, B. Fulton-Howard, D. Galimberti, J. M. García-Alberca, P. García-González, S. Garcia-Madrona, G. Garcia-Ribas, R. Ghidoni, I. Giegling, G. Giorgio, A. M. Goate, O. Goldhardt, D. Gomez-Fonseca, A. González-Pérez, C. Graff, G. Grande, E. Green, T. Grimmer, E. Grünblatt, M. Grunin, V. Gudnason, T. Guetta-Baranes, A. Haapasalo, G. Hadjigeorgiou, J. L. Haines, K. L. Hamilton-Nelson, H. Hampel, O. Hanon, J. Hardy, A. M. Hartmann, L. Hausner, J. Harwood, S. Heilmann-Heimbach, S. Helisalmi, M. T. Heneka, I. Hernández, M. J. Herrmann, P. Hoffmann, C. Holmes, H. Holstege, R. H. Vilas, M. Hulsman, J. Humphrey, G. J. Biessels, X. Jian, C. Johansson, G. R. Jun, Y. Kastumata, J. Kauwe, P. G. Kehoe, L. Kilander, A. K. Ståhlbom, M. Kivipelto, A. Koivisto, J. Kornhuber, M. H. Kosmidis, W. A. Kukull, P. P. Kuksa, B. W. Kunkle, A. B. Kuzma, C. Lage, E. J. Laukka, L. Launer, A. Lauria, C.-Y. Lee, J. Lehtisalo, O. Lerch, A. Lleó, W. Longstreth Jr, O. Lopez, A. L. de Munain, S. Love, M. Löwemark, L. Luckcuck, K. L. Lunetta, Y. Ma, J. Macías, C. A. MacLeod, W. Maier, F. Mangialasche, M. Spallazzi, M. Marquié, R. Marshall, E. R. Martin, A. M. Montes, C. M. Rodríguez, C. Masullo, R. Mayeux, S. Mead, P. Mecocci, M. Medina, A. Meggy, S. Mehrabian, S. Mendoza, M. Menéndez-González, P. Mir, S. Moebus, M. Mol, L. Molina-Porcel, L. Montrreal, L. Morelli, F. Moreno, K. Morgan, T. Mosley, M. M. Nöthen, C. Muchnik, S. Mukherjee, B. Nacmias, T. Ngandu, G. Nicolas, B. G. Nordestgaard, R. Olaso, A. Orellana, M. Orsini, G. Ortega, A. Padovani, C. Paolo, G. Papenberg, L. Parnetti, F. Pasquier, P. Pastor, G. Peloso, A. Pérez-Cordón, J. Pérez-Tur, P. Pericard, O. Peters, Y. A. L. Pijnenburg, J. A. Pineda, G. Piñol-Ripoll, C. Pisanu, T. Polak, J. Popp, D. Posthuma, J. Priller, R. Puerta, O. Quenez, I. Quintela, J. Q. Thomassen, A. Rábano, I. Rainero, F. Rajabli, I. Ramakers, L. M. Real, M. J. T. Reinders, C. Reitz, D. Reyes-Dumeyer, P. Ridge, S. Riedel-Heller, P. Riederer, N. Roberto, E. Rodriguez-Rodriguez, A. Rongve, I. R. Allende, M. Rosende-Roca, J. L. Royo, E. Rubino, D. Rujescu, M. E. Sáez, P. Sakka, I. Saltvedt, Á. Sanabria, M. B. Sánchez-Arjona, F. Sanchez-Garcia, P. S. Juan, R. Sánchez-Valle, S. B. Sando, C. Sarnowski, C. L. Satizabal, M. Scamosci, N. Scarmeas, E. Scarpini, P. Scheltens, N. Scherbaum, M. Scherer, M. Schmid, A. Schneider, J. M. Schott, G. Selbæk, D. Seripa, M.

Serrano, J. Sha, A. A. Shadrin, O. Skrobot, S. Slifer, G. J. L. Snijders, H. Soininen, V. Solfrizzi, A. Solomon, Y. Song, S. Sorbi, O. Sotolongo-Grau, G. Spalletta, A. Spottke, A. Squassina, E. Stordal, J. P. Tartan, L. Tárraga, N. Tesí, A. Thalamuthu, T. Thomas, G. Tosto, L. Traykov, L. Tremolizzo, A. Tybjærg-Hansen, A. Uitterlinden, A. Ullgren, I. Ulstein, S. Valero, O. Valladares, C. Van Broeckhoven, J. Vance, B. N. Vardarajan, A. van der Lugt, J. Van Dongen, J. van Rooij, J. van Swieten, R. Vandenberghe, F. Verhey, J.-S. Vidal, J. Vogelgsang, M. Vyhnalek, M. Wagner, D. Wallon, L.-S. Wang, R. Wang, L. Weinhold, J. Wiltfang, G. Windle, B. Woods, M. Yannakoulia, H. Zare, Y. Zhao, X. Zhang, C. Zhu, M. Zulaica, EADB, GR@ACE, DEGESCO, EADI, GERAD, Demgene, FinnGen, ADGC, CHARGE, L. A. Farrer, B. M. Psaty, M. Ghanbari, T. Raj, P. Sachdev, K. Mather, F. Jessen, M. A. Ikram, A. de Mendonça, J. Hort, M. Tsolaki, M. A. Pericak-Vance, P. Amouyel, J. Williams, R. Frikke-Schmidt, J. Clarimon, J.-F. Deleuze, G. Rossi, S. Seshadri, O. A. Andreassen, M. Ingelsson, M. Hiltunen, K. Sleegers, G. D. Schellenberg, C. M. van Duijn, R. Sims, W. M. van der Flier, A. Ruiz, A. Ramirez, J.-C. Lambert, New insights into the genetic etiology of Alzheimer's disease and related dementias. *Nat. Genet.* **54**, 412–436 (2022).

9. S. Steinberg, H. Stefansson, T. Jonsson, H. Johannsdottir, A. Ingason, H. Helgason, P. Sulem, O. T. Magnusson, S. A. Gudjonsson, U. Unnsteinsdottir, A. Kong, S. Helisalmi, H. Soininen, J. J. Lah, DemGene, D. Aarsland, T. Fladby, I. D. Ulstein, S. Djurovic, S. B. Sando, L. R. White, G.-P. Knudsen, L. T. Westlye, G. Selbæk, I. Giegling, H. Hampel, M. Hiltunen, A. I. Levey, O. A. Andreassen, D. Rujescu, P. V. Jonsson, S. Bjornsson, J. Snaedal, K. Stefansson, Loss-of-function variants in ABCA7 confer risk of Alzheimer's disease. *Nat. Genet.* **47**, 445–447 (2015).

10. A. De Roeck, C. Van Broeckhoven, K. Sleegers, The role of ABCA7 in Alzheimer's disease: evidence from genomics, transcriptomics and methylomics. *Acta Neuropathol.* **138**, 201–220 (2019).

11. C. Reitz, G. Jun, A. Naj, R. Rajbhandary, B. N. Vardarajan, L.-S. Wang, O. Valladares, C.-F. Lin, E. B. Larson, N. R. Graff-Radford, D. Evans, P. L. De Jager, P. K. Crane, J. D. Buxbaum, J. R. Murrell, T. Raj, N. Ertekin-Taner, M. Logue, C. T. Baldwin, R. C. Green, L. L. Barnes, L. B. Cantwell, M. D. Fallin, R. C. P. Go, P. Griffith, T. O. Obisesan, J. J. Manly, K. L. Lunetta, M. I. Kamboh, O. L. Lopez, D. A. Bennett, H. Hendrie, K. S. Hall, A. M. Goate, G. S. Byrd, W. A. Kukull, T. M. Foroud, J. L. Haines, L. A. Farrer, M. A. Pericak-Vance, G. D. Schellenberg, R. Mayeux, Alzheimer Disease Genetics Consortium, Variants in the ATP-binding cassette transporter (ABCA7), apolipoprotein E ϵ4,and the risk of late-onset Alzheimer disease in African Americans. *JAMA*. **309**, 1483–1492 (2013).

12. H. Holstege, M. Hulsman, C. Charbonnier, B. Grenier-Boley, O. Quenez, D. Grozeva, J. G. J. van Rooij, R. Sims, S. Ahmad, N. Amin, P. J. Norsworthy, O. Dols-Icardo, H. Hummerich, A. Kawalia, P. Amouyel, G. W. Beecham, C. Berr, J. C. Bis, A. Boland, P. Bossù, F. Bouwman, J. Bras, D. Campion, J. N. Cochran, A. Daniele, J.-F. Dartigues, S. Debette, J.-F. Deleuze, N. Denning, A. L. DeStefano, L. A. Farrer, M. V. Fernández, N. C. Fox, D. Galimberti, E. Genin, J. J. P. Gille, Y. Le Guen, R. Guerreiro, J. L. Haines, C. Holmes, M. A. Ikram, M. K. Ikram, I. E. Jansen, R. Kraaij, M. Lathrop, A. W. Lemstra, A. Lleó, L. Luckcuck, M. M. A. M. Mannens, R. Marshall, E. R. Martin, C. Masullo, R. Mayeux, P. Mecocci, A. Meggy, M. O. Mol, K. Morgan, R. M. Myers, B. Nacmias, A. C.

Naj, V. Napolioni, F. Pasquier, P. Pastor, M. A. Pericak-Vance, R. Raybould, R. Redon, M. J. T. Reinders, A.-C. Richard, S. G. Riedel-Heller, F. Rivadeneira, S. Rousseau, N. S. Ryan, S. Saad, P. Sanchez-Juan, G. D. Schellenberg, P. Scheltens, J. M. Schott, D. Seripa, S. Seshadri, D. Sie, E. A. Sistermans, S. Sorbi, R. van Spaendonk, G. Spalletta, N. Tesi, B. Tijms, A. G. Uitterlinden, S. J. van der Lee, P. J. Visser, M. Wagner, D. Wallon, L.-S. Wang, A. Zarea, J. Clarimon, J. C. van Swieten, M. D. Greicius, J. S. Yokoyama, C. Cruchaga, J. Hardy, A. Ramirez, S. Mead, W. M. van der Flier, C. M. van Duijn, J. Williams, G. Nicolas, C. Bellenguez, J.-C. Lambert, Exome sequencing identifies rare damaging variants in ATP8B4 and ABCA1 as risk factors for Alzheimer's disease. *Nat. Genet.* **54**, 1786–1794 (2022).

13. N. N. Lyssenko, D. Praticò, ABCA7 and the altered lipidostasis hypothesis of Alzheimer's disease. *Alzheimers. Dement.* **17**, 164–174 (2021).

14. K. Le Guennec, G. Nicolas, O. Quenez, C. Charbonnier, D. Wallon, C. Bellenguez, B. Grenier-Boley, S. Rousseau, A.-C. Richard, A. Rovelet-Lecrux, D. Bacq, J.-G. Garnier, R. Olaso, A. Boland, V. Meyer, J.-F. Deleuze, P. Amouyel, H. M. Munter, G. Bourque, M. Lathrop, T. Frebourg, R. Redon, L. Letenneur, J.-F. Dartigues, F. Pasquier, A. Rollin-Sillaire, E. Génin, J.-C. Lambert, D. Hannequin, D. Campion, CNR-MAJ collaborators, ABCA7 rare variants and Alzheimer disease risk. *Neurology*. **86**, 2134–2137 (2016).

15. W. S. Kim, C. S. Weickert, B. Garner, Role of ATP-binding cassette transporters in brain lipid transport and neurological disease. *J. Neurochem.* **104**, 1145–1166 (2008).

16. S. Abe-Dohmae, Y. Ikeda, M. Matsuo, M. Hayashi, K.-I. Okuhira, K. Ueda, S. Yokoyama, Human ABCA7 supports apolipoprotein-mediated release of cellular cholesterol and phospholipid to generate high density lipoprotein. *J. Biol. Chem.* **279**, 604–611 (2004).

17. N. Wang, D. Lan, M. Gerbod-Giannone, P. Linsel-Nitschke, A. W. Jehle, W. Chen, L. O. Martinez, A. R. Tall, ATP-binding cassette transporter A7 (ABCA7) binds apolipoprotein A-I and mediates cellular phospholipid but not cholesterol efflux. *J. Biol. Chem.* **278**, 42906–42912 (2003).

18. T. Aikawa, M.-L. Holm, T. Kanekiyo, ABCA7 and Pathogenic Pathways of Alzheimer's Disease. *Brain Sci*. **8** (2018), doi:10.3390/brainsci8020027.

19. N. Tanaka, S. Abe-Dohmae, N. Iwamoto, S. Yokoyama, Roles of ATP-binding cassette transporter A7 in cholesterol homeostasis and host defense system. *J. Atheroscler. Thromb.* **18**, 274–281 (2011).

20. N. Habib, I. Avraham-Davidi, A. Basu, T. Burks, K. Shekhar, M. Hofree, S. R. Choudhury, F. Aguet, E. Gelfand, K. Ardlie, D. A. Weitz, O. Rozenblatt-Rosen, F. Zhang, A. Regev, Massively parallel single-nucleus RNA-seq with DroNc-seq. *Nat. Methods*. **14**, 955–958 (2017).

21. B. B. Lake, R. Ai, G. E. Kaeser, N. S. Salathia, Y. C. Yung, R. Liu, A. Wildberg, D. Gao, H.-L. Fung, S. Chen, R. Vijayaraghavan, J. Wong, A. Chen, X. Sheng, F. Kaper, R. Shen, M. Ronaghi, J.-B. Fan, W. Wang, J. Chun, K. Zhang, Neuronal subtypes and diversity

revealed by single-nucleus RNA sequencing of the human brain. *Science*. **352**, 1586–1590 (2016).

22. S. Zhong, S. Zhang, X. Fan, Q. Wu, L. Yan, J. Dong, H. Zhang, L. Li, L. Sun, N. Pan, X. Xu, F. Tang, J. Zhang, J. Qiao, X. Wang, A single-cell RNA-seq survey of the developmental landscape of the human prefrontal cortex. *Nature*. **555**, 524–528 (2018).

23. I. Korsunsky, N. Millard, J. Fan, K. Slowikowski, F. Zhang, K. Wei, Y. Baglaenko, M. Brenner, P.-R. Loh, S. Raychaudhuri, Fast, sensitive and accurate integration of single-cell data with Harmony. *Nat. Methods*. **16**, 1289–1296 (2019).

24. L. McInnes, J. Healy, J. Melville, UMAP: Uniform Manifold Approximation and Projection for Dimension Reduction (2018), (available at http://arxiv.org/abs/1802.03426).

25. G. M. Welch, C. A. Boix, E. Schmauch, J. Davila-Velderrain, M. B. Victor, V. Dileep, P. L. Bozzelli, Q. Su, J. D. Cheng, A. Lee, N. S. Leary, A. R. Pfenning, M. Kellis, L.-H. Tsai, Neurons burdened by DNA double-strand breaks incite microglia activation through antiviral-like signaling in neurodegeneration. *Sci Adv*. **8**, eabo4662 (2022).

26. A. Liberzon, C. Birger, H. Thorvaldsdóttir, M. Ghandi, J. P. Mesirov, P. Tamayo, The Molecular Signatures Database (MSigDB) hallmark gene set collection. *Cell Syst*. **1**, 417–425 (2015).

27. S. Mubeen, C. T. Hoyt, A. Gemünd, M. Hofmann-Apitius, H. Fröhlich, D. Domingo-Fernández, The Impact of Pathway Database Choice on Statistical Enrichment Analysis and Predictive Modeling. *Front. Genet.* **10**, 1203 (2019).

28. A. Subramanian, P. Tamayo, V. K. Mootha, S. Mukherjee, B. L. Ebert, M. A. Gillette, A. Paulovich, S. L. Pomeroy, T. R. Golub, E. S. Lander, J. P. Mesirov, Gene set enrichment analysis: a knowledge-based approach for interpreting genome-wide expression profiles. *Proc. Natl. Acad. Sci. U. S. A.* **102**, 15545–15550 (2005).

29. B. W. Kernighan, S. Lin, An efficient heuristic procedure for partitioning graphs. *Bell Syst. Tech. J.* **49**, 291–307 (1970).

30. Specificity of ABCA7-mediated cell lipid efflux. *Biochimica et Biophysica Acta (BBA) - Molecular and Cell Biology of Lipids*. **1867**, 159157 (2022).

31. Lysophosphatidylcholine export by human ABCA7. *Biochimica et Biophysica Acta (BBA) - Molecular and Cell Biology of Lipids*. **1862**, 658–665 (2017).

32. S.-M. Ho, B. J. Hartley, J. Tcw, M. Beaumont, K. Stafford, P. A. Slesinger, K. J. Brennand, Rapid Ngn2-induction of excitatory neurons from hiPSC-derived neural progenitor cells. *Methods*. **101**, 113–124 (2016).

33. R. Tian, A. Abarientos, J. Hong, S. H. Hashemi, R. Yan, N. Dräger, K. Leng, M. A. Nalls, A. B. Singleton, K. Xu, F. Faghri, M. Kampmann, Genome-wide CRISPRi/a screens in human neurons link lysosomal failure to ferroptosis. *Nat. Neurosci.* **24**, 1020–1034 (2021).

34. D. Zadravec, A. Brolinson, R. M. Fisher, C. Carneheim, R. I. Csikasz, J. Bertrand-Michel, J. Borén, H. Guillou, M. Rudling, A. Jacobsson, Ablation of the very-long-chain fatty acid elongase ELOVL3 in mice leads to constrained lipid storage and resistance to diet-induced obesity. *FASEB J.* **24**, 4366–4377 (2010).

35. S. Tripathy, K. A. Lytle, R. D. Stevens, J. R. Bain, C. B. Newgard, A. S. Greenberg, L.-S. Huang, D. B. Jump, Fatty acid elongase-5 (Elovl5) regulates hepatic triglyceride catabolism in obese C57BL/6J mice. *J. Lipid Res.* **55**, 1448–1464 (2014).

36. Oxysterol-Binding Protein: new insights into lipid transport functions and human diseases. *Biochimica et Biophysica Acta (BBA) - Molecular and Cell Biology of Lipids*. **1868**, 159365 (2023).

37. C. Guo, L. Sun, X. Chen, D. Zhang, Oxidative stress, mitochondrial damage and neurodegenerative diseases. *Neural Regeneration Res.* **8**, 2003–2014 (2013).

38. N. Nissanka, C. T. Moraes, Mitochondrial DNA damage and reactive oxygen species in neurodegenerative disease. *FEBS Lett.* **592**, 728–742 (2018).

39. B. Zhang, C. Pan, C. Feng, C. Yan, Y. Yu, Z. Chen, C. Guo, X. Wang, Role of mitochondrial reactive oxygen species in homeostasis regulation. *Redox Rep.* (2022), doi:10.1080/13510002.2022.2046423.

40. M. P. Mori, N. C. de Souza-Pinto, Role of mitochondrial dysfunction in the pathophysiology of DNA repair disorders. *Cell Biol. Int.* **42**, 643–650 (2018).

41. Molecular pathophysiology of impaired glucose metabolism, mitochondrial dysfunction, and oxidative DNA damage in Alzheimer's disease brain. *Mech. Ageing Dev.* **161**, 95–104 (2017).

42. G. Welch, L.-H. Tsai, Mechanisms of DNA damage-mediated neurotoxicity in neurodegenerative disease. *EMBO Rep.* **23**, e54217 (2022).

43. Cell Cycle Activation Linked to Neuronal Cell Death Initiated by DNA Damage. *Neuron*. **41**, 549–561 (2004).

44. Recent developments in the role of DNA damage response and understanding its implications for new therapeutic approaches in Alzheimer's disease. *Translational Medicine of Aging*. **7**, 52–65 (2023).

45. A. R. Collins, The Comet Assay for DNA Damage and Repair: Principles, Applications, and Limitations. *Molecular Biotechnology*. **26** (2004), pp. 249–261.

46. P. L. Olive, D. Wlodek, J. P. Banáth, DNA double-strand breaks measured in individual cells subjected to gel electrophoresis. *Cancer Res.* **51**, 4671–4676 (1991).

47. P.-C. Pao, J. Penney, L.-H. Tsai, Examining the Role of HDACs in DNA Double-Strand Break Repair in Neurons. *Methods Mol. Biol.* **1983**, 225–234 (2019).

48. D. Iacobazzi, P. Convertini, S. Todisco, A. Santarsiero, V. Iacobazzi, V. Infantino, New Insights into NF-κB Signaling in Innate Immunity: Focus on Immunometabolic Crosstalks. *Biology* . **12**, 776 (2023).

49. M. Mussbacher, M. Derler, J. Basílio, J. A. Schmid, NF-κB in monocytes and macrophages – an inflammatory master regulator in multitalented immune cells. *Front. Immunol.* **14**, 1134661 (2023).

50. K. Satoh, S. Abe-Dohmae, S. Yokoyama, P. St George-Hyslop, P. E. Fraser, ATP-binding cassette transporter A7 (ABCA7) loss of function alters Alzheimer amyloid processing. *J. Biol. Chem.* **290**, 24152–24165 (2015).

51. W. S. Kim, G. J. Guillemin, E. N. Glaros, C. K. Lim, B. Garner, Quantitation of ATP-binding cassette subfamily-A transporter gene expression in primary human brain cells. *Neuroreport*. **17**, 891–896 (2006).

52. A. K. Walker, R. L. Jacobs, J. L. Watts, V. Rottiers, K. Jiang, D. M. Finnegan, T. Shioda, M. Hansen, F. Yang, L. J. Niebergall, D. E. Vance, M. Tzoneva, A. C. Hart, A. M. Näär, A conserved SREBP-1/phosphatidylcholine feedback circuit regulates lipogenesis in metazoans. *Cell*. **147**, 840–852 (2011).

53. G. Sienski, P. Narayan, J. M. Bonner, N. Kory, S. Boland, A. A. Arczewska, W. T. Ralvenius, L. Akay, E. Lockshin, L. He, B. Milo, A. Graziosi, V. Baru, C. A. Lewis, M. Kellis, D. M. Sabatini, L.-H. Tsai, S. Lindquist, disrupts intracellular lipid homeostasis in human iPSC-derived glia. *Sci. Transl. Med.* **13** (2021), doi:10.1126/scitranslmed.aaz4564.

54. R. M. Hagen, S. Rodriguez-Cuenca, A. Vidal-Puig, An allostatic control of membrane lipid composition by SREBP1. *FEBS Lett.* **584**, 2689–2698 (2010).

55. S. Rajakumari, R. Rajasekharan, G. Daum, Triacylglycerol lipolysis is linked to sphingolipid and phospholipid metabolism of the yeast Saccharomyces cerevisiae. *Biochim. Biophys. Acta*. **1801**, 1314–1322 (2010).

56. C. Yang, X. Wang, J. Wang, X. Wang, W. Chen, N. Lu, S. Siniossoglou, Z. Yao, K. Liu, Rewiring Neuronal Glycerolipid Metabolism Determines the Extent of Axon Regeneration. *Neuron*. **105**, 276–292.e5 (2020).

57. J. M. Inloes, K.-L. Hsu, M. M. Dix, A. Viader, K. Masuda, T. Takei, M. R. Wood, B. F. Cravatt, The hereditary spastic paraplegia-related enzyme DDHD2 is a principal brain triglyceride lipase. *Proc. Natl. Acad. Sci. U. S. A.* **111**, 14924–14929 (2014).

58. I. Ralhan, C.-L. Chang, J. Lippincott-Schwartz, M. S. Ioannou, Lipid droplets in the nervous system. *J. Cell Biol.* **220** (2021), doi:10.1083/jcb.202102136.

59. L. W. Wat, C. Chao, R. Bartlett, J. L. Buchanan, J. W. Millington, H. J. Chih, Z. S. Chowdhury, P. Biswas, V. Huang, L. J. Shin, L. C. Wang, M.-P. L. Gauthier, M. C. Barone, K. L. Montooth, M. A. Welte, E. J. Rideout, A role for triglyceride lipase brummer in the regulation of sex differences in Drosophila fat storage and breakdown. *PLoS Biol.* **18**, e3000595 (2020).

60. P. Schönfeld, G. Reiser, Why does brain metabolism not favor burning of fatty acids to provide energy? Reflections on disadvantages of the use of free fatty acids as fuel for brain. *J. Cereb. Blood Flow Metab.* **33**, 1493–1499 (2013).

61. P. Schönfeld, G. Reiser, Brain energy metabolism spurns fatty acids as fuel due to their inherent mitotoxicity and potential capacity to unleash neurodegeneration. *Neurochem. Int.* **109**, 68–77 (2017).

62. M. A. Aon, N. Bhatt, S. C. Cortassa, Mitochondrial and cellular mechanisms for managing lipid excess. *Front. Physiol.* **5**, 282 (2014).

63. G. Robert, J. Richard Wagner, ROS-Induced DNA Damage as an Underlying Cause of Aging. *Advances in Geriatric Medicine and Research*. **4** (2020), doi:10.20900/agmr20200024.

64. C. Volanti, J.-Y. Matroule, J. Piette, Involvement of oxidative stress in NF-kappaB activation in endothelial cells treated by photodynamic therapy. *Photochem. Photobiol.* **75**, 36–45 (2002).

65. T. G. Canty Jr, E. M. Boyle Jr, A. Farr, E. N. Morgan, E. D. Verrier, T. H. Pohlman, Oxidative stress induces NF-kappaB nuclear translocation without degradation of IkappaBalpha. *Circulation*. **100**, II361–4 (1999).

66. R. Schreck, K. Albermann, P. A. Baeuerle, Nuclear factor kappa B: an oxidative stress-responsive transcription factor of eukaryotic cells (a review). *Free Radic. Res. Commun.* **17**, 221–237 (1992).

67. J. N. van der Veen, J. P. Kennelly, S. Wan, J. E. Vance, D. E. Vance, R. L. Jacobs, The critical role of phosphatidylcholine and phosphatidylethanolamine metabolism in health and disease. *Biochim. Biophys. Acta Biomembr.* **1859**, 1558–1572 (2017).

68. Phosphatidylcholine Biosynthesis during Neuronal Differentiation and Its Role in Cell Fate Determination. *J. Biol. Chem.* **285**, 25382–25393 (2010).

69. L. Paoletti, C. Elena, P. Domizi, C. Banchio, Role of Phosphatidylcholine during Neuronal differentiation. *IUBMB Life*. **63**, 714–720 (2011).

70. E. Posse de Chaves, D. E. Vance, R. B. Campenot, J. E. Vance, Axonal synthesis of phosphatidylcholine is required for normal axonal growth in rat sympathetic neurons. *J. Cell Biol.* **128**, 913–918 (1995).

71. W. Araki, R. J. Wurtman, Control of membrane phosphatidylcholine biosynthesis by diacylglycerol levels in neuronal cells undergoing neurite outgrowth. *Proc. Natl. Acad. Sci. U. S. A.* **94**, 11946–11950 (1997).

72. D. Magaquian, S. Delgado Ocaña, C. Perez, C. Banchio, Phosphatidylcholine restores neuronal plasticity of neural stem cells under inflammatory stress. *Sci. Rep.* **11**, 1–12 (2021).

73. Increasing levels of cardiolipin differentially influence packing of phospholipids found in the mitochondrial inner membrane. *Biochem. Biophys. Res. Commun.* **450**, 366–371 (2014).

74. T. H. Haines, N. A. Dencher, Cardiolipin: a proton trap for oxidative phosphorylation. *FEBS Lett.* **528**, 35–39 (2002).

75. M. Fry, D. E. Green, Cardiolipin requirement by cytochrome oxidase and the catalytic role of phospholipid. *Biochem. Biophys. Res. Commun.* **93**, 1238–1246 (1980).

76. M. Fry, D. E. Green, Cardiolipin requirement for electron transfer in complex I and III of the mitochondrial respiratory chain. *J. Biol. Chem.* **256**, 1874–1880 (1981).

77. M. McKenzie, M. Lazarou, D. R. Thorburn, M. T. Ryan, Mitochondrial respiratory chain supercomplexes are destabilized in Barth Syndrome patients. *J. Mol. Biol.* **361**, 462–469 (2006).

78. K. Shinzawa-Itoh, H. Aoyama, K. Muramoto, H. Terada, T. Kurauchi, Y. Tadehara, A. Yamasaki, T. Sugimura, S. Kurono, K. Tsujimoto, T. Mizushima, E. Yamashita, T. Tsukihara, S. Yoshikawa, Structures and physiological roles of 13 integral lipids of bovine heart cytochrome c oxidase. *EMBO J.* **26**, 1713–1725 (2007).

79. M. Zhang, E. Mileykovskaya, W. Dowhan, Gluing the respiratory chain together. Cardiolipin is required for supercomplex formation in the inner mitochondrial membrane. *J. Biol. Chem.* **277**, 43553–43556 (2002).

80. Cardiolipin Stabilizes Respiratory Chain Supercomplexes. *J. Biol. Chem.* **278**, 52873–52880 (2003).

81. C. T. Chu, J. Ji, R. K. Dagda, J. F. Jiang, Y. Y. Tyurina, A. A. Kapralov, V. A. Tyurin, N. Yanamala, I. H. Shrivastava, D. Mohammadyani, K. Z. Qiang Wang, J. Zhu, J. Klein-Seetharaman, K. Balasubramanian, A. A. Amoscato, G. Borisenko, Z. Huang, A. M. Gusdon, A. Cheikhi, E. K. Steer, R. Wang, C. Baty, S. Watkins, I. Bahar, H. Bayır, V. E. Kagan, Cardiolipin externalization to the outer mitochondrial membrane acts as an elimination signal for mitophagy in neuronal cells. *Nat. Cell Biol.* **15**, 1197–1205 (2013).

82. M. K. Crowder, C. D. Seacrist, R. D. Blind, Phospholipid regulation of the nuclear receptor superfamily. *Adv. Biol. Regul.* **63**, 6–14 (2017).

83. A. Alzheimer, Uber eigenartige Erkrankung der Hirnrinde. *All Z Psychiatr*. **64**, 146–148 (1907).

84. Aberrant Lipid Metabolism in the Forebrain Niche Suppresses Adult Neural Stem Cell Proliferation in an Animal Model of Alzheimer's Disease. *Cell Stem Cell*. **17**, 397–411 (2015).

85. J. W. Pettegrew, K. Panchalingam, R. L. Hamilton, R. J. McClure, Brain membrane phospholipid alterations in Alzheimer's disease. *Neurochem. Res.* **26**, 771–782 (2001).

86. B. M. Ross, A. Moszczynska, J. Erlich, S. J. Kish, Phospholipid-metabolizing enzymes in

Alzheimer's disease: increased lysophospholipid acyltransferase activity and decreased phospholipase A2 activity. *J. Neurochem.* **70**, 786–793 (1998).

87. X. Han, D. M. Holtzman, D. W. McKeel Jr, Plasmalogen deficiency in early Alzheimer's disease subjects and in animal models: molecular characterization using electrospray ionization mass spectrometry. *J. Neurochem.* **77**, 1168–1180 (2001).

88. L. Ginsberg, J. H. Xuereb, N. L. Gershfeld, Membrane instability, plasmalogen content, and Alzheimer's disease. *J. Neurochem.* **70**, 2533–2538 (1998).

89. J. K. Blusztajn, I. Lopez Gonzalez-Coviella, M. Logue, J. H. Growdon, R. J. Wurtman, Levels of phospholipid catabolic intermediates, glycerophosphocholine and glycerophosphoethanolamine, are elevated in brains of Alzheimer's disease but not of Down's syndrome patients. *Brain Res.* **536**, 240–244 (1990).

90. J. A. Conquer, M. C. Tierney, J. Zecevic, W. J. Bettger, R. H. Fisher, Fatty acid analysis of blood plasma of patients with Alzheimer's disease, other types of dementia, and cognitive impairment. *Lipids*. **35**, 1305–1312 (2000).

91. C. Picard, C. Julien, J. Frappier, J. Miron, L. Théroux, D. Dea, United Kingdom Brain Expression Consortium and for the Alzheimer's Disease Neuroimaging Initiative, J. C. S. Breitner, J. Poirier, Alterations in cholesterol metabolism-related genes in sporadic Alzheimer's disease. *Neurobiol. Aging*. **66**, 180.e1–180.e9 (2018).

92. Y. Wang, M. Cella, K. Mallinson, J. D. Ulrich, K. L. Young, M. L. Robinette, S. Gilfillan, G. M. Krishnan, S. Sudhakar, B. H. Zinselmeyer, D. M. Holtzman, J. R. Cirrito, M. Colonna, TREM2 lipid sensing sustains the microglial response in an Alzheimer's disease model. *Cell*. **160**, 1061–1071 (2015).

93. R.-Y. Li, Q. Qin, H.-C. Yang, Y.-Y. Wang, Y.-X. Mi, Y.-S. Yin, M. Wang, C.-J. Yu, Y. Tang, TREM2 in the pathogenesis of AD: a lipid metabolism regulator and potential metabolic therapeutic target. *Mol. Neurodegener.* **17**, 40 (2022).

94. F. Filipello, S.-F. You, F. S. Mirfakhar, S. Mahali, B. Bollman, M. Acquarone, O. Korvatska, J. A. Marsh, A. Sivaraman, R. Martinez, C. Cantoni, L. De Feo, L. Ghezzi, M. A. Minaya, A. Renganathan, A. G. Cashikar, J.-I. Satoh, W. Beatty, A. K. Iyer, M. Cella, W. H. Raskind, L. Piccio, C. M. Karch, Defects in lysosomal function and lipid metabolism in human microglia harboring a TREM2 loss of function mutation. *Acta Neuropathol.* **145**, 749–772 (2023).

95. F. Yin, Lipid metabolism and Alzheimer's disease: clinical evidence, mechanistic link and therapeutic promise. *FEBS J.* **290**, 1420–1453 (2023).

96. J. L. Mercer, J. P. Argus, D. M. Crabtree, M. M. Keenan, M. Q. Wilks, J.-T. A. Chi, S. J. Bensinger, C. P. Lavau, D. S. Wechsler, Modulation of PICALM Levels Perturbs Cellular Cholesterol Homeostasis. *PLoS One*. **10**, e0129776 (2015).

97. L. A. Solomon, S. Podder, J. He, N. L. Jackson-Chornenki, K. Gibson, R. G. Ziliotto, J. Rhee, R. P. DeKoter, Coordination of Myeloid Differentiation with Reduced Cell Cycle

Progression by PU.1 Induction of MicroRNAs Targeting Cell Cycle Regulators and Lipid Anabolism. *Mol. Cell. Biol.* **37** (2017), doi:10.1128/MCB.00013-17.

98. W. J. Strittmatter, A. D. Roses, Apolipoprotein E and Alzheimer's disease. *Annu. Rev. Neurosci.* **19**, 53–77 (1996).

99. Y.-T. Lin, J. Seo, F. Gao, H. M. Feldman, H.-L. Wen, J. Penney, H. P. Cam, E. Gjoneska, W. K. Raja, J. Cheng, R. Rueda, O. Kritskiy, F. Abdurrob, Z. Peng, B. Milo, C. J. Yu, S. Elmsaouri, D. Dey, T. Ko, B. A. Yankner, L.-H. Tsai, APOE4 Causes Widespread Molecular and Cellular Alterations Associated with Alzheimer's Disease Phenotypes in Human iPSC-Derived Brain Cell Types. *Neuron*. **98**, 1294 (2018).

100. J. W. Blanchard, M. Bula, J. Davila-Velderrain, L. A. Akay, L. Zhu, A. Frank, M. B. Victor, J. M. Bonner, H. Mathys, Y.-T. Lin, T. Ko, D. A. Bennett, H. P. Cam, M. Kellis, L.-H. Tsai, Reconstruction of the human blood-brain barrier in vitro reveals a pathogenic mechanism of APOE4 in pericytes. *Nat. Med.* **26**, 952–963 (2020).

101. J. W. Blanchard, L. A. Akay, J. Davila-Velderrain, D. von Maydell, H. Mathys, S. M. Davidson, A. Effenberger, C.-Y. Chen, K. Maner-Smith, I. Hajjar, E. A. Ortlund, M. Bula, E. Agbas, A. Ng, X. Jiang, M. Kahn, C. Blanco-Duque, N. Lavoie, L. Liu, R. Reyes, Y.-T. Lin, T. Ko, L. R'Bibo, W. T. Ralvenius, D. A. Bennett, H. P. Cam, M. Kellis, L.-H. Tsai, APOE4 impairs myelination via cholesterol dysregulation in oligodendrocytes. *Nature*. **611**, 769–779 (2022).

102. C. Sassi, M. A. Nalls, P. G. Ridge, J. R. Gibbs, J. Ding, M. K. Lupton, C. Troakes, K. Lunnon, S. Al-Sarraj, K. S. Brown, C. Medway, N. Clement, J. Lord, J. Turton, J. Bras, M. R. Almeida, ARUK Consortium, H. Holstege, E. Louwersheimer, W. M. van der Flier, P. Scheltens, J. C. Van Swieten, I. Santana, C. Oliveira, K. Morgan, J. F. Powell, J. S. Kauwe, C. Cruchaga, A. M. Goate, A. B. Singleton, R. Guerreiro, J. Hardy, ABCA7 p.G215S as potential protective factor for Alzheimer's disease. *Neurobiol. Aging*. **46**, 235.e1–9 (2016).

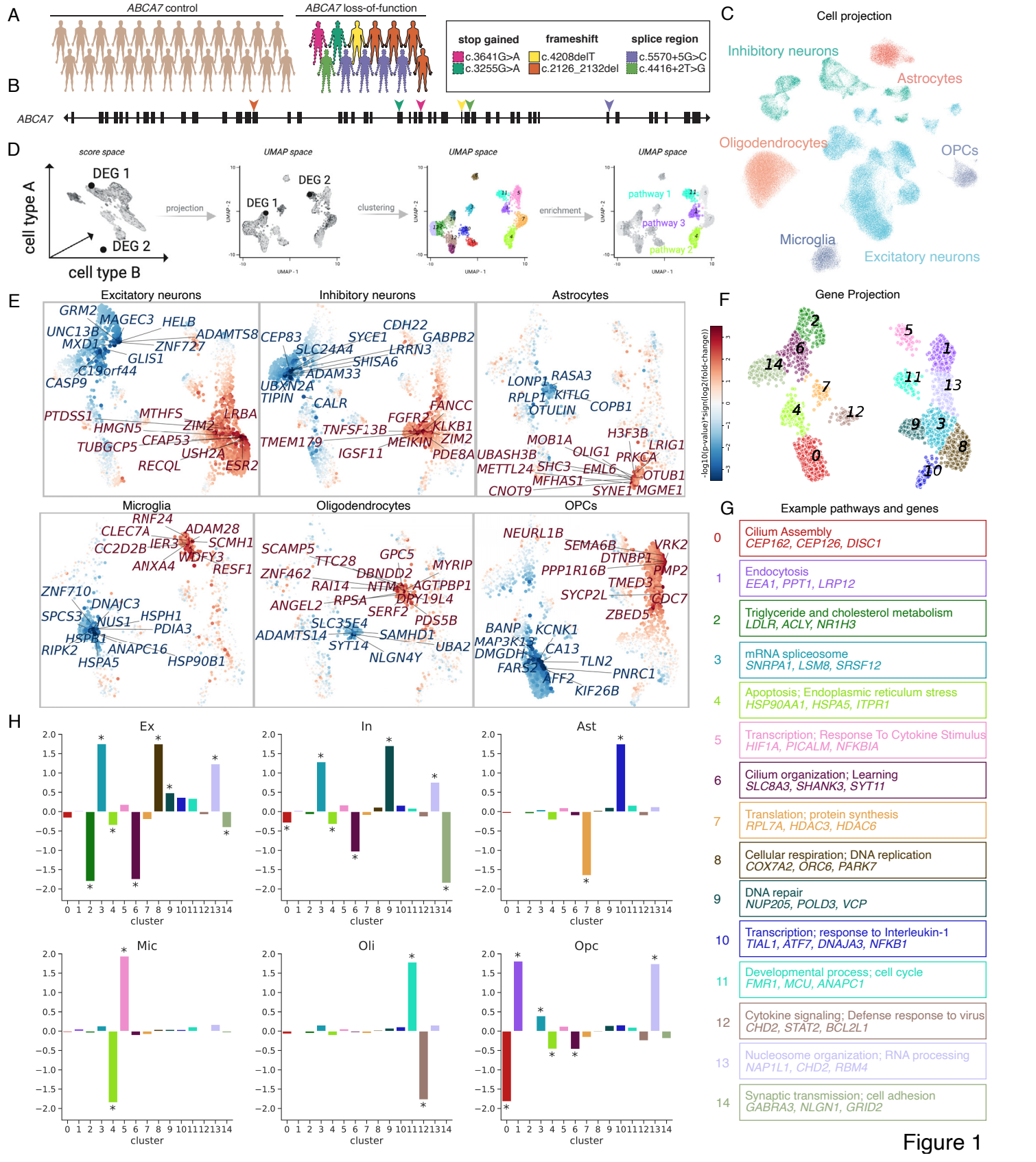
A
ABCA7 control
ABCA7 loss-of-function
stop gained
c.3641G>A
c.3255G>A
frameshift
c.4208delT
c.2126_2132del
splice region
c.5570+5G>C
c.4416+2T>G
B
ABCA7
C
Cell projection
Inhibitory neurons
Astrocytes
Oligodendrocytes
OPCs
Microglia
Excitatory neurons
D
score space
UMAP space
DEG 1
DEG 2
cell type A
cell type B
projection
clustering
enrichment
pathway 1
pathway 2
pathway 3
UMAP - 1
UMAP - 2
E
Excitatory neurons
Inhibitory neurons
Astrocytes
Microglia
Oligodendrocytes
OPCs
F
Gene Projection
-log10(p-value)*sign(log2(fold-change))
G
Example pathways and genes
0 Cilium Assembly
CEP162, CEP126, DISC1
1 Endocytosis
EEA1, PPT1, LRP12
2 Triglyceride and cholesterol metabolism
LDLR, ACLY, NR1H3
3 mRNA spliceosome
SNRPA1, LSM8, SRSF12
4 Apoptosis; Endoplasmic reticulum stress
HSP90AA1, HSPA5, ITPR1
5 Transcription; Response To Cytokine Stimulus
HIF1A, PICALM, NFKBIA
6 Cilium organization; Learning
SLC8A3, SHANK3, SYT11
7 Translation; protein synthesis
RPL7A, HDAC3, HDAC6
8 Cellular respiration; DNA replication
COX7A2, ORC6, PARK7
9 DNA repair
NUP205, POLD3, VCP
10 Transcription; response to Interleukin-1
TIAL1, ATF7, DNAJA3, NFKB1
11 Developmental process; cell cycle
FMR1, MCU, ANAPC1
12 Cytokine signaling; Defense response to virus
CHD2, STAT2, BCL2L1
13 Nucleosome organization; RNA processing
NAP1L1, CHD2, RBM4
14 Synaptic transmission; cell adhesion
GABRA3, NLGN1, GRID2
H
Ex
In
Ast
Mic
Oli
Opc
cluster

Figure 1

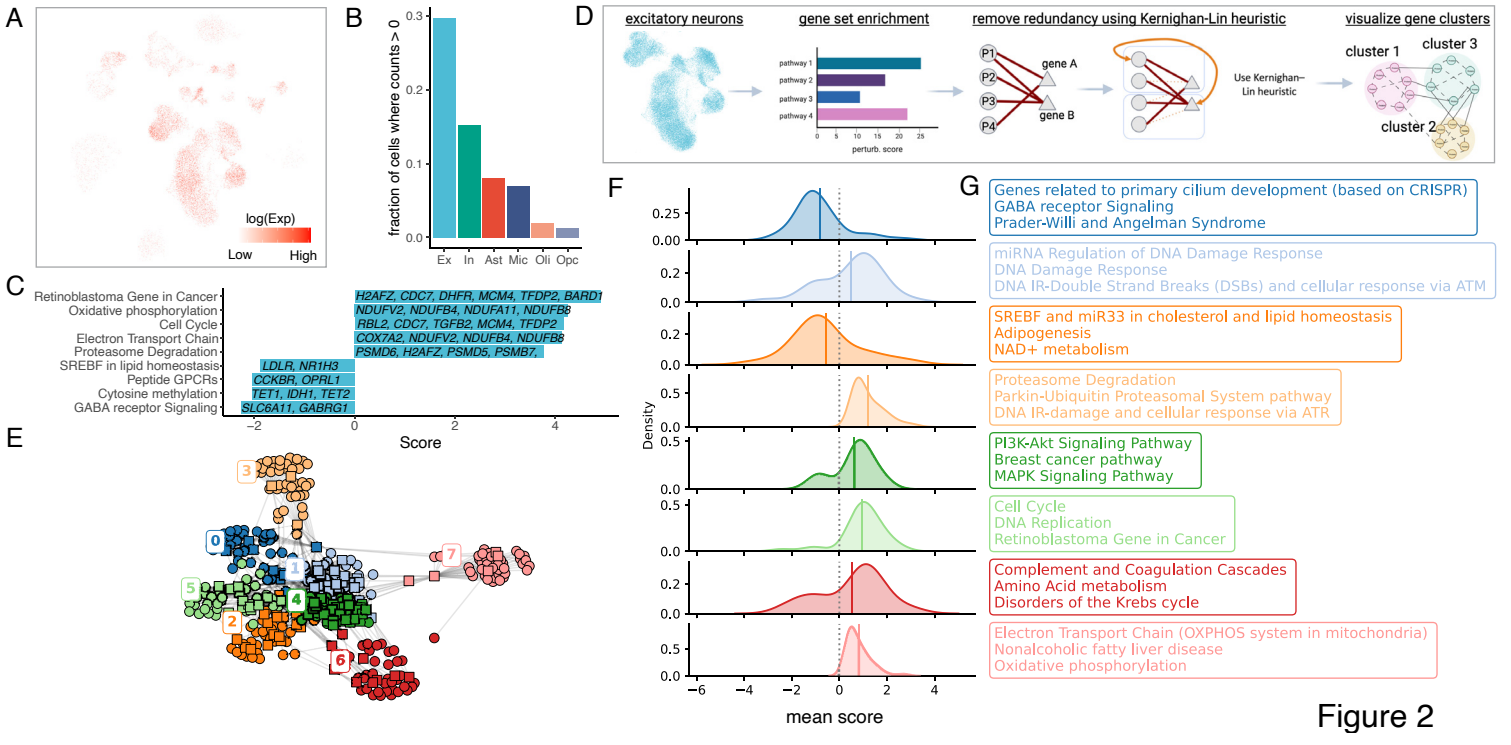
A
log(Exp)
Low
High
B
fraction of cells where counts > 0
0.3
0.2
0.1
0.0
Ex
In
Ast
Mic
Oli
Opc
C
Retinoblastoma Gene in Cancer
Oxidative phosphorylation
Cell Cycle
Electron Transport Chain
Proteasome Degradation
SREBF in lipid homeostasis
Peptide GPCRs
Cytosine methylation
GABA receptor Signaling
H2AFZ, CDC7, DHFR, MCM4, TFDP2, BARD1
NDUFV2, NDUFB4, NDUFA11, NDUFB8
RBL2, CDC7, TGFB2, MCM4, TFDP2
COX7A2, NDUFV2, NDUFB4, NDUFB8
PSMD6, H2AFZ, PSMD5, PSMB7,
LDLR, NR1H3
CCKBR, OPRL1
TET1, IDH1, TET2
SLC6A11, GABRG1
−2
0
2
4
Score
D
excitatory neurons
gene set enrichment
remove redundancy using Kernighan-Lin heuristic
visualize gene clusters
pathway 1
pathway 2
pathway 3
pathway 4
0
5
10
15
20
25
perturb. score
P1
P2
P3
P4
gene A
gene B
Use Kernighan–Lin heuristic
cluster 1
cluster 2
cluster 3
E
0
1
2
3
4
5
6
7
F
Density
0.25
0.00
0.2
0.0
0.5
−6
−4
−2
0
2
4
mean score
G
Genes related to primary cilium development (based on CRISPR)
GABA receptor Signaling
Prader-Willi and Angelman Syndrome
miRNA Regulation of DNA Damage Response
DNA Damage Response
DNA IR-Double Strand Breaks (DSBs) and cellular response via ATM
SREBF and miR33 in cholesterol and lipid homeostasis
Adipogenesis
NAD+ metabolism
Proteasome Degradation
Parkin-Ubiquitin Proteasomal System pathway
DNA IR-damage and cellular response via ATR
PI3K-Akt Signaling Pathway
Breast cancer pathway
MAPK Signaling Pathway
Cell Cycle
DNA Replication
Retinoblastoma Gene in Cancer
Complement and Coagulation Cascades
Amino Acid metabolism
Disorders of the Krebs cycle
Electron Transport Chain (OXPHOS system in mitochondria)
Nonalcoholic fatty liver disease
Oxidative phosphorylation

Figure 2

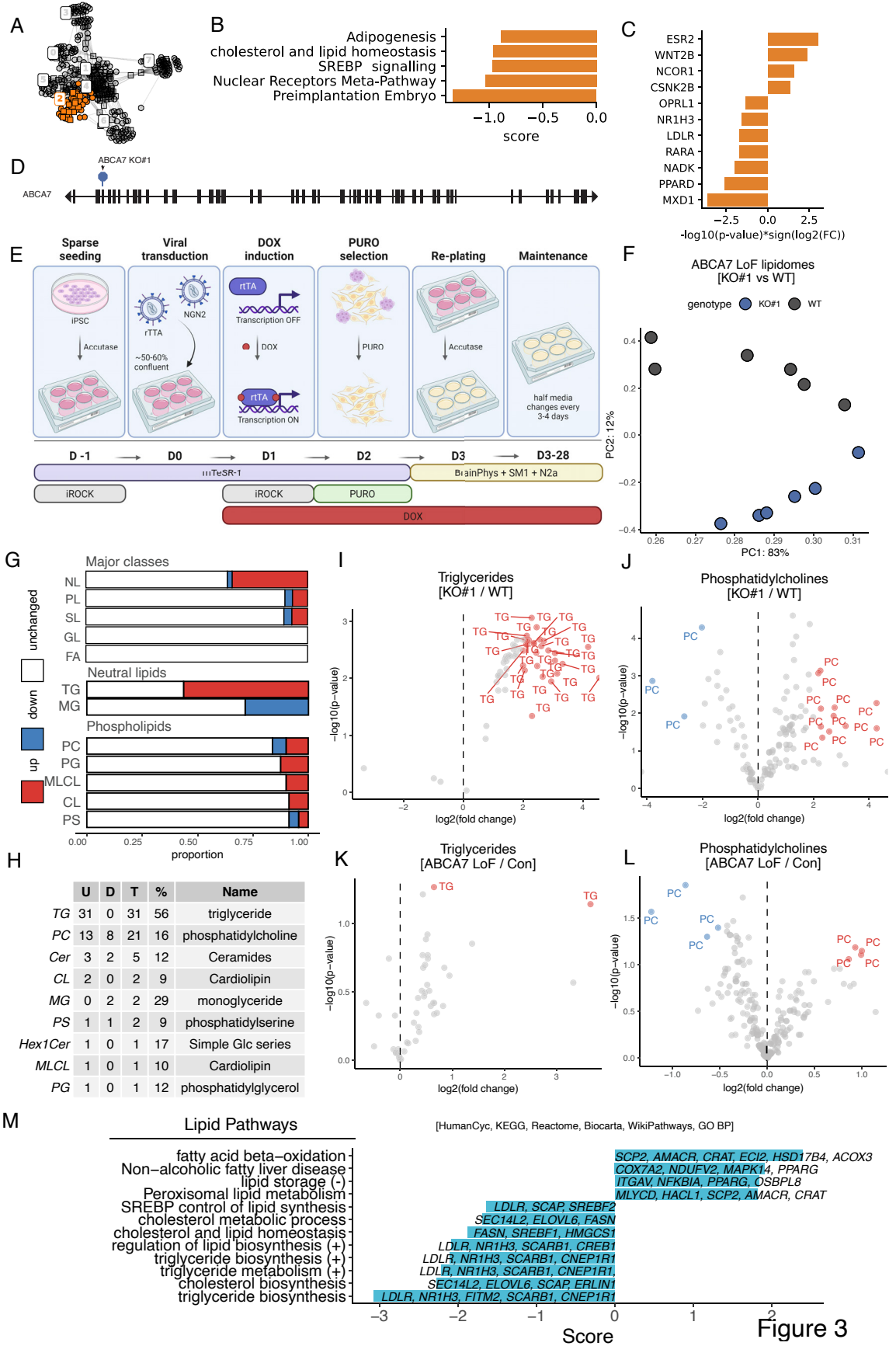

	U	D	T	%	Name
TG	31	0	31	56	triglyceride
PC	13	8	21	16	phosphatidylcholine
Cer	3	2	5	12	Ceramides
CL	2	0	2	9	Cardiolipin
MG	0	2	2	29	monoglyceride
PS	1	1	2	9	phosphatidylserine
Hex1Cer	1	0	1	17	Simple Glc series
MLCL	1	0	1	10	Cardiolipin
PG	1	0	1	12	phosphatidylglycerol

Figure 3

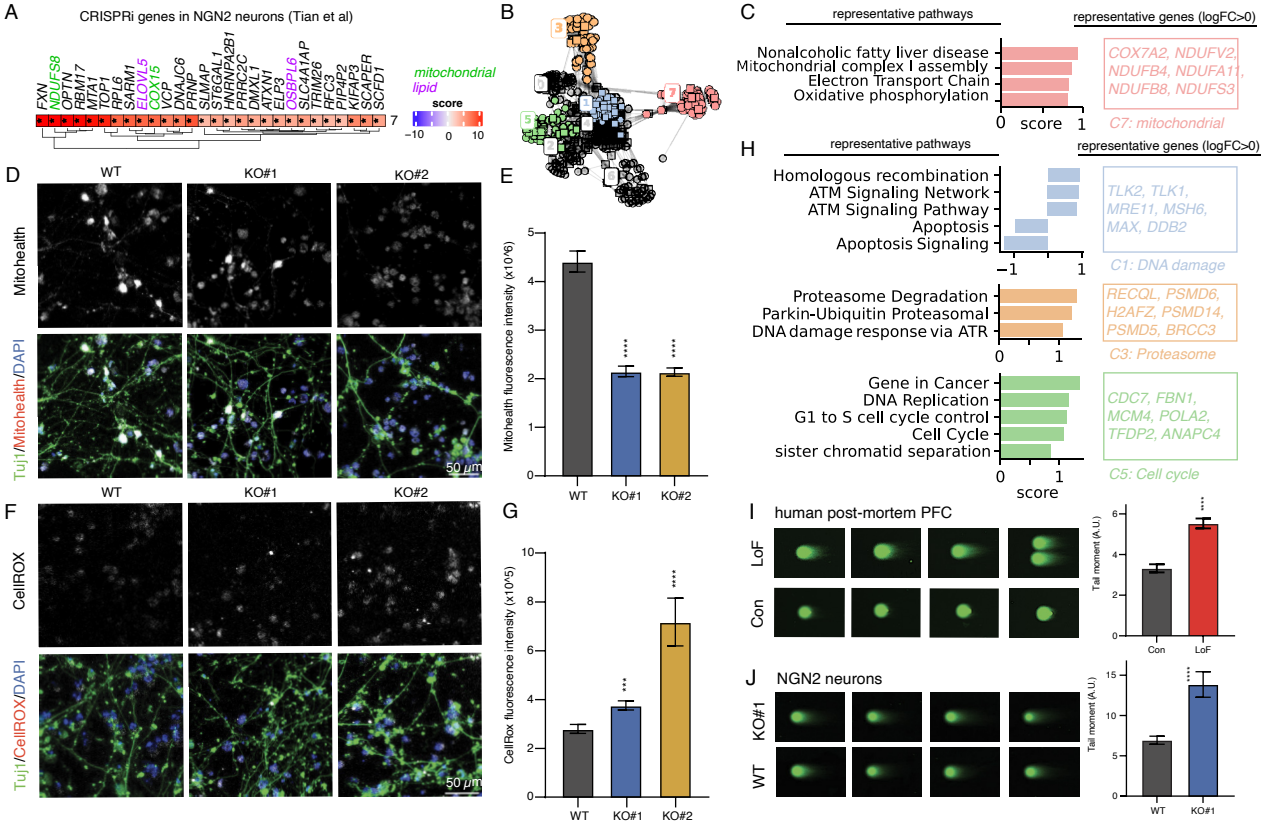
A
CRISPRi genes in NGN2 neurons (Tian et al)
FXN
NDUFS8
OPTN
RBM17
MTA1
TOP1
RPL6
SARM1
ELOVL5
COX15
VCP
DNAJC6
PRNP
SLMAP
ST6GAL1
HNRNPA2B1
PRRC2C
DMXL1
ATXN1
ELP3
OSBPL6
SLC4A1AP
TRIM26
RFC3
PIP4P2
KIFAP3
SCAPER
SCFD1
7
mitochondrial
lipid
score
−10
0
10
B
C
representative pathways
representative genes (logFC>0)
Nonalcoholic fatty liver disease
Mitochondrial complex I assembly
Electron Transport Chain
Oxidative phosphorylation
0
score
1
COX7A2, NDUFV2, NDUFB4, NDUFA11, NDUFB8, NDUFS3
C7: mitochondrial
D
WT
KO#1
KO#2
Mitohealth
Tuj1/Mitohealth/DAPI
50 μm
E
Mitohealth fluorescence intensity (x10^6)
WT
KO#1
KO#2
F
CellROX
Tuj1/CellROX/DAPI
50 μm
G
CellRox fluorescence intensity (x10^5)
WT
KO#1
KO#2
H
representative pathways
representative genes (logFC>0)
Homologous recombination
ATM Signaling Network
ATM Signaling Pathway
Apoptosis
Apoptosis Signaling
−1
1
TLK2, TLK1, MRE11, MSH6, MAX, DDB2
C1: DNA damage
Proteasome Degradation
Parkin-Ubiquitin Proteasomal
DNA damage response via ATR
0
1
RECQL, PSMD6, H2AFZ, PSMD14, PSMD5, BRCC3
C3: Proteasome
Gene in Cancer
DNA Replication
G1 to S cell cycle control
Cell Cycle
sister chromatid separation
0
1
score
CDC7, FBN1, MCM4, POLA2, TFDP2, ANAPC4
C5: Cell cycle
I
human post-mortem PFC
LoF
Con
Tail moment (A.U.)
Con
LoF
J
NGN2 neurons
KO#1
WT
Tail moment (A.U.)
WT
KO#1

Figure 4

Supplementary Materials for

A single-cell atlas of ABCA7 loss-of-function reveals lipid disruptions, mitochondrial dysfunction and DNA damage in neurons

Djuna von Maydell[1,2,†], Shannon Wright[1,2,†], Julia Maeve Bonner[1,2,†], Ping-Chieh Pao[1,2], Gloria Suella Menchaca[1,2], Gwyneth Welch[1,2], Carles A. Boix[3,4], Hansruedi Mathys[1,2,‡], Guillaume Leclerc[3], Noelle Leary[1,2], George Samaan[1,2], Manolis Kellis[3,4], Li-Huei Tsai[1,2,*]

Corresponding author: lhtsai@mit.edu

The PDF file includes:

Materials and Methods
Supplementary Text
Figs. S1 to S11
Tables S1 to S4
References

Other Supplementary Materials for this manuscript include the following:

Data S1 to S12

Materials and Methods

Computational Methods

Variant calling and ROSMAP subject selection

A total of 36 individuals were selected from the ROSMAP cohort, a longitudinal cohort study of aging and dementia in elderly nuns, priests, and brothers. Processed whole genome sequencing variant call files for all ROSMAP samples, where available (N=1249 sequencing samples), were downloaded from Synapse (syn11724057) using a custom pipeline available here (https://github.com/djunamay/ROSMAPwgs/). Variant call data were downloaded for chromosomes harboring *SORL1, TREM2, ABCA7, ATP8B4, ABCA1,* and *ADAM10*. When >1 WGS sample existed for a given subject, the sample with the higher Genomic Quality Score was chosen. Only samples that did not have sex mismatches and were consistent with previous array-based genotype data were considered (see syn12178037). Only variants that passed quality control ['FILTER_PASS'] were considered. Potential LoF variants in each of the aforementioned genes were flagged based on the following criteria: The variant had to be either a splice, missense, frameshift, nonsense, or premature start variant and be annotated as ['LOF']. For ABCA7, this filtering captured known ABCA7 LoF risk variants from the literature, except for c.5570+5G>C (*1*), which was manually added to the filtered variants. Also see syn10901595 (https://www.synapse.org/#!Synapse:syn10901595) for information on WGS library preparation, quality control, variant annotations, and impact predictions. Annotated genotype data for filtered variants is shown in **Data S1**.

The WGS data was used to identify 12 subjects, who did not carry a known LoF variant in one of the aforementioned genes, other than ABCA7 LoF, and for whom fresh-frozen *post-mortem* tissue was available for request from Rush University. We also selected 24 individuals, who do not carry a single ABCA7 LoF mutation or LoF variants in one of the aforementioned genes (termed 'control' samples). Control samples were matched on age, sex, and pathology. Informed consent was obtained from each subject, and the Religious Orders Study and Rush Memory and Aging Project were approved by an Institutional Review Board (IRB) of Rush University Medical Center.

Read Counting & Alignment

Library demultiplexing was performed using the BMC/BCC 1.8 pipeline updated on 12/09/2020 (https://openwetware.org/wiki/BioMicroCenter:Software). Fast-q reads were aligned to human genome GRCh38 and counted using the cellranger *count()* function from cellranger version 6.1.2. (10x Genomics). Introns were included in counting, to allow for detection of unspliced transcripts and the expected number of cells was set to 5000. Otherwise cellranger (v.6.1.2) default parameters were used. Counts across individual samples were then aggregated using a custom aggregation script (https://github.com/djunamay/ABCA7lof2), resulting in a total of 150,456 cells.

Sample Swap Analysis

Sample swap analysis was performed using a previously established pipeline MVV (QTLtools_1.1) (*2*), which compares allelic concordance between genomic and transcriptomic sequencing data. As input, we used the BAM files generated in the cellranger counting step and the chromosome 19 (the chromosome harboring ABCA7) variant call files (VCF). When comparing the concordance of BAM and VCF data for homozygous and heterozygous sites, the

expected WGS sample appeared as a clear outlier (more consistent along both dimensions than any of the other 1249 WGS ROSMAP samples) for all single cell samples (**Fig. S2**).

Cell filtering metrics

Prior to cell type annotation, we performed a series of quality control steps on the aggregated counts matrix. First, we removed cells, for which the number of detected genes (N_g) did not fall in the interval [500, 10000], where N_g is defined for each cell as the number of genes, where *counts >0*.

Next, we removed all cells with a high fraction of counts coming from mitochondrial-encoded genes. Mitochondrial fraction (M_f) is a commonly used per-cell metric to measure compromised nuclear integrity, where high fractions indicate low-quality nuclei, where M_f= (total counts $_{\text{mitochondrially-encoded genes}}$)/(total counts $_{\text{all genes}}$). We fit a gaussian mixture model to $\log_2$-transformed per-cell M_f values, using grid search to choose the optimal number of components and covariance type. The model with five components and full covariance had the lowest bayesian information criterion (BIC) score. Cells belonging to the component with the highest average M_f scores were presumed to constitute a population of low-quality cells and removed from further analysis. This initial filtering removed *circa* 20,000 cells.

Considering all remaining cells in marker-gene expression space, where marker genes include only known cell type-specific genes for the major human PFC cell type, including astrocytes (with 159 markers), excitatory neurons (113 markers), inhibitory neurons (83 markers), microglia (97 markers), oligodendrocytes (179 markers), OPCs (143 markers), and vascular cells (124 markers) (**Table S2**) normalized to total library counts, we performed incremental PCA (IncrementalPCA from sklearn.decomposition) on this mean-centered standardized matrix to project cells from the marker gene space onto the top 50 principal components sorted by variance. Visually, the cells formed a number of gaussian-like clusters when the first two principal components were examined. Under the assumption that each gaussian cluster represented a different cell type in the brain, we next fit a gaussian mixture model (GaussianMixture from sklearn.mixture) to the projected data, using grid search (GridSearchCV from sklearn.preprocessing) to choose the optimal number of components and covariance type. The model with ten components and full covariance had the lowest BIC score. Indeed, each resulting cell cluster was robustly enriched for a subset of major cell type markers in the brain, indicating a cluster of astrocytes, microglia, OPCs, oligodendrocytes, excitatory neurons, and inhibitory neurons, and a heterogeneous cluster of vascular cells.

To remove cells that were not well-captured by this model and likely represent low-quality cells, we next computed the per-cell logliklihood (i.e. the liklihood of the observed data, given the model) and removed cells with a liklihood < -100. We also removed two gaussian clusters whose liklihood distributions constituted clear outliers compared to remaining clusters. The excluded cells had significantly lower total counts and higher mitochondrial fractions compared to those that passed the liklihood filter, suggesting that the removed cells indeed were low quality. When examining the data visually projected onto the first two principal components, this filtering removed many of the cells that were not visibly associated with a main gaussian cluster. Together, this filtering removed an additional *circa* 12,000 cells, leaving a total of 118,668 cells.

Gene filtering metrics

For the remaining downstream analysis we only considered genes that were both nuclear-encoded and protein-coding, which constituted a total of 19384 genes, based on annotation of ensembl.GRCh38p12.

Cell type annotations

To avoid biased cell type annotations due to technical artifacts associated with sequencing batch and individual-of origin, we first applied the Python implementation of the Harmony algorithm (*3*) with individual-of-origin as indicator vector to the low-dimensional embedding of cells (first 50 principal components) remaining after the initial rounds of quality control (see above *Cell filtering metrics*). Next, we computed a neighborhood graph on the Harmony-corrected values in the PC embedding space, as implemented in the Scanpy (*4*) Python package, using default parameters. Finally, we applied the Leiden graph-clustering method to cluster this neighborhood graph of cells, using the Scanpy implementation of the Leiden algorithm (*5*).

We used the Scanpy 'rank_genes_groups' function to compute top marker genes per Leiden cluster. Internally, this function uses a T-test to compute the relative enrichments of genes for each Leiden cluster compared to all other Leiden clusters. We assigned a major cell type label ('Ex', 'In', 'Ast', 'Mic', 'Oli', or 'Opc', 'Vascular') by computing per-cluster average $\log_2$-fold-changes (logFC) for respective cell type markers and assigning the cell type with the highest logFC, where large and positive logFCs indicate high relative expression of a gene in a given Leiden clusters compared to all other clusters.

Finally, we sub-clustered cells from each major cell type using the Leiden clustering algorithm and examined distributions of mitochondrial fractions and total counts among subclusters of the same cell type. Clusters whose mean mitochondrial fraction was >2 standard deviations (sd) above the mean or whose mean total counts were < 2 sd below the mean or >2 sd above the mean (when comparing sub-clusters of a single cell type) were removed. Manual inspection of the removed clusters revealed that they tended to have fewer cells and low individual-level representations, and were not well-connected in the graph.

Individual-level filtering

After all rounds of qc as described above, we noted a subset of individuals (N=6) with very few cells (<500) and these subjects were removed from further analysis, resulting in 24 control individuals and 12 ABCA7 LoF individuals. None of these individuals carried ABCA7 LoF variants and removing them did not substantially alter metadata distributions.

Differential gene expression

Per-gene count values were summed for each cell-type-by-individual combination, resulting in 36 pseudobulk gene expression vectors for each of the six major cell types. For each cell type, only genes with a nonzero detection rate >0.10 were considered for differential expression. Pseudobulk counts were normalized using the edgeR (*6*, *7*) TMM method. The residual mean-variance trend not explained by the multivariate linear model (formalized below), was removed using Limma-Voom (*8*). Unknown sources of variance were captured in the model using SVA (*9*). Limma's *lmfit*, *eBayes*, and *toptable* functions (*10*) were then used to estimate differential gene expression statistics, as reported in **Data S3**.

The following model was fit for each cell type:

$G_i = \boldsymbol{\beta}_0$ * ABCA7LoF + $\boldsymbol{\beta}_1$ * msex + $\boldsymbol{\beta}_2$ * nft + $\boldsymbol{\beta}_3$ * amyloid + $\boldsymbol{\beta}_4$ * age_death + $\boldsymbol{\beta}_5$*PMI + $\boldsymbol{\beta}_6$ * batch + $\boldsymbol{\beta}_7$ * APOE4.

G_i refers to a vector of expression profiles of size $1\ x\ 36$ for a gene i in a given cell type. ABCA7LoF is a binary variable, encoding the presence of an ABCA7 variant predicted to cause LoF (see **Data S1**). See **Supplementary Text** for descriptions of the remaining variables included in the model.

Gene-pathway projections

For each cell type, we computed a set of gene-wise scores quantifying the direction and statistical significance of gene expression changes (computed as part of the differential gene expression analysis) associated with ABCA7 LoF: *S = sign(log2FC) * -log10(p-value)*, where *log2FC>0* indicates up-regulation in ABCA7 LoF *vs* control. Top differentially expressed genes per cell type (|S|>1.3) were projected from 6-dimensional score space, where each dimension captures ABCA7 LoF perturbation scores in one of the major cell types (Ex, In, Ast, Mic, Oli, OPC), onto two dimensions, using the UMAP algorithm (*11*, *12*) (umap Python package). Gene scores that were not detected >10% in a given cell type were set to 0. We performed a grid search for gaussian mixture parameters (N components and covariance type) on the embedded cells (using the Python sklearn package) to assign genes to clusters in the 2D space. We proceeded with the model with the lowest BIC score, which had 15 components and a "tied" covariance matrix.

Each cluster was assigned representative pathway names by testing genes in that cluster for enrichment of Gene Ontology Biological Process pathways (**Table S2**) against the background of all genes in the embedding space, by hyper-geometric enrichment (using the Python package gseapy). Pathways with an enrichment p-value < 0.01 were considered for cluster annotation.

Per-cell-type perturbation scores for each cluster were computed as the average gene score *S* (for a given cell type) for all scores in that cluster. The statistical significance of each cell type-specific cluster score was assessed by permuting cluster assignments (100,000 permutations).

Gene-set enrichment analysis

Genes were rank ordered based on their scores *S (*see description in *Gene-pathway projections*). An R implementation of gene set enrichment analysis (*9*, *13*) (fast gene set enrichment analysis, fGSEA (*11*)) was run with 10,000 permutations to estimate the statistical overrepresentation of gene sets in the WikiPathways database (**Table S2**) within high-scoring, differentially expressed genes. Gene sets with a minimum size of 5 and a maximum size of 1000 were considered.

To query a more comprehensive set of specific biological themes related to lipid and NFkB, we performed fGSEA on a larger database of pathways (including HumanCyc, KEGG, Reactome, Biocarta, WikiPathways, and GO BP), after filtering these pathway databases for lipid-related ('sterol', 'lipid', 'glycer', 'fatt', 'ceramide', 'phosphatidyl') and NFkB ('kappa') terms, respectively.

Gene-pathway clustering using Kernighan-Lin heuristic

The Kernighan-Lin heuristic was implemented in python based on the original paper (*14*). The KL algorithm is a heuristic algorithm to divide a graph into N partitions of equal sizes, where N>=2 and N<=(*total # nodes*), while minimizing the sum of all edges that cross partition boundaries (total cut size). Our implementation of the KL algorithm can be found here: https://github.com/djunamay/geneclusters.

To reduce the solution search space and computational complexity, we performed KL clustering on only the leading edge genes (*LE*) from WikiPathways showing perturbation evidence at $p<0.05$ (fGSEA). We subset the bipartite pathway graph *G* to include only genes in the set of *LE* genes and pathways with degree > 4. KL clustering was then run on this smaller bipartite graph with a gene cluster size of 50. Gene-pathway graph layouts were computed using the networkx Python package using the spring layout algorithm, with 10,000 iterations and K=15. Layouts were visualized using the matplotlib pyplot package in Python.

Representative pathways for each cluster were inferred from the graph, by averaging the ABCA7 LoF perturbation scores *S* for all genes in the cluster of interest sharing an edge with the pathway in question. Scores for pathways with intra-cluster degrees>=5 were reported. Genes per cluster were ranked based on $|S|$ and genes with the largest scores ($|S|>1.3$) were reported.

Overlap with CRISPRi perturb-sequencing dataset

Glutamatergic Neuron-RNA-Seq-CRISPRi (2020) data differential gene expression statistics (from CRISPRi perturbed vs non-perturbed cells) were downloaded from the online crisprbrain.org resource (**Table 2**). For each CRISPRi gene target, downstream gene expression changes were summarized as scores (where *Score=sign(log2(FC))*-log10(p-value)*), for all genes, for which average expression *log2CPM > 0*. GSEA was used (parameters: minSize = 5, maxSize = 1000, nPermSimple=10000) to compute enrichment scores for all KL gene clusters (**Data S7**). Only CRISPRi target genes that had a nonzero detection rate >0.25 in *post-mortem* excitatory neurons, as assessed by snRNAseq, and had an ABCA7 LoF perturbation score $|S| > 0.5$ in excitatory neurons, as assessed by snRNAseq in the *post-mortem* human brain, were considered for this analysis.

Lipidomic data analysis

Lipids were identified and their signal integrated using the Lipidsearch © software (version 4.2.27, Mitsui Knowledge Industry, University of Tokyo). Integrations and peak quality were curated manually before exporting. Statistical significance for differences in peak distributions between control and ABCA7 LoF or WT and KO#1 were computed by two-sided unpaired T-test.

Post-mortem **Experimental Methods**

Isolation of nuclei from frozen *post-mortem* brain tissue

The protocol for the isolation of nuclei from frozen *post-mortem* brain tissue was adapted from a previous study (1). All procedures were carried out on ice or at 4°C. In brief, *post-mortem* brain tissue was homogenized in 700 µl Homogenization Buffer (320 mM sucrose, 5 mM CaCl2, 3 mM Mg(CH3COO)2, 10 mM Tris HCl pH 7.8, 0.1 mM EDTA pH 8.0, 0.1% IGEPAL CA-630, 1 mM β-mercaptoethanol, and 0.4 U µl−1 recombinant RNase inhibitor (Clontech)) using a Wheaton Dounce tissue grinder (15 strokes with the loose pestle). Homogenized tissue was filtered through a 40-µm cell strainer, mixed with an equal volume of Working Solution, which is prepared by mixing Diluent (30mM CaCl2, 18mM Mg(CH3COO)2, 60mM Tris pH 7.8, 0.6mM

EDTA, 6mM β-mercaptoethanol) with Optiprep density gradient solution (Sigma-Aldrich D1556-250ML) in a 1:5 ratio. The sample mix was then loaded on top of an Optiprep density gradient consisting of 750 µl 30% OptiPrep solution (1.5:1 ratio of Working Solution:Homogenization Buffer) on top of 300 µl 40% OptiPrep solution (4:1 ratio of Working Solution:Homogenization Buffer). The nuclei were separated by centrifugation (5 min, 10,000 g, 4 °C). Approximately 100µl of nuclei were collected from the 30%/40% interface and washed twice with 1 ml of PBS containing 0.04% BSA, centrifuging 300g for 3 min (4 °C) in between, then resuspended in 100µl PBS containing 0.04% BSA. The nuclei were counted on C-Chip disposable hemocytometer and diluted to 1000 nuclei per µl in PBS containing 0.04% BSA.

Droplet-based snRNA-seq

cDNA libraries were prepared in two batches using the Chromium Single Cell 3′ Reagent Kits v2 or v3 according to the manufacturer's protocol (10x Genomics). The generated scRNA-seq libraries were sequenced using NovaSeq 6000 S2 (28 + 91 bases pair-end run with 8 nucleotide index). Samples were split over two lanes. To increase sequencing depth, samples were sequenced twice, on two flow cells.

Immunohistochemistry in *post-mortem* human brain tissue

Fresh frozen PFC tissue was sectioned on a cryostat microtome (Leica CM3050 S) at 20µm. Slices were fixed on slides in 4% paraformaldehyde at 4°C overnight, washed 2X with PBS, then permeabilized with 0.3% Triton-X for 10-30 min. Permeabilized slices were blocked in PBS with 0.1% Triton X-100 + 10% bovine serum albumin for 2 hours at room temperature, then incubated in primary antibodies diluted in blocking solution (1:500) overnight at 4°C. Slices were washed 3-4X for 10 min with PBS, then incubated in secondary antibodies diluted in blocking solution (1:1000) for 2 hours at room temperature. Autofluorescence was quenched with TrueBlack (Sigma-Aldrich) according to the manufacturer's instructions. Images were acquired using the Zeiss LSM 880 confocal microscope at 20X for quantification. Representative images were acquired at 63X. Images were analyzed using Imaris imaging software. NeuN signal was used to create a mask representing mature neurons, and this algorithm was applied across all images. The sum intensity within the NeuN mask was extracted and normalized to NeuN volume.

Neutral COMET Assay in *post-mortem* human brain tissue

Fresh frozen PFC tissue was homogenized in 500 µL 1X PBS (Sigma Aldrich, P3813) using a Bio-vortexer Homogenizer (Daigger). Homogenized cells were counted and diluted to $1x10^5$ cell/mL. 1% Ultrapure low melting point (LMP) agarose (Invitrogen; Cat#16-520-100) in 1X PBS was warmed to 42°C. Diluted cells (50 uL) were added to 450 uL LMP agarose and gently mixed. Cell/agarose solution (50 uL/sample) was transferred to CometSlide (Trevigen; Cat#4250-200-03), and set at 4°C for 20-30 min, protected from light. Set slides were incubated in cold lysis buffer (40 mL Trevigen CometAssay Lysis Solution (Cat#4250-050-01), 4 mL DMSO) for 14-16 hours at 4°C, protected from light. After lysis, slides were immersed in 1X neutral comet buffer (0.3M sodium acetate, 0.1M Tris, pH 9.0) for 30 min at 4°C, followed by electrophoresis (Trevigen CometAssay Electrophoresis System, Cat#4250-050-ES) in neutral comet buffer at 21V for 45 minutes at 4°C. Slides were incubated in DNA precipitation solution (6.7 mL 7.5M NH4Ac, 43.3 mL 95% ethanol) for 30 min at RT, immersed in 70% ethanol for 30 min at RT, then dried at 37°C for 20-30 min. Cells were stained with 1:10,000 SYBR gold

(Invitrogen, S11494) in TE buffer (10 mM Tris, 1 mM EDTA) for 30 min in the dark, washed briefly in water, dried at 37°C for 15-20 min, and then coverslip mounted with Fluoromount-G Mounting Medium (ThermoFisher, Cat#00-4958-02). Comet tails were imaged on a Zeiss LSM710 at 5x as a 5x5 tile scan for analysis with the OpenComet FIJI plugin using default settings. Representative images were acquired at 20x.

Lipidomics of *post-mortem* human brain tissue

A biphasic extraction protocol was used to isolate a lipid fraction from frozen *post-mortem* prefrontal cortex (~100mg). Briefly, weighed tissue was homogenized using Bio-vortexer Homogenizer (Daigger) in 1 mL cold methanol (Sigma MX0486) and transferred to glass vials (VWR 66011-550) with an additional 1mL of cold methanol. Chloroform (Sigma 1.02444) (4 mL; cold) was added to each vial, and mixed by vortexing for 1 min. Water (Sigma WX0001) (2 mL; cold) was added to each vial, and mixed by vortexing for 1 min. Vials were placed in 50 mL conical tubes and centrifuged for 10 min at 3000 rcf for phase separation. The lower, chloroform phase was collected (3 mL from each sample) and transferred to new vials. A blank treated the same as samples was included throughout the biphasic extraction for lipidomic analysis. Lipidomics and analysis was performed in collaboration with the Harvard Center for Mass Spectrometry (HCMS).

For lipidomics, samples were dried under nitrogen flow and resuspended in 60 µL of chloroform. Each sample was split into two equal aliquots, one for each polarity analysis. LC–MS analyses were modified from (*15*) and were performed on an Orbitrap Exactive plus MS (Thermo Scientific) in line with an Ultimate 3000 LC (Thermo Scientific). Each sample was analyzed in positive and negative modes, in top 5 automatic data-dependent MS/MS mode. Column hardware consisted of a Biobond C4 column (4.6 × 50 mm, 5 µm, Dikma Technologies). Flow rate was set to 100 µL min^{-1} for 5 min with 0% mobile phase B (MB), then switched to 400 µL min^{-1} for 50 min, with a linear gradient of MB from 20% to 100%. The column was then washed at 500 µL min^{-1} for 8 min at 100% MB before being re-equilibrated for 7 min at 0% MB and 500 µL min^{-1}. For positive mode runs, buffers consisted for mobile phase A (MA) of 5mM ammonium formate, 0.1 % formic acid and 5% methanol in water, and for MB of 5 mM ammonium formate, 0.1% formic acid, 5% water, 35% methanol in isopropanol. For negative runs, buffers consisted for MA of 0.03% ammonium hydroxide, 5% methanol in water, and for MB of 0.03% ammonium hydroxide, 5% water, 35% methanol in isopropanol.

NGN2 Experimental Methods

Culture and generation of human isogenic iPSCs

A control parental line was derived from a 75-year-old female (AG09173) with an APOE3/3 genotype by the Picower Institute for Learning and Memory iPSC Facility as first described (*16*). Two ABCA7 LoF isogenic lines were derived from parental AG09173. ABCA7 KO#1, generated by Synthego, contains a premature termination codon in exon 3 (fig. S8A), and to our knowledge, does not directly reflect a patient mutation but is functionally analogous to patient loss-of-function mutations.

ABCA7 KO#2 contains a patient-derived mutation (Y622*) (*17*) and was generated in house by CRISPR-Cas9 genome editing. The CRISPR/Cas9-ABCA7-Y622* sgRNA plasmid was prepared followed by the published protocol (*18*). In brief, a sgRNA sequence within 10 nucleotides from the target site was designed using the CRISPR/Cas9 Design Tool

(http://crispr.mit.edu). The oligomer pairs (forward: 5'-CACCGCCCCTACAGCCACCCGGGCG-3' and reverse: 5'-AAACCGCCCGGGTGGCTGTAGGGGC-3') were annealed and cloned into pSpCas9-2A-GFP (PX458) plasmid (Addgene #48138). Plasmid DNA was submitted for Sanger sequencing to confirm correct ABCA7 sgRNA sequence (fig. S8B).

AG09173 iPSCs were dissociated with Accutase (Thermo Fisher Scientific) supplemented with 10 µM ROCK inhibitor (Tocris) for electroporation using Amaxa and Human Stem Cell Nucleofector Kit I (Lonza). ~$5x10^6$ cells were resuspended in 100 µl of reaction buffer supplemented with 7.5 µg of CRISPR/Cas9-ABCA7 sgRNA plasmid and 15 µg of single-strand oligodeoxynucleotide (ssODN) template (5'-GGTGCGCGCCCCCAGGCCAATCCAGGAGCTGCACCCTAAGCTCCCGTTGCCTCTC ACAGCTGGGAGACATCCTCCCCTAGAGCCACCCGGGCGTCGTCTTCCTGTTCTTGGC AGCCTTCGCGGTGGCCACGGTGACCCAGAGCTTCCTGCTCAGCGCCTTCTTCTCCCG CGCCAACCTGG-3'). This reaction mixture was nucleofected with program A-23, resuspended with media supplemented with 10 µM ROCK inhibitor and seeded on MEF plates. Two days after electroporation, cells were dissociated and filtered through Falcon polystyrene test tubes (Corning #352235), transferred to Falcon polypropylene test tubes (Corning #352063) and sorted by BD FACS Aria IIU in FACS Facility at the Whitehead Institute and seeded as single cells in media supplemented with 1X Penicillin-Streptomycin (P/S, Gemini Bio-products) and 10 µM ROCK inhibitor. After sufficient colony growth, each colony was transferred in part to a 12-well plate while the remainder was collected and used to extract genomic DNA (Qiagen DNeasy Blood & Tissue Kit, Cat. No. 69504) and screen for the Y622* mutation by sanger sequencing.

All lines used were confirmed to have normal karyotypes before use and periodically reviewed (Cell Line Genetics) (**Fig. S8C**). All human iPSCs were maintained at 37°C and 5% CO_2, in feeder-free conditions in mTeSR-1 medium (Cat #85850; STEMCELL Technologies) on Matrigel-coated plates (Cat # 354277; Corning; hESC-Qualified Matrix). iPSCs were passaged at 60–80% confluence using ReLeSR (Cat# 05872; STEMCELL Technologies) and reseeded between 1:6 and 1:24 (depending on desired density) onto Matrigel-coated plates.

<u>rTTA and NGN2 Virus production</u>

HEK293T cells (ATCC, Cat#CRL-3216) were maintained in DMEM/F-12, GlutaMAX (ThermoFisher, Cat#10565018), 10% fetal bovine serum (GeminiBio, SKU#100-106), 1% MEM Non-essential amino acids (Sigma, Cat#M7145), 1% sodium pyruvate (ThermoFisher, Cat#11360070), and 1% Penicillin-Streptomycin (GeminiBio, SKU#400-109). Cells were passaged for maintenance with TrypLE (ThermoFisher, Cat#12605010) at 70-80% confluence and reseeded 1:10 in 10 cm tissue culture plates.

For transfection, HEK293T cells were seeded at $5x10^6$ cells per 10 cm plate. Transfection mixtures containing the components required for 3rd generation lentiviral production (per 10 cm dish: 10 µg EF1a-rtTA-Hygro (Addgene #66810) or pLV-TetO-hNGN2-eGFP-Puro (Addgene #79823), 5 µg pMDL g/pRRE, 2.5 µg pRSV-Rev, 2.5 µg MD2.G, and 48 µL polyethyleneimine (1 mg/mL) in 600 uL OptiMEM (Fisher, Cat#51-985-034)). Mixtures were inverted 10X and incubated at RT for 20 min, then added dropwise to the dish. Transfection media was removed 16h later and replaced with 10 mL fresh media. Three days after transfection, media was collected and centrifuged at 3000 xg for 5 min at 4°C to pellet any contaminating cells. Supernatant was transferred to sterile Millex glass ultracentrifuge tubes and centrifuged at

25,000 rpm for 2 hours using a SW32Ti rotor in a Beckman Optima L-90K Ultracentrifuge. The pellets were resuspended in 1 mL PBS per 10 cm plate, and stored at -80°C until use.

Lentivirus-mediated NGN2 induction in iPSCs

iPSCs were dissociated into single cell suspension with Cell Dissociation Buffer (Life Technologies, Cat#13151-014), centrifuged at 300 xg for 5 min, and resuspended in mTeSR1 media with Rock inhibitor (Rockout; Abcam, ab285418). Single-cell suspension was plated in a 6-well plate coated with Matrigel for an optimized seeding density of 50-60% confluence 24 hours after plating. One day after plating, cells were co-transduced with 80 µL pLV-TetO-hNGN2-eGFP-Puro and 80 µL EF1a-rtTA-Hygro added in 1 mL fresh media per well and incubated overnight at 37°C. NGN2 expression was then induced 24 with addition of 2 mL fresh media supplemented with doxycycline (DOX, 1 µg/mL, final concentration) and Rock inhibitor. Puromycin (1 µg/mL) selection of non-NGN2 expressing cells was performed with media change 24 hours after induction, with continued DOX supplementation. After 24 hours of puromycin selection, immature neurons were re-plated onto PDL/laminin coated plates at $1x10^6$ cells/well on 6-well plates or $5x10^4$ cells/well on 96-well plates. Neurons were maintained in BrainPhys Neuronal Media (STEMCELL Technologies, Cat#05793) with Neurocult SM1 Neuronal Supplement (STEMCELL Technologies, Cat#05711), N2-supplement-A (STEMCELL Technologies, Cat#07152), and DOX (1 µg/mL) with half media changes every 3-4 days. Neuronal cultures were maintained for 28 days before experimentation.

Lipidomics of iPSC-derived neurons

iPSC-derived neurons were washed once with cold PBS (Fisher; Cat#MT21040CM) and lifted off plate with a cell scraper in 1 mL cold PBS . Cells were centrifuged at 2000 xg for 5 min. PBS was removed, and cells were resuspended in 2 mL cold methanol for biphasic extraction as described above for *post-mortem* brain tissue. Lipidomics and analysis was performed in collaboration with the Harvard Center for Mass Spectrometry (HCMS).

For lipidomics, samples were dried under nitrogen flow and resuspended in 60 µL of chloroform. Each sample was split into two equal aliquots, one for each polarity analysis. LC–MS analyses were modified from (*15*) and were performed on an Orbitrap Exactive plus MS (Thermo Scientific) in line with an Ultimate 3000 LC (Thermo Scientific). Each sample was analyzed in positive and negative modes, in top 5 automatic data-dependent MS/MS mode. Column hardware consisted of a Biobond C4 column (4.6 × 50 mm, 5 µm, Dikma Technologies). Flow rate was set to 100 µL min^{-1} for 5 min with 0% mobile phase B (MB), then switched to 400 µL min^{-1} for 50 min, with a linear gradient of MB from 20% to 100%. The column was then washed at 500 µL min^{-1} for 8 min at 100% MB before being re-equilibrated for 7 min at 0% MB and 500 µL min^{-1}. For positive mode runs, buffers consisted for mobile phase A (MA) of 5mM ammonium formate, 0.1 % formic acid and 5% methanol in water, and for MB of 5 mM ammonium formate, 0.1% formic acid, 5% water, 35% methanol in isopropanol. For negative runs, buffers consisted for MA of 0.03% ammonium hydroxide, 5% methanol in water, and for MB of 0.03% ammonium hydroxide, 5% water, 35% methanol in isopropanol.

Immunocytochemistry

Neurons were fixed in 4% paraformaldehyde/4% sucrose in PBS at 4°C for 15 min at room temperature, washed 3X with PBS, then permeabilized with 0.1% Triton-X in PBS for 5 min at

room temperature. Cells were blocked in 2% Bovine Serum Albumin (BSA, Fisher Bioreagents, BP9703) in PBS for 20 min at room temperature, then incubated in primary antibodies diluted in blocking solution (1:500) overnight at 4°C. Cells were washed 3X for 5 min with PBS, then incubated in secondary antibodies diluted in blocking solution (1:1000) for 2 hours at room temperature. Cells were washed 3X for 5 min with PBS, then incubated for 10 min with 1:2000 Hoescht 33342 (Invitrogen, H3570). Cells were washed 1X with PBS, and wells flooded with PBS for imaging. Images were acquired on a Zeiss LSM900 at 20X. Images were analyzed blinded to condition with FIJI/ImageJ, using NeuN or Tuj1 channels to generate neuronal-specific ROIs. Resulting ROIs were filtered by size and Hoescht positivity to ensure accurate ROI selection of neuronal cell bodies.

Neutral COMET assay in iPSC-derived neurons

iPSC-derived neurons were washed once and lifted off plate with cell scraper in 1 mL cold PBS (Fisher; Cat#MT21040CM), and centrifuged at 300 xg for 5 min. PBS was removed, and cells were gently resuspended in 1 mL of cold PBS. Cells were centrifuged at 2000 xg for 5 min. PBS was removed, and cell pellets were flash frozen on dry ice. Cell pellets were dissociated by pipetting up and down with 500 uL cold PBS, and underwent the same procedure described for *post-mortem* brain tissue above.

CellROX and Mitochondrial Health stain

CellROX Green Reagent (ThermoFisher, Cat#C10444) and HCS Mitochondrial Health kit (ThermoFisher, Cat#H10295) were used on live cells according to manufacturer's protocols. In brief, CellROX dye was added directly to cell media for a final concentration of 5µM, while 50 uL of media containing 1.5 µL MitoHealth dye was added to each well. Both stains were incubated on live cells for 30 min at 37°C. Cells were fixed in 4% paraformaldehyde in PBS, then co-stained according to immunocytochemistry procedures described above. Images were acquired on a Zeiss LSM900 at 20X.

Supplementary Text

Description of variables according to the Rush Alzheimer's Disease Center Codebook

1. **age_death.** Age at death
2. **amyloid.** Overall amyloid level - Mean of 8 brain regions. Amyloid beta protein identified by molecularly-specific immunohistochemistry and quantified by image analysis. Value is percent area of cortex occupied by amyloid beta. Mean of amyloid beta score in 8 regions (4 or more regions are needed to calculate). The 8 regions are hippocampus, entorhinal cortex, midfrontal cortex, inferior temporal gyrus, angular gyrus, calcarine cortex, anterior cingulate cortex, superior frontal cortex.
3. **braaksc.** Braak stage. Semi quantitative measure of neurofibrillary tangles. Braak Stage is a semi quantitative measure of severity of neurofibrillary tangle (NFT) pathology. Bielschowsky silver stain was used to visualize NFTs in the frontal, temporal, parietal, entorhinal cortex, and the hippocampus. Braak stages were based upon the distribution and severity of NFT pathology: Braak stages I and II indicate NFTs confined mainly to the entorhinal region of the brain; Braak stages III and IV indicate involvement of limbic regions such as the hippocampus; Braak stages V and VI indicate moderate to severe neocortical involvement.
4. **ceradsc - CERAD score.** Semiquantitative measure of neuritic plaques.CERAD score is a semiquantitative measure of neuritic plaques. A neuropathologic diagnosis was made of no AD (value 4), possible AD (value 3), probable AD (value 2), or definite AD (value 1) based on semiquantitative estimates of neuritic plaque density as recommended by the Consortium to Establish a Registry for Alzheimer's Disease (CERAD), modified to be implemented without adjustment for age and clinical diagnosis. A CERAD neuropathologic diagnosis of AD required moderate (probable AD) or frequent neuritic plaques (definite AD) in one or more neocortical regions. Diagnosis includes algorithm and neuropathologist's opinion, blinded to age and all clinical data. Value 1: definite AD, Value 2: probable AD, Value 3: possible AD, Value 4: no AD.
5. **cogdx - Final consensus cognitive diagnosis.** Clinical consensus diagnosis of cognitive status at time of death. At the time of death, all available clinical data were reviewed by a neurologist with expertise in dementia, and a summary diagnostic opinion was rendered regarding the most likely clinical diagnosis at the time of death. Summary diagnoses were made blinded to all postmortem data. Case conferences including one or more neurologists and a neuropsychologist were used for consensus on selected cases. Value 1: NCI, No cognitive impairment (No impaired domains), Value 2: MCI, Mild cognitive impairment (One impaired domain) and NO other cause of CI, Value 3: MCI, Mild cognitive impairment (One impaired domain) AND another cause of CI, Value 4: AD, Alzheimer's disease and NO other cause of CI (NINCDS PROB AD), Value 5: AD, Alzheimer's disease AND another cause of CI (NINCDS POSS AD), Value 6: Other dementia. Other primary cause of dementia
6. **msex – Sex.** Self-reported sex, with "1" indicating male sex. 1 = Male 0 = Female
7. **nft - Neurofibrillary tangle burden.** Neurofibrillary tangle summary based on 5 regions. Neurofibrillary tangle burden is determined by microscopic examination of silver-stained slides from 5 regions: midfrontal cortex, midtemporal cortex, inferior parietal cortex, entorhinal cortex, and hippocampus. The count of each region is scaled by

dividing by the corresponding standard deviation. The 5 scaled regional measures are then averaged to obtain a summary measure for neurofibrillary tangle burden.

8. **pmi - Post-mortem interval.** Time interval in hours from time of death to autopsy. *Post-mortem* interval (PMI) refers to the interval between death and tissue preservation in hours.

Fig. S1. Overview of human snRNA-sequencing cohort. (A) Sanger sequencing of ABCA7 LoF variants in prefrontal cortex genomic DNA samples from 3 ABCA7 LoF-carriers and 3 controls from the snRNA-seq cohort. Sequencing confirmed heterozygosity of indicated variant in LoF samples, with variant location indicated by black box. (B, C) ABCA7 protein levels (log2(abundance)) (B) and ABCA7 protein levels corrected for NeuN (RBFOX3 levels) (C) from *post-mortem* human prefrontal cortex in all available control vs ABCA7 LoF carriers (see **Table S2** for external dataset used). (D) Permutation for differences in ABCA7 protein between control and ABCA7 LoF-carriers, when repeatedly sampling an equal number of controls to ABCA7 LoF-carriers. (E) NeuN (RBFOX3) protein levels by genotype in the whole cohort. (F) Permutation for differences in NeuN (RBFOX3) protein between control and ABCA7 LoF-carriers as in (D). (G-I) ABCA7 protein levels (G), ABCA7 protein levels corrected for NeuN (RBFOX3) (D), and RBFOX3 levels (I) from *post-mortem* human prefrontal cortex for subset of individuals in the snRNA-seq cohort. (J-M) Distributions of continuous metadata variables (see **Supplementary Text** for descriptions) for control individuals (N=24) vs ABCA7 LoF-carriers (N=12). (N-R) Distributions of discrete metadata variables for control individuals (N=24) vs ABCA7 LoF-carriers (N=12). Con=control, LoF=ABCA7 loss-of-function. P-values in panels B-M were computed by two-sided Wilcoxon rank sum test, except for panels D and F, where p-values were computed empirically by permutation. In panels N-R p-values were computed by two-sided Fisher's exact test.

Fig. S2. Validating matches between whole genome sequencing (WGS) and snRNAseq libraries. Each plot indicates the concordance of homo- and heterozygous SNP calls between WGS and snRNAseq data for a single individual. Matches between WGS SNP calls and snRNAseq BAM inferred SNP calls are indicated by extreme outliers. Expected (i.e. correct) matches are indicated in blue/purple. All 36 sequenced samples included in this study after qc are shown.

Fig. S3. Overview of snRNA-sequencing batch correction and data quality. (A-H) Distributions of continuous (A-D) and discrete (E-I) metadata variables by sequencing batch. (see **Supplementary Text** for descriptions) (J, K) Two-dimensional projection of snRNA-seq single cells from gene expression space, colored by batch 1 (J) or batch 2 (K) after all rounds of quality control. (L) Two-dimensional UMAP projection of snRNA-seq single cells from gene expression space, colored by individual of origin after all rounds of quality control. Each individual is indicated by a different color. (M) Cell type composition by sequencing batch (astrocytes (Ast), red; endothelial cells (Endo), orange; excitatory neurons (Ex), light blue; inhibitory neurons (In), green; microglia (Mic), navy blue; oligodendrocytes (Oli), peach; oligodendrocyte precursor cells (Opc), grey. P-values for all continuous variables were computed by two-sided Wilcoxon rank sum test. P-values for all discrete variables were computed by two-sided Fisher's exact test.

Fig. S4. Overview of snRNAseq cell type annotations. (A) Two-dimensional UMAP projections of individual cells from gene expression space, colored by Leiden clusters (**see Methods**). (B) Average marker gene expression (per-cluster mean log(fold-change) for all marker genes for the cell type indicated along the x-axis). Log(fold-changes) are computed for the cluster of interest vs all remaining clusters. Reference 1 (**Table 2**) marker genes were used. (C) Cladogram visualizing subcluster relationships based on pairwise distances between per-cluster gene expression profiles. (D) Per-individual contributions (fractions) per cell type. (E)

Average marker gene expression profiles (x-axis) per major cell type annotation (y-axis) for two marker gene references (**Table 2**). (F) Distribution of select marker gene expression by cell type. Y-axis indicates logcounts. (G,H) Individual-level gene expression correlations by celltype. (I) Median number of cells per cell type per individual. (J) Cell type fraction by individual.

Fig. S5. Differential gene expression consistency. (A-F) Correlation of differentially expressed genes in indicated cell types as computed on all samples (x-axis) vs excluding batch 2 and APOE4-carriers (y-axis). pcc=Pearson correlation coefficient.

Fig. S6. Cell-type-specific gene UMAPs related to Figure 1. (A) UMAPs showing up-regulated genes per cell type (S>1.3). (B) UMAPs showing down-regulated genes per cell type (S< -1.3). (M) Perturbation patterns of gene clusters shown in Figure 2 in indicated cell type shown as histograms (astrocytes (Ast), red; excitatory neurons (Ex), light blue; inhibitory neurons (In), green; microglia (Mic), navy blue; oligodendrocytes (Oli), peach; oligodendrocyte precursor cells (Opc), grey). Gene scores *S* are plotted on the x-axis and frequency is plotted on the y-axis.

Fig. S7. Neuronal expression of ABCA7 in human brain. (A,C,E,G) Normalized expression of indicated gene in NeuN- *vs* NeuN+ cells (N=6 individuals, from (*6*), see **Table 2**) (B,D,F,H). Normalized expression of indicated gene in glial (per-individual mean expression profiles across Oli, Opc, Ast, Mic) *vs* neuronal cells (per-individual mean expression profiles across Ex and In) from *post-mortem* snRNA-seq data. All p-values are computed by paired-two-sided T-test.

Fig. S8. CRISPR iPSC lines sanger sequencing and karyotype quality control. (A) Sanger sequencing chromatogram confirming single nucleotide insertion in ABCA7 exon 3 to introduce premature termination codon into isogenic iPSC line ABCA7 KO#1 using CRISPR-Cas9 gene editing. (B) Sanger sequencing chromatogram confirming patient single nucleotide polymorphism in ABCA7 exon 15 to introduce premature termination codon into isogenic iPSC line ABCA7 KO#2 using CRISPR-Cas9 gene editing. (C) Normal karyotypes were observed for control, ABCA7 KO# 1 and ABCA7 KO# 2 isogenic iPSC lines.

Fig. S9. Lipidomic analysis in ABCA7 KO vs Control NGN2 neurons. (A) Pairwise Pearson correlation of NGN2 lipidomic profiles. (B) Correlation of lipidomic scores (sign(log(fold-change)*-log10(p-value), T-test) between WT and ABCA7 KO#1 NGN2 neurons by batch. Top consistent lipid changes shown in green. (C) Distribution of |*log(fold-changes)*| per major lipid class in WT vs ABCA7 KO#1 NGN2 neurons.

Fig. S10. ABCA7 LoF in excitatory neurons induces NF-kB activation. (A) NF-kB pathway changes (p<0.025) in ABCA7 LoF excitatory neurons. (B) Left: Representative confocal images of p65 (red) signal in control and ABCA7 LoF prefrontal cortex co-stained for NeuN (white) and DAPI (blue). Right: Quantification of (left) p65 fluorescence intensity normalized to NeuN signal (control: n=3; ABCA7 LoF: n=5; n=number of patient samples) (P<0.0001). 63X images, Scale bars, 50 µm., *P<0.05, ****P<0.0001. (C) Left: Representative confocal images of p65 (greyscale) signal in control, ABCA7 KO#1 and KO#2 iPSC-derived neurons co-stained for Tuj1 (green) and DAPI (blue). 20X images, Scale bars, 50 µm. Right: Quantification of p65 fluorescence intensity shown at left (control: n=144; ABCA7 KO#1: n=195; ABCA7 KO#2: n=179) (KO#1: P<0.0001; KO#2: P<0.0001).

Fig. S11. Qualitative model of ABCA7 pathogenic cascade in excitatory neurons. The data suggests that loss of lipid exporter ABCA7 alters neuronal phospholipid content, leading to an anabolic shift and the observed accumulation in TAGs, which share common precursors with phospholipids. Neurons have a limited capacity to store TAGs as lipid droplets, necessitating the catabolism of these excess TAGs by mitochondria, which we hypothesize results in mitochondrial dysfunction and the production of ROS. This observed mitochondrial dysfunction and elevated ROS can cause DNA damage and inflammatory phenotypes (Created with BioRender.com).

Table S1. Annotation of ABCA7 loss of function variants used in this study

rsID	HGVS.c	HGVS.p	annotation	AD association	N in cohort
rs113809142	c.4416+2T>G	NA	splice donor variant[1]	Steinberg et al (2015), Nature Genetics, Table 1	1
rs200538373	c.5570+5G>C	NA	splice region variant[1,2]	Steinberg et al (2015), Nature Genetics, Table 1	4
rs538591288	c.4208delT	p.Leu1403fs	frameshift variant[1]	Steinberg et al (2015), Nature Genetics, Table 1	1
rs547447016	c.2126_2132delAGCAGGG	p.Glu709fs	frameshift variant[1]	Steinberg et al (2015), Nature Genetics, Table 1	4
rs201060968	c.3641G>A	p.Trp1214*	stop gained	NA	1
19_1053362_G_A	c.3255G>A	p.Trp1085*	stop gained	NA	1

[1]Allen M et al., *Neurol Genet*, 2017. [2]Steinberg et al., *Nat Genet*, 2015.

Table S2. External datasets used

Description	**Access**	**Reference**
NeuN+/- bulk RNA-sequencing from *post-mortem* human brain	https://osf.io/vn7w2/	(*6*)
Cell type specific marker genes for human brain	https://osf.io/vn7w2/	(*19*)
CRISPRi NeuN bulk transcriptomics	https://crisprbrain.org/rna-seq-screen/?screen=Glutamatergic%20Neuron-RNA-Seq-CRISPRi-2020	(*20*)
WikiPathways 2019 Human	https://maayanlab.cloud/Enrichr/#libraries	NA
Gene Ontology Biological Process 2023	https://maayanlab.cloud/Enrichr/#libraries	NA
Post-mortem human PFC proteomic data	https://www.synapse.org/#!Synapse:syn21449368	(*21*)

Table S3. Antibodies used

Antibody name	Company	Catalog No.
p65 (D14E12)	Cell Signaling Technologies	8242
yH2Ax	Millipore	05-636
NeuN	Synaptic Systems	266004
Tuj1	BioLegend	MMS-435P

Table S4. PCR/Sanger sequencing (SS) primers

Primer	Sequence
rs547447016_FOR	5'-ACGCTGGCCTGGATCTACTC-3'
rs547447016_REV	5'-TGCATGCGTGTGCCAAGAAG-3'
chr19.1053362G>A_rs201060968_FOR	5'-CTGAAGCACCCCTTTGTCCAC-3'
chr19.1053362G>A_rs201060968_REV	5'-GAAAGCGCTTGAGAAGCAGGG-3'
chr19.1053362G>A_REV_SS	5'-GCTGCTCATAAACACGCTATTCATCCTTC-3'
rs201060968_FOR_SS	5'-CATTGCTGGCCTAGACGTAA-3'
ABCA7_KO#1_FOR	5'-GTGACGAAAGCGTTAAGCCC-3'
ABCA7_KO#1_REV	5'-GCAGTGGCTTGTTTGGGAAG-3'
ABCA7_KO#2_FOR	5'-CTGGTTCTGGTGCTCAAG-3'
ABCA7_KO#2_REV	5'-CCTACGGCAGACGTCTTCAG-3'

Data S1. Genotypes of interest for all individuals in the selected cohort.

Data S2. ROSMAP cohort metadata for selected individuals in this study.

Data S3. Differential expression statistics for each cell type (related to **Figure 1**).

Data S4. Cluster pathway enrichments (related to **Figure 1**).

Data S5. Cluster cell type enrichments (related to **Figure 1**).

Data S6. All Wikipathway enrichment results (related to **Figure 2**).

Data S7. Kernighan-Lin cluster assignments (related to **Figure 2**). .

Data S8. NGN2 lipidome statistics (related to **Figure 3**).

Data S9. *Post-mortem* PFC lipidome statistics (related to **Figure 3**).

Data S10. Lipid-specific pathway analysis (related to **Figure 3**).

Data S11. Tian-et-al enrichment results (related to **Figure 4**).

Data S12. NFKB-specific analysis (related to **Figure S12**).

1. S. Steinberg, H. Stefansson, T. Jonsson, H. Johannsdottir, A. Ingason, H. Helgason, P. Sulem, O. T. Magnusson, S. A. Gudjonsson, U. Unnsteinsdottir, A. Kong, S. Helisalmi, H. Soininen, J. J. Lah, D. Aarsland, T. Fladby, I. D. Ulstein, S. Djurovic, S. B. Sando, L. R. White, G.-P. Knudsen, L. T. Westlye, G. Selbæk, I. Giegling, H. Hampel, M. Hiltunen, A. I. Levey, O. A. Andreassen, D. Rujescu, P. V. Jonsson, S. Bjornsson, J. Snaedal, K. Stefansson, Loss-of-function variants in ABCA7 confer risk of Alzheimer's disease. *Nat. Genet.* **47**, 445–447 (2015).

2. A. Fort, N. I. Panousis, M. Garieri, S. E. Antonarakis, T. Lappalainen, E. T. Dermitzakis, O. Delaneau, MBV: a method to solve sample mislabeling and detect technical bias in large combined genotype and sequencing assay datasets. *Bioinformatics*. **33** (2017), doi:10.1093/bioinformatics/btx074.

3. I. Korsunsky, N. Millard, J. Fan, K. Slowikowski, F. Zhang, K. Wei, Y. Baglaenko, M. Brenner, P.-R. Loh, S. Raychaudhuri, Fast, sensitive and accurate integration of single-cell data with Harmony. *Nat. Methods*. **16**, 1289–1296 (2019).

4. F. A. Wolf, P. Angerer, F. J. Theis, SCANPY: large-scale single-cell gene expression data analysis. *Genome Biol.* **19**, 1–5 (2018).

5. V. Traag, L. Waltman, N. J. van Eck, From Louvain to Leiden: guaranteeing well-connected communities (2018), doi:10.1038/s41598-019-41695-z.

6. G. M. Welch, C. A. Boix, E. Schmauch, J. Davila-Velderrain, M. B. Victor, V. Dileep, P. L. Bozzelli, Q. Su, J. D. Cheng, A. Lee, N. S. Leary, A. R. Pfenning, M. Kellis, L.-H. Tsai, Neurons burdened by DNA double-strand breaks incite microglia activation through antiviral-like signaling in neurodegeneration. *Sci Adv*. **8**, eabo4662 (2022).

7. M. D. Robinson, D. J. McCarthy, G. K. Smyth, edgeR: a Bioconductor package for differential expression analysis of digital gene expression data. *Bioinformatics*. **26**, 139–140 (2010).

8. C. W. Law, Y. Chen, W. Shi, G. K. Smyth, voom: Precision weights unlock linear model analysis tools for RNA-seq read counts. *Genome Biol.* **15**, R29 (2014).

9. J. T. Leek, J. D. Storey, Capturing heterogeneity in gene expression studies by surrogate variable analysis. *PLoS Genet.* **3**, 1724–1735 (2007).

10. M. E. Ritchie, B. Phipson, D. Wu, Y. Hu, C. W. Law, W. Shi, G. K. Smyth, limma powers differential expression analyses for RNA-sequencing and microarray studies. *Nucleic Acids Res.* **43**, e47 (2015).

11. G. Korotkevich, V. Sukhov, N. Budin, B. Shpak, M. N. Artyomov, A. Sergushichev, Fast gene set enrichment analysis. *bioRxiv* (2021), p. 060012.

12. L. McInnes, J. Healy, J. Melville, UMAP: Uniform Manifold Approximation and Projection for Dimension Reduction (2018), (available at http://arxiv.org/abs/1802.03426).

13. A. Subramanian, P. Tamayo, V. K. Mootha, S. Mukherjee, B. L. Ebert, M. A. Gillette, A. Paulovich, S. L. Pomeroy, T. R. Golub, E. S. Lander, J. P. Mesirov, Gene set enrichment analysis: a knowledge-based approach for interpreting genome-wide expression profiles. *Proc. Natl. Acad. Sci. U. S. A.* **102**, 15545–15550 (2005).

14. *Graph Partitioning: A Heuristic Procedure to Partition Network Graphs*.

15. E. R. Miraldi, H. Sharfi, R. H. Friedline, H. Johnson, T. Zhang, K. S. Lau, H. J. Ko, T. G. Curran, K.

M. Haigis, M. B. Yaffe, R. Bonneau, D. A. Lauffenburger, B. B. Kahn, J. K. Kim, B. G. Neel, A. Saghatelian, F. M. White, Molecular network analysis of phosphotyrosine and lipid metabolism in hepatic PTP1b deletion mice. *Int Bio (Cam)*. **5**, 940–963 (2013).

16. Y.-T. Lin, J. Seo, F. Gao, H. M. Feldman, H.-L. Wen, J. Penney, H. P. Cam, E. Gjoneska, W. K. Raja, J. Cheng, R. Rueda, O. Kritskiy, F. Abdurrob, Z. Peng, B. Milo, C. J. Yu, S. Elmsaouri, D. Dey, T. Ko, B. A. Yankner, L.-H. Tsai, APOE4 Causes Widespread Molecular and Cellular Alterations Associated with Alzheimer's Disease Phenotypes in Human iPSC-Derived Brain Cell Types. *Neuron*. **98**, 1294 (2018).

17. A. De Roeck, C. Van Broeckhoven, K. Sleegers, The role of ABCA7 in Alzheimer's disease: evidence from genomics, transcriptomics and methylomics. *Acta Neuropathol.* **138**, 201–220 (2019).

18. F. A. Ran, P. D. Hsu, J. Wright, V. Agarwala, D. A. Scott, F. Zhang, Genome engineering using the CRISPR-Cas9 system. *Nat. Protoc.* **8**, 2281–2308 (2013).

19. O. Franzén, L.-M. Gan, J. L. M. Björkegren, PanglaoDB: a web server for exploration of mouse and human single-cell RNA sequencing data. *Database* . **2019**, baz046 (2019).

20. CRISPRbrain, (available at https://crisprbrain.org/rna-seq-screen/?screen=Glutamatergic%20Neuron-RNA-Seq-CRISPRi-2020).

21. E. C. B. Johnson, E. B. Dammer, D. M. Duong, L. Ping, M. Zhou, L. Yin, L. A. Higginbotham, A. Guajardo, B. White, J. C. Troncoso, M. Thambisetty, T. J. Montine, E. B. Lee, J. Q. Trojanowski, T. G. Beach, E. M. Reiman, V. Haroutunian, M. Wang, E. Schadt, B. Zhang, D. W. Dickson, N. Ertekin-Taner, T. E. Golde, V. A. Petyuk, P. L. De Jager, D. A. Bennett, T. S. Wingo, S. Rangaraju, I. Hajjar, J. M. Shulman, J. J. Lah, A. I. Levey, N. T. Seyfried, Large-scale proteomic analysis of Alzheimer's disease brain and cerebrospinal fluid reveals early changes in energy metabolism associated with microglia and astrocyte activation. *Nat. Med.* **26**, 769–780 (2020).

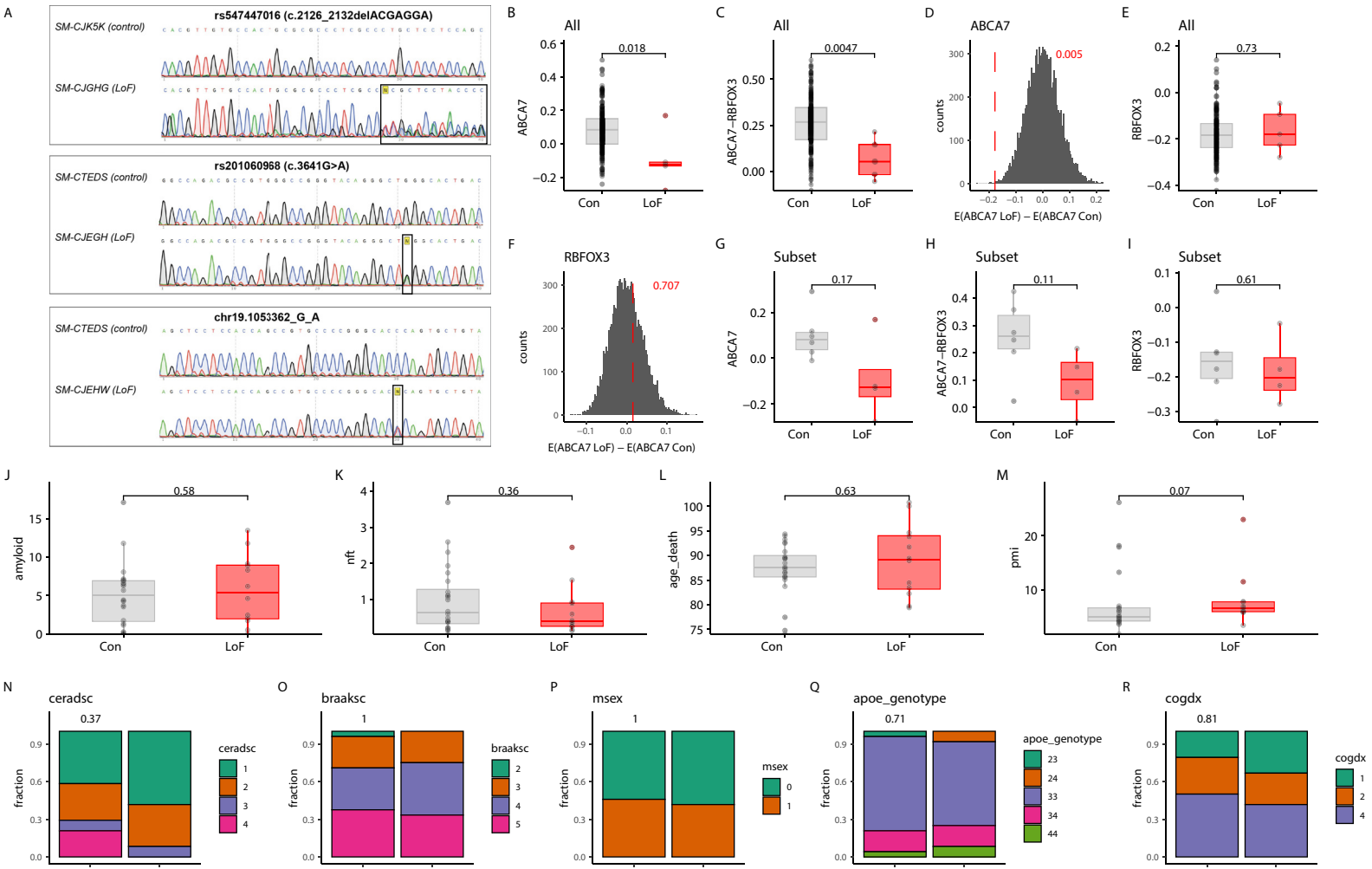
A
rs547447016 (c.2126_2132delACGAGGA)
SM-CJK5K (control)
SM-CJGHG (LoF)
rs201060958 (c.3641G>A)
SM-CTEDS (control)
SM-CJEGH (LoF)
chr19.1053362_G_A
SM-CTEDS (control)
SM-CJEHW (LoF)
B All 0.018 ABCA7 Con LoF
C All 0.0047 ABCA7−RBFOX3 Con LoF
D ABCA7 0.005 counts E(ABCA7 LoF) − E(ABCA7 Con)
E All 0.73 RBFOX3 Con LoF
F RBFOX3 0.707 counts E(ABCA7 LoF) − E(ABCA7 Con)
G Subset 0.17 ABCA7 Con LoF
H Subset 0.11 ABCA7−RBFOX3 Con LoF
I Subset 0.61 RBFOX3 Con LoF
J 0.58 amyloid Con LoF
K 0.36 nft Con LoF
L 0.63 age_death Con LoF
M 0.07 pmi Con LoF
N ceradsc 0.37 fraction ceradsc 1 2 3 4 Con LoF
O braaksc 1 fraction braaksc 2 3 4 5 Con LoF
P msex 1 fraction msex 0 1 Con LoF
Q apoe_genotype 0.71 fraction apoe_genotype 23 24 33 34 44 Con LoF
R cogdx 0.81 fraction cogdx 1 2 4 Con LoF

Figure S1

SM-CJJ35
D17-8756
It's a match
SM-CJIY2
D17-8758
It's a match
SM-CJGO3
D17-8766
It's a match
SM-CJGLE
D17-8768
It's a match
SM-CJGMY
D20-7443
It's a match
SM-CJK5K
D20-7451
It's a match
SM-CJGI5
D17-8772
It's a match
SM-CJIYK
D17-8778
It's a match
SM-CTEM9
D17-8786
It's a match
SM-CTDRT
D17-8790
It's a match
SM-CJEGX
D17-8792
It's a match
SM-CJEKQ
D20-7458
It's a match
SM-CJEJJ
D17-8796
It's a match
SM-CJFOJ
D20-7432
It's a match
SM-CJFND
D20-7433
It's a match
SM-CJFNM
D20-7434
It's a match
SM-CJGGX
D20-7435
It's a match
SM-CJEKK
D20-7436
It's a match
SM-CJFN9
D20-7437
It's a match
SM-CJFOK
D20-7438
It's a match
SM-CJFNB
D20-7439
It's a match
SM-CJEHW
D20-7440
It's a match
SM-CJFKI
D20-7441
It's a match
SM-CJGMM
D20-7442
It's a match
SM-CJGHG
D20-7444
It's a match
SM-CTEDS
D20-7445
It's a match
SM-CTDUM
D20-7446
It's a match
SM-CTED9
D20-7447
It's a match
SM-CTEEP
D20-7448
It's a match
MAP46246604
D20-7450
It's a match
SM-CJIX6
D20-7452
It's a match
SM-CJJ1E
D20-7453
It's a match
SM-CJGIV
D20-7454
It's a match
SM-CTDOJ
D20-7455
It's a match
SM-CJIZR
D20-7456
It's a match
SM-CJEGH
D20-7457
It's a match
fraction consistent homo
fraction consistent hetero

Figure S2

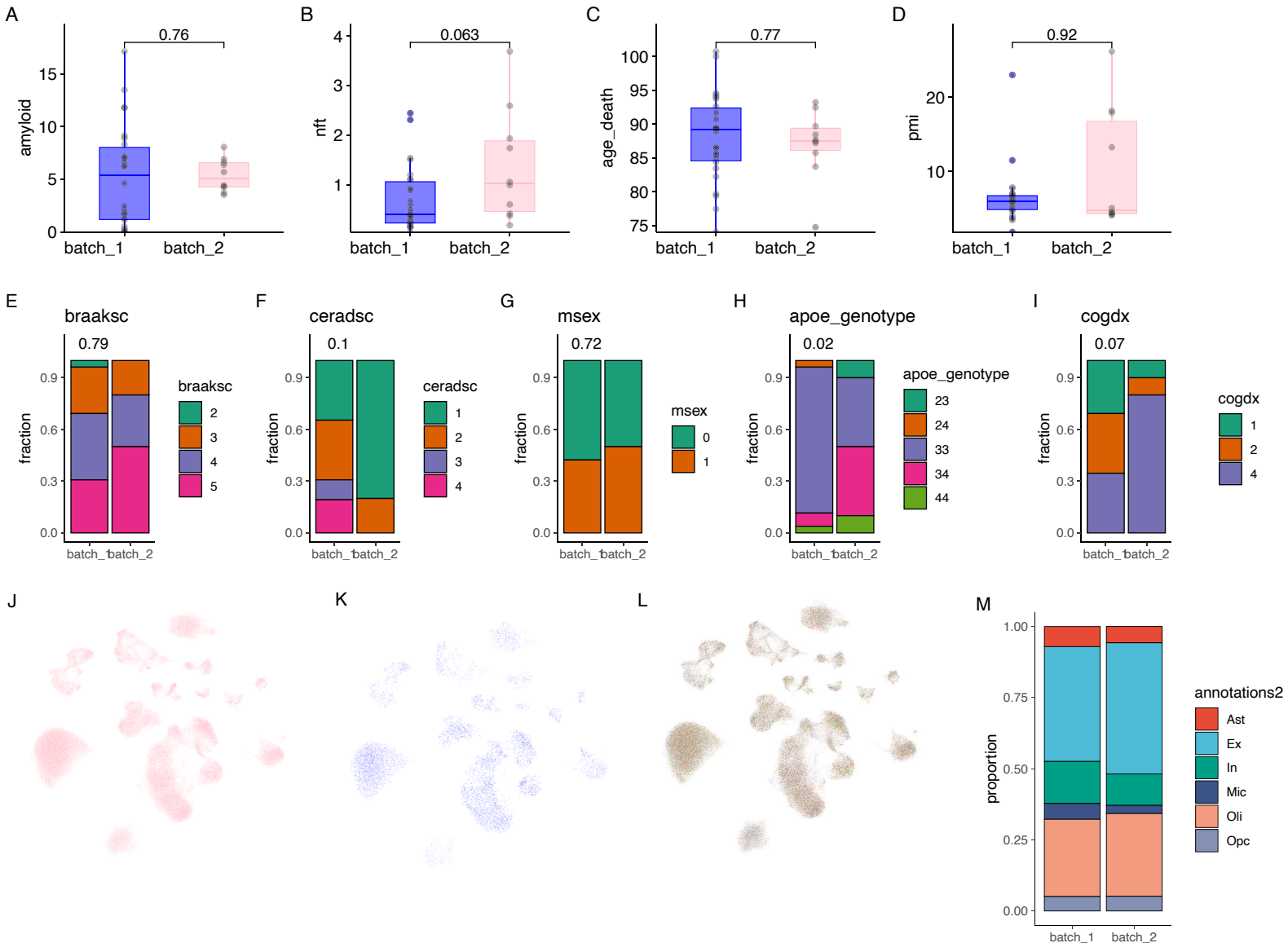
A
0.76
amyloid
batch_1
batch_2
B
0.063
nft
C
0.77
age_death
D
0.92
pmi
E
braaksc
0.79
fraction
F
ceradsc
0.1
G
msex
0.72
H
apoe_genotype
0.02
I
cogdx
0.07
J
K
L
M
proportion
annotations2
Ast
Ex
In
Mic
Oli
Opc

Figure S3

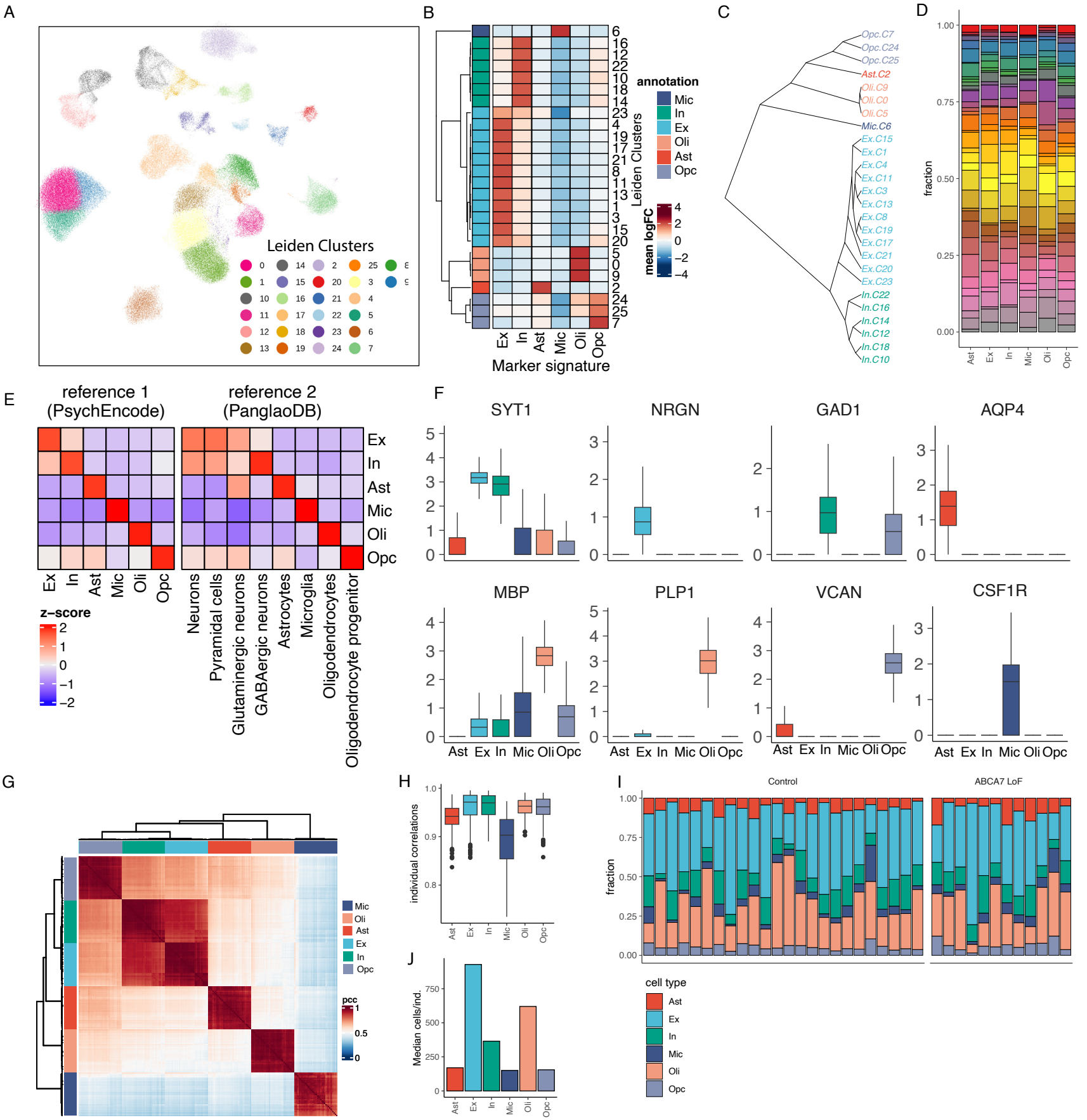
A
Leiden Clusters
B
annotation
Mic
In
Ex
Oli
Ast
Opc
Leiden Clusters
mean logFC
Marker signature
C
D
fraction
E
reference 1
(PsychEncode)
reference 2
(PanglaoDB)
z-score
Neurons
Pyramidal cells
Glutaminergic neurons
GABAergic neurons
Astrocytes
Microglia
Oligodendrocytes
Oligodendrocyte progenitor
F
SYT1
NRGN
GAD1
AQP4
MBP
PLP1
VCAN
CSF1R
G
pcc
H
individual correlations
I
Control
ABCA7 LoF
fraction
cell type
J
Median cells/ind.

Figure S4

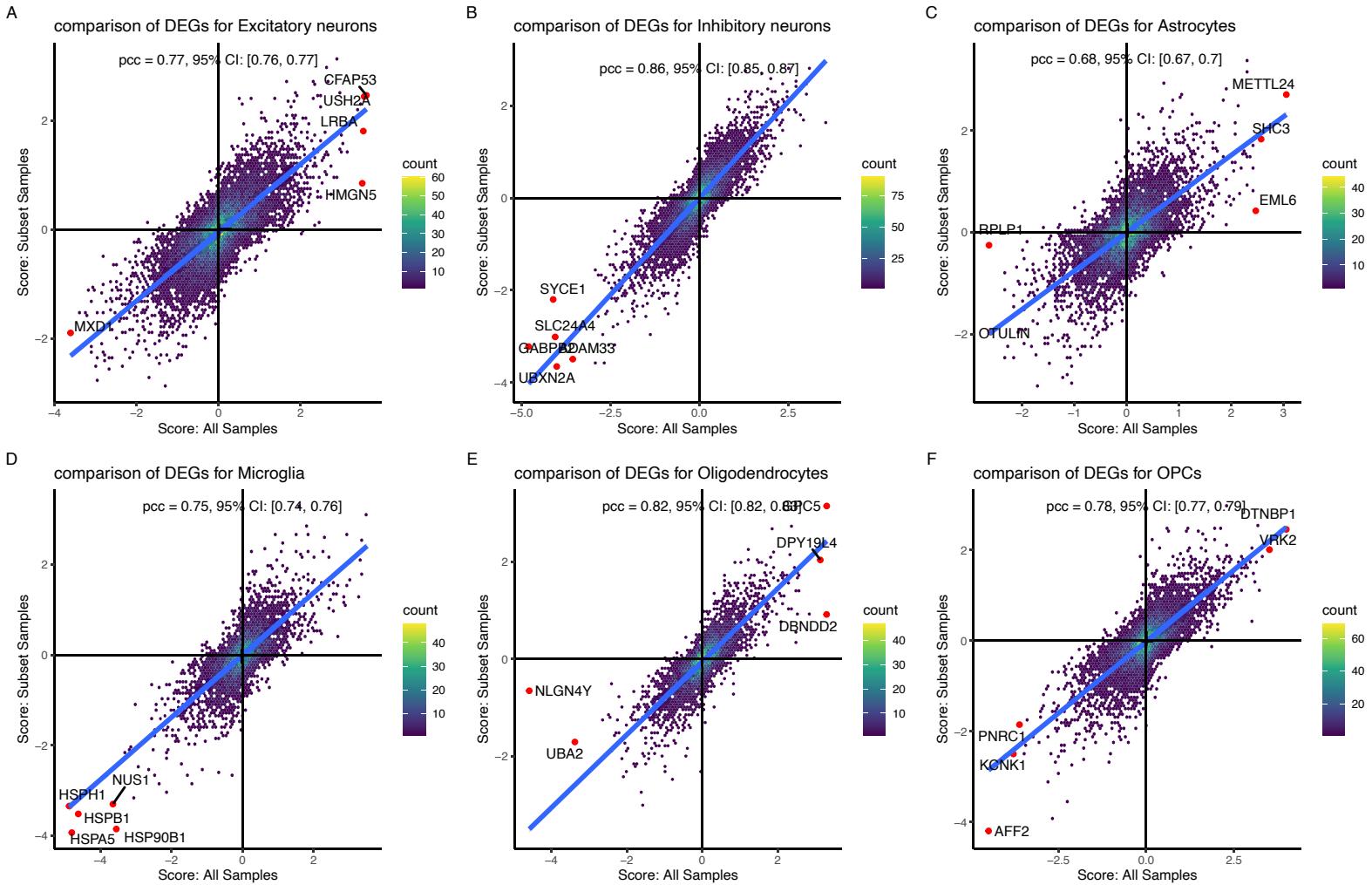
A
comparison of DEGs for Excitatory neurons
pcc = 0.77, 95% CI: [0.76, 0.77]
CFAP53
USH2A
LRBA
HMGN5
MXD1
Score: Subset Samples
Score: All Samples
count
B
comparison of DEGs for Inhibitory neurons
pcc = 0.86, 95% CI: [0.85, 0.87]
SYCE1
SLC24A4
GABPB2
ADAM33
UBXN2A
C
comparison of DEGs for Astrocytes
pcc = 0.68, 95% CI: [0.67, 0.7]
METTL24
SHC3
EML6
RPLP1
OTULIN
D
comparison of DEGs for Microglia
pcc = 0.75, 95% CI: [0.74, 0.76]
NUS1
HSPH1
HSPB1
HSPA5
HSP90B1
E
comparison of DEGs for Oligodendrocytes
pcc = 0.82, 95% CI: [0.82, 0.83]
GPC5
DPY19L4
DBNDD2
NLGN4Y
UBA2
F
comparison of DEGs for OPCs
pcc = 0.78, 95% CI: [0.77, 0.79]
DTNBP1
VRK2
PNRC1
KCNK1
AFF2

Figure S5

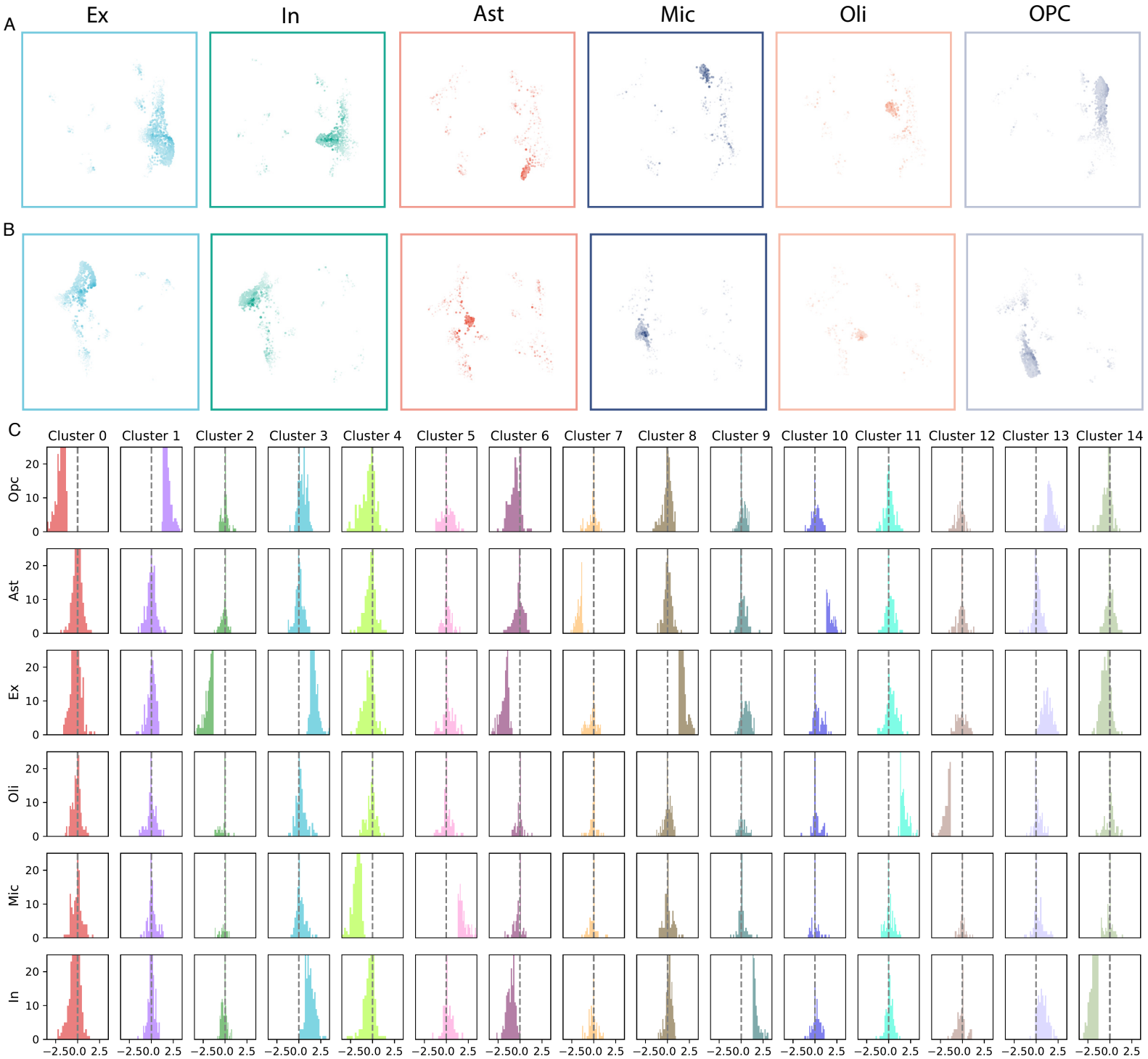
A
Ex
In
Ast
Mic
Oli
OPC
B
C
Cluster 0
Cluster 1
Cluster 2
Cluster 3
Cluster 4
Cluster 5
Cluster 6
Cluster 7
Cluster 8
Cluster 9
Cluster 10
Cluster 11
Cluster 12
Cluster 13
Cluster 14
Opc
Ast
Ex
Oli
Mic
In
0
10
20
−2.5
0.0
2.5

Figure S6

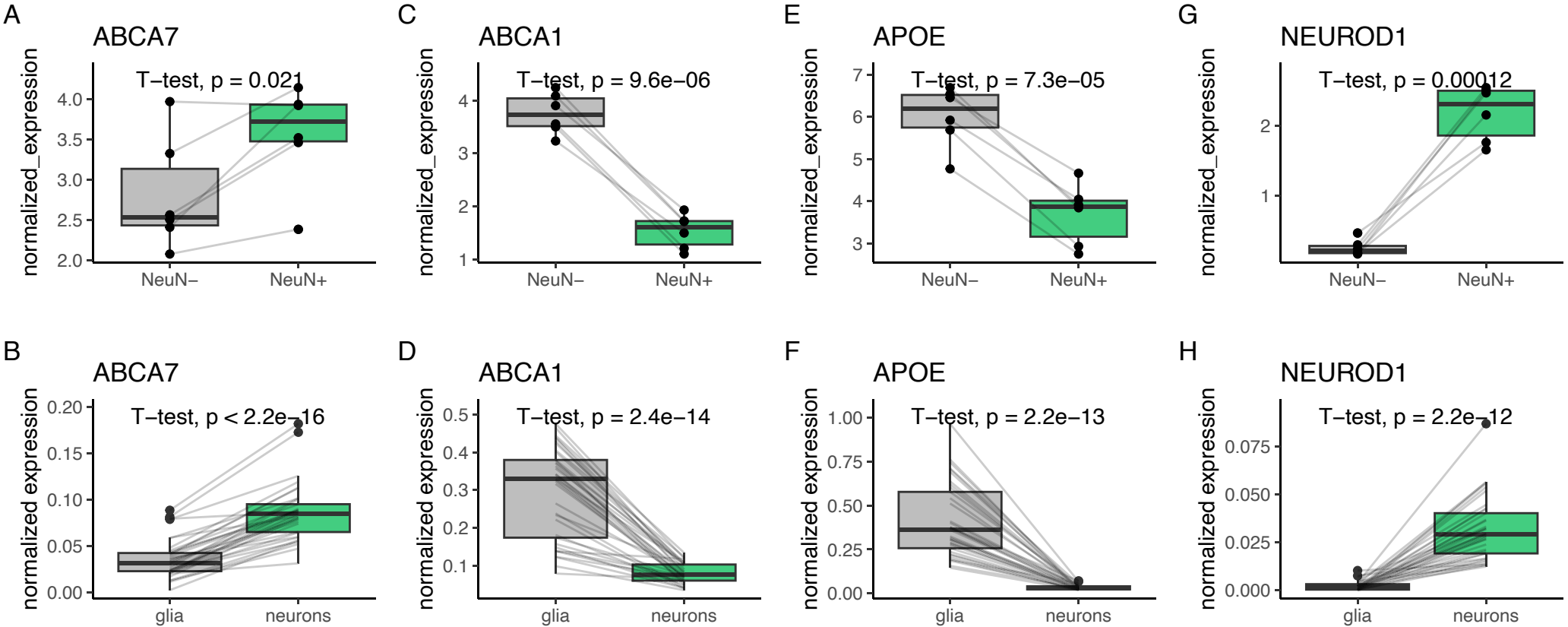
A
ABCA7
T−test, p = 0.021
normalized_expression
4.0
3.5
3.0
2.5
2.0
NeuN−
NeuN+
C
ABCA1
T−test, p = 9.6e−06
normalized_expression
4
3
2
1
NeuN−
NeuN+
E
APOE
T−test, p = 7.3e−05
normalized_expression
7
6
5
4
3
NeuN−
NeuN+
G
NEUROD1
T−test, p = 0.00012
normalized_expression
2
1
NeuN−
NeuN+
B
ABCA7
T−test, p < 2.2e−16
normalized expression
0.20
0.15
0.10
0.05
0.00
glia
neurons
D
ABCA1
T−test, p = 2.4e−14
normalized expression
0.5
0.4
0.3
0.2
0.1
glia
neurons
F
APOE
T−test, p = 2.2e−13
normalized expression
1.00
0.75
0.50
0.25
0.00
glia
neurons
H
NEUROD1
T−test, p = 2.2e−12
normalized expression
0.075
0.050
0.025
0.000
glia
neurons

Figure S7

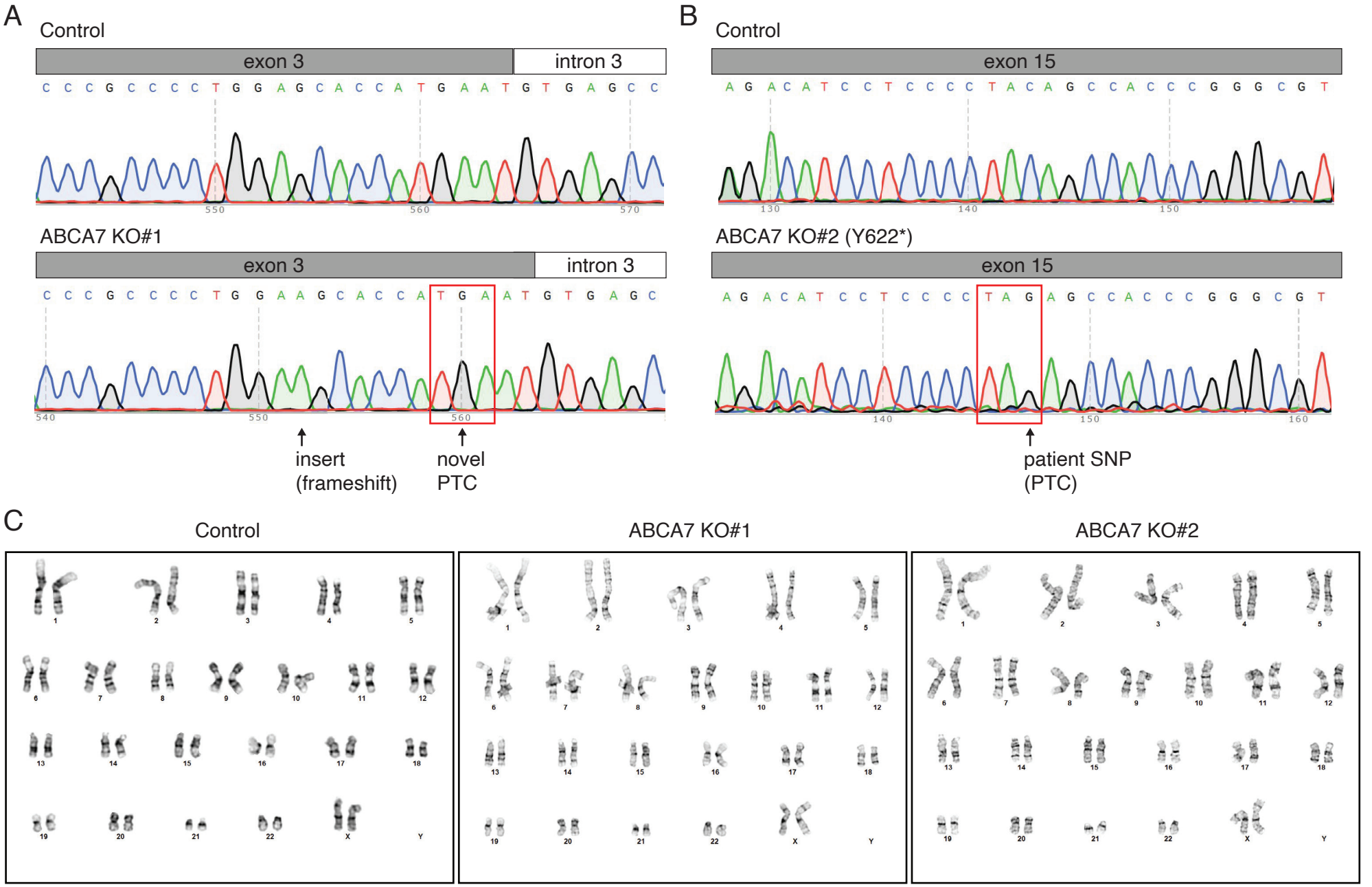
A
Control
exon 3
intron 3
ABCA7 KO#1
exon 3
intron 3
insert
(frameshift)
novel
PTC
B
Control
exon 15
ABCA7 KO#2 (Y622*)
exon 15
patient SNP
(PTC)
C
Control
ABCA7 KO#1
ABCA7 KO#2

Figure S8

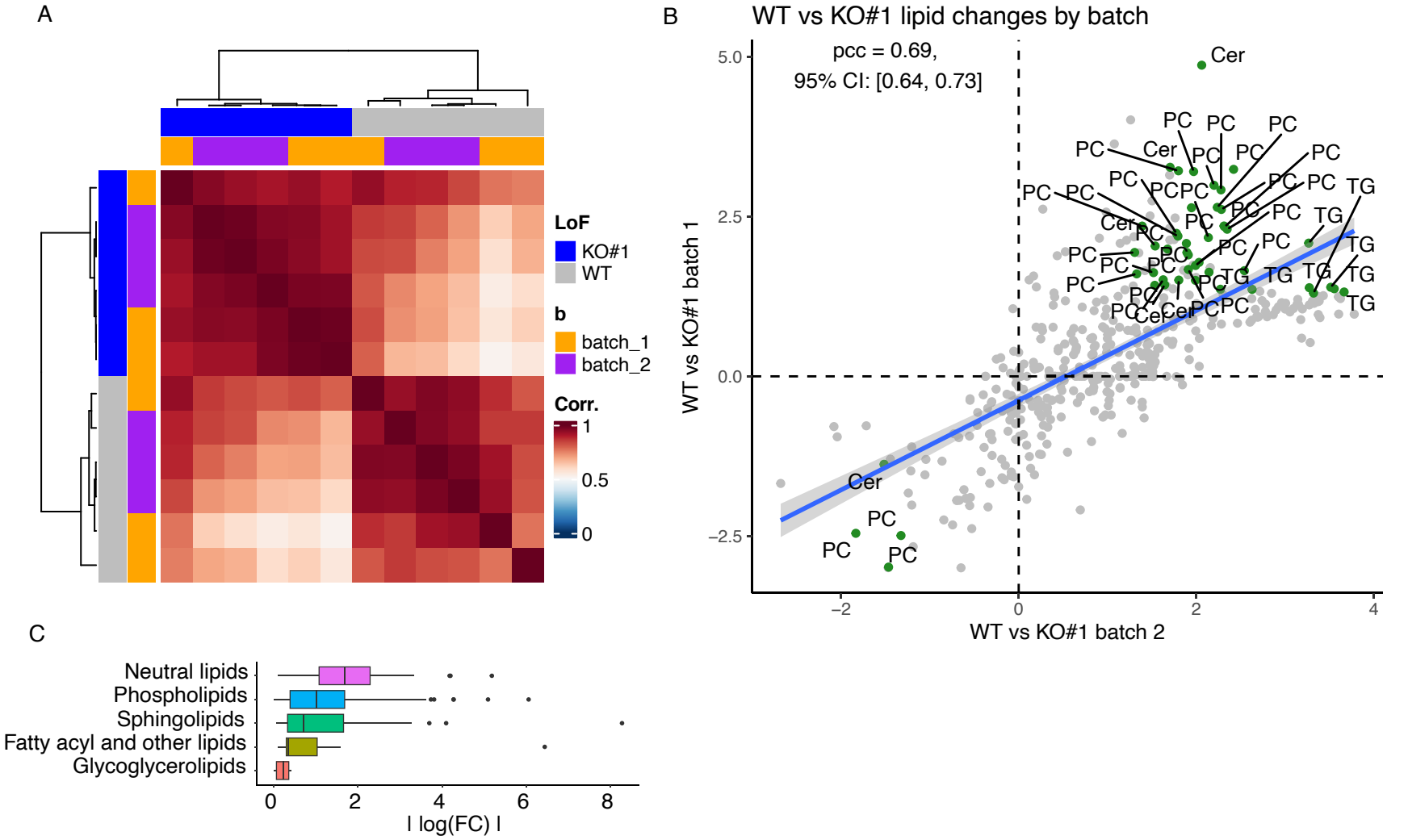
A
LoF
KO#1
WT
b
batch_1
batch_2
Corr.
1
0.5
0
B
WT vs KO#1 lipid changes by batch
pcc = 0.69,
95% CI: [0.64, 0.73]
WT vs KO#1 batch 1
WT vs KO#1 batch 2
5.0
2.5
0.0
−2.5
−2
0
2
4
Cer
PC
TG
C
Neutral lipids
Phospholipids
Sphingolipids
Fatty acyl and other lipids
Glycoglycerolipids
0
2
4
6
8
| log(FC) |

Figure S9

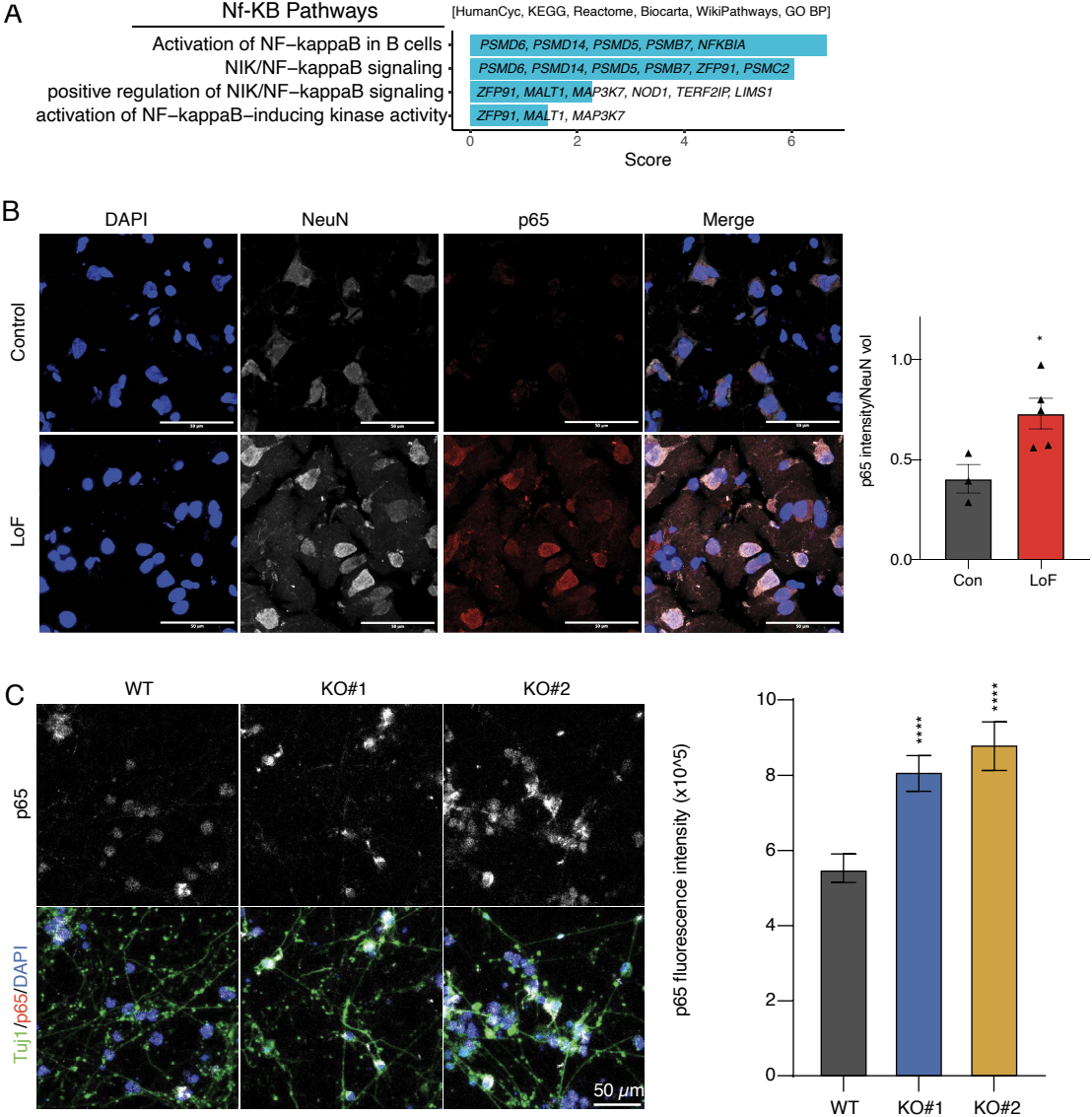
A
Nf-KB Pathways
[HumanCyc, KEGG, Reactome, Biocarta, WikiPathways, GO BP]
Activation of NF−kappaB in B cells
NIK/NF−kappaB signaling
positive regulation of NIK/NF−kappaB signaling
activation of NF−kappaB−inducing kinase activity
PSMD6, PSMD14, PSMD5, PSMB7, NFKBIA
PSMD6, PSMD14, PSMD5, PSMB7, ZFP91, PSMC2
ZFP91, MALT1, MAP3K7, NOD1, TERF2IP, LIMS1
ZFP91, MALT1, MAP3K7
0
2
4
6
Score
B
DAPI
NeuN
p65
Merge
Control
LoF
p65 intensity/NeuN vol
1.0
0.5
0.0
Con
LoF
C
WT
KO#1
KO#2
p65
Tuj1/p65/DAPI
50 μm
p65 fluorescence intensity (x10^5)
10
8
6
4
2
0
****
****
WT
KO#1
KO#2

Figure S10

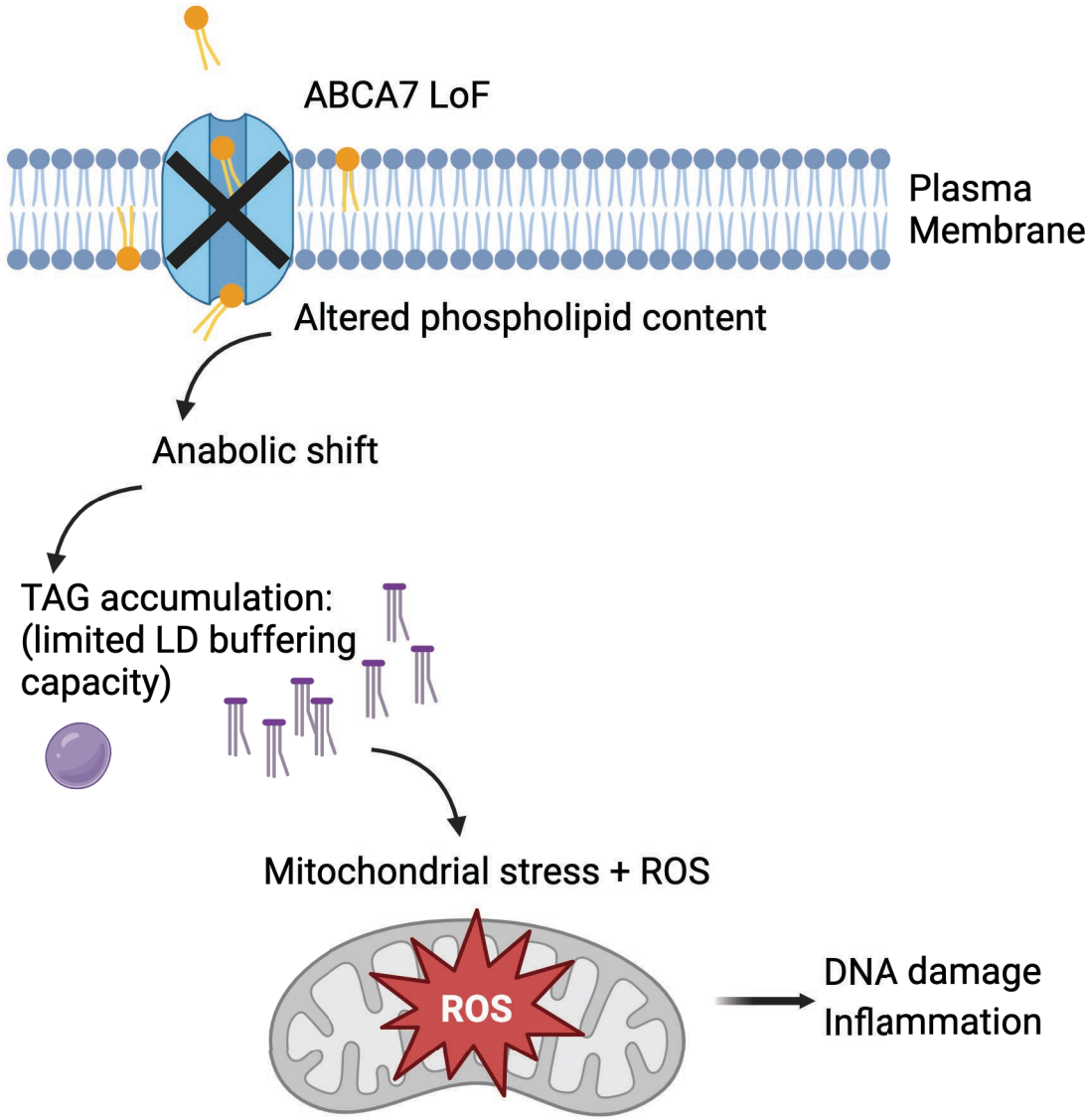
ABCA7 LoF
Plasma
Membrane
Altered phospholipid content
Anabolic shift
TAG accumulation:
(limited LD buffering
capacity)
Mitochondrial stress + ROS
ROS
DNA damage
Inflammation

Figure S11